High Precision Dynamical Masses of Very Low Mass Binaries

Q.M. Konopacky[1], A.M. Ghez[1,2], T.S. Barman[3], E.L. Rice[1], J.I. Bailey, III[4], R.J. White[5], I.S. McLean[1], G. Duchêne[6,7]

ABSTRACT

We present the results of a 3 year monitoring program of a sample of 26 very low mass (VLM) field binaries using both astrometric and spectroscopic data obtained in conjunction with the laser guide star adaptive optics system on the W.M. Keck II 10 m telescope. By combining astrometry and spectroscopy, degeneracies in orbital parameters can be resolved and individual component masses can be obtained. We present relative orbits for 15 of these systems, which allow us to derive the total system mass. There measurements triple the number of mass measurements for VLM objects. In addition, we find the absolute orbits for 6 systems in our sample, giving the mass ratio of the of the binary components, which in turn allows us to derive individual masses. We determine the eccentricity distribution for our 15 sources with relative orbital solutions, and find an excess of systems with low eccentricites compared to what is seen for higher mass stars. We then compare our dynamical mass measurements to the predictions of theoretical evolutionary models and find that there are systematic discrepancies. Specifically, we find that for systems with the most precisely deteremined masses, both models considered either underpredict or overpredict the correct mass. The discrepancies are a function of spectral type, with late M through mid L systems tending to have their masses underpredicted, while one T type system has its mass overpredicted. These discrepancies imply that either the temperatures predicted by evolutionary and atmosphere models are inconsistent for an object of a given mass, or the mass-radius relationship or cooling timescales predicted by the evolutionary models are incorrect. If the trends we see with spectral type hold into the planetary mass regime, the implication is that the amsses of directly imaged extrasolar planets will be overpredicted by the evolutionary models. Future direct measurements of the radii of

---

[1] UCLA Division of Astronomy and Astrophysics, Los Angeles, CA 90095-1562 ; quinn, ghez@astro.ucla.edu

[2] Institute of Geophysics and Planetary Physics, University of California, Los Angeles, CA 90095-1565

[3] Lowell Observatory, 1400 W. Mars Hill Rd., Flagstaff, AZ 86001; barman@lowell.edu

[4] Department of Astronomy, University of Michigan, 500 Church Street, Ann Arbor, MI 48105, baileyji@umich.edu

[5] Department of Physics and Astronomy, Georgia State University, Atlanta, GA 30303, white@chara.gsu.edu

[6] Laboratoire d'Astrophysique, Observatoire de Grenoble, Universite Joseph Fourier - BP 53, F-38041, Grenoble Cedex 9, France; Gaspard.Duchene@obs.ujf-grenoble.fr

[7] Astronomy Department, UC Berkeley, 601 Campbell Hall, Berkeley, CA 94720-3411, USA

these objects, in addition to improved precision in dynamical mass estimates and further individual mass determinations, will distinguish the cause of these discrepancies.

Subject headings: stars: binaries, visual; stars: low-mass, brown dwarfs; stars: individual (2MASSW J0746425+200032, **others**), stars: fundamental parameters

1. Introduction

Characterizing the fundamental properties of brown dwarfs is an important step in unlocking the physics of substellar objects, including gas giant planets. These very cool objects have internal and atmospheric properties unique from those of stars, including partially degenerate interiors, dominant molecular opacities, and atmospheric dust formation (Chabrier & Baraffe 2000). Brown dwarfs also represent a substantial fraction of the galactic stellar content, and are bright and numerous enough to be studied in great detail with current technology (Kirkpatrick 2005). Thus, these substellar objects present an ideal laboratory in which to study the physical processes at work in very low mass objects that both approach and overlap the planetary mass regime.

Mass is the most fundamental parameter in determining the properties and evolution of a brown dwarf; unfortunately it is also one of the most difficult to measure. Masses of brown dwarfs are typically inferred from the comparison of measured luminosities and temperatures with predictions from theoretical models. However, masses obtained in this way from different models can be discrepant, especially amongst the lowest mass objects (Hillenbrand & White 2004; Tamazian et al. 2002; Liu et al. 2008). These discrepancies stem from physical assumptions about the interior and atmospheric properties of these highly complex objects (Burrows et al. 1997; Chabrier et al. 2000). An essential step toward properly calibrating these models and constraining their physics is to obtain dynamical mass measurements of brown dwarfs.

By determining the orbital solutions of brown dwarfs that are part of binary systems, masses can be measured. Orbital measurements are normally made by monitoring either spectroscopic binaries using high resolution spectroscopy or visual binaries using high resolution imaging. Amongst very low mass (VLM) objects, two spectroscopic binaries have had their orbital solutions calculated (Basri & Martin 1999, Stassun et al. 2006). Spectroscopic orbital solutions provide the mass ratio of the components of the binary (unless the system is eclipsing, in which case component masses can be derived, Stassun et al. 2006). Five VLM visual binaries have also had their orbital solutions derived via astrometric monitoring (Lane et al. 2001, Bouy et al. 2004, Liu et al. 2008, Dupuy et al. 2009a, Dupuy et al. 2009b). Of these five systems, four have been monitored using adaptive optics (AO) on the W.M. Keck II telescope. In particular, the advent of laser guide star adaptive optics (LGS AO) at Keck has drastically increased the number of VLM objects that can be observed at high spatial resolution (Wizinowich et al. 2006). In a survey done in parallel to the work presented here, both the orbit of 2MASS 1534-29 AB (Liu et al. 2008) and LHS 2397a AB (Dupuy et al. 2009b) were derived using data obtained in conjunction with LGS AO system. Total system masses are derived when only astrometric measurements are obtained for visual binaries, as is the case for four out of five of these measurements.

The most powerful tests of theoretical evolutionary models can be performed if the individual component masses of a binary are known (as was demonstrated by Stassun et al. 2006). Individual component masses allow for the comparison of objects to the predictions of models free of assumptions about their relationship to their companion, and also provide definitive determination of whether an object is substellar if it is near the stellar/substellar boundary. Other than eclipsing binaries, one of the best ways to derive component masses is to monitor a visual binary using high resolution spectroscopy in combination with astrometry. Derivations of both the total system mass with astrometry and the mass ratio with spectroscopy can be combined to give individual masses for the components.

The relative radial velocity expected between the components of visual binaries is typically less than 10 km/s. Thus, in most cases, visual binaries monitored with unresolved high resolution spectroscopy will not have a measurable velocity shift much beyond the systemic velocity of the system - more likely, the absorption lines of the combined system will appear broadened. In order to measure the radial velocities of each component, it is desirable to have spatially resolved, high resolution spectroscopic observations. The high spectral resolution (R$\sim$25000), near-infrared spectrograph NIRSPEC, offered on Keck II in conjunction with the LGS AO system, enables these necessary observations. By yielding high resolution spectra of each component, NIRSPEC provides the ability to determine individual component radial velocities and to derive the mass ratio of a visual binary. This method has been shown to be possible in the case of GJ 569Bab, where a combination of astrometric and spatially-resolved spectroscopic monitoring provided component masses (Zapatero Osorio et al. 2004, Simon et al. 2006). Measurements such as these are currently not possible from space, as there is no instrument that achieves the necessary spectral resolution. We now seek a larger sample of mass measurements across a range of spectral types in order to systematically test evolutionary models.

We present the first results from our ongoing monitoring campaign of VLM visual binaries using the LGS AO system on the Keck II telescope. Over the course of three years, we have monitored a total of 26 VLM binaries. We present the relative orbital solutions for 15 systems, tripling the current number of mass measurements for VLM objects, and the absolute orbits for 6 systems. In section 2, we describe our sample selection and in section 3 we discuss our astrometric and spectroscopic observations. In section 4, we outline our data analysis procedures and in section 5, we describe our derivation of orbital solutions. In section 6, we derive bolometric luminosities and effective temperatures for the components of the binaries, and in section 7, we discuss the distribution of eccentricities as determined by our sample. In section 8 we present the comparison of our findings to evolutionary models. We then discuss the implications of our model comparison in section 9. We summarizes our findings in section 10.

2. Sample Selection

2.1. Initial Sample

The initial sample for this project was culled from Burgasser et al. (2007), which listed the 68 visual, VLM binaries known as of 2006. Three cuts were applied to this initial list. First, the binaries had to be observable with the Keck telescope LGS AO system, so we imposed a declination > -35 degrees requirement, which reduced the possible number of targets to 61. Second, the operation of the LGS AO system requires a tip-tilt reference source of apparent R magnitude < 18 within an arcminute of the source, and therefore VLM binaries without a suitable tip-tilt reference were also cut. This lowered the total number of observable targets to 49, 80% of the northern hemisphere sample.

Third, we required that useful dynamical mass estimates would likely be obtained by 2009. To assess the required precision for our dynamical mass estimates, we calculated the predicted masses for the two most commonly used sets of evolutionary models, those of Burrows et al. (1997) and Chabrier et al. (2000), across the entire range of temperatures and luminosities spanned by both models. We calculated the percent difference between the predictions of each model with respect to the prediction of Burrows et al. (1997). The results of this assessment are shown in Figure 10, which displays in color the offset between the models across the H-R diagram (with the discrepancies averaged in 50 K temperature increments and 0.1 $\log(L/L_\odot$ increments). As the figure demonstrates, we found that the difference in the mass predictions of the two models varied from anywhere from a few percent to greater than 100%. We therefore chose a precision goal of 10% because at this level the majority of the models predictions could be distinguished and because this level of precision was reasonable to expect given our observing strategy.

To implement our third cut, a series of Monte Carlo simulations were performed. In these simulations, the total system mass for each target was assumed based on the estimated spectral types of the binary components and held constant for all runs. Additionally, the semi-major axis of the orbit was chosen by sampling from the range of possible values between 1/2 and two times the original separation measurement. From these assumptions, a period was calculated, and T_o (time of periapse passage) was randomly selected from the range allowed by this period. All other orbital parameters for an astrometric orbit, which include e (eccentricity), i (inclination), Ω (longitude of the ascending node), and ω (argument of pericenter), where randomly selected from among the complete range of possible values of each parameter. Although it has been shown amongst higher mass field stars that the eccentricity distribution is not flat ($f(e) \sim 2e$, Duquennoy & Mayor 1991), it is unclear whether this distribution holds for VLM binaries, so we opted to sample from a flat eccentricity distribution.

Using these simulated orbits, it was possible to generate simulated sets of "astrometric datapoints" corresponding to the likely times of measurement. We planned on two observing campaigns per year, one in June and one in December. These dates were chosen to coincide with the two times per year that NIRSPEC is offered behind the LGS AO system at Keck (see section 3). The sky coordinates of each binary then determined whether we simulated one or two astrometric data points per year. We also generated simulated sets of relative radial velocity measurements, which could be predicted from orbital parameters chosen for each run. These simulated measurements were chosen to correspond to appropriate observing dates. All synthetic data points were combined with already existing measurements, the number of which varied from source to source. While the majority of sources initially had only one previous astrometric measurement, others had up to six. Synthetic astrometric datapoints were also assigned uncertainties based on the average uncertainty normally obtained for measurements of binary stars using the Keck AO system with NIRC2 ($\sigma \sim$ 1 mas). Although the average uncertainty in relative radial velocity measurements with NIRSPAO was not known at the time, other observations with NIRSPEC suggested using a conservative uncertainty of about 1 km/s. All datapoints where then used to run the orbital solution fitter, which uses the Thiele-Innes method (e.g., Hilditch 2001), minimizing the χ^2 between the model and the measurements (see Ghez et al. 2008). A chi-squared cut of 10 was imposed to account for the fact that in some simulated orbital solutions could not generate astrometric measurements corresponding to real data points in those systems with multiple measurements. In this way, we were able to utilize more information than simply separation and estimated mass to calculate likelihood of accurate mass measurement in a system. A total of 1000 simulated orbital solutions were created for each system.

From each of these simulations, the predicted uncertainty in dynamical mass could be determined. All those systems for which 66% of the simulations yielded precisions of 10% or better in mass were put in the final sample. This generated a sample of 21 targets that we began monitoring in the spring of 2006. These sources are listed in Table 1. Figure 10 shows the results of our simulations, plotting the percent of solutions with precise mass estimates versus the initial binary separation. The spectral type of the primary component is denoted by symbol, and sources included in our initial sample are colored red. The variation in percent of solutions with separation stems from the variation in the estimated masses of the components and the number of previous measurements at the start of our monitoring program.

2.2. Sample Refinement

Upon commencement of the monitoring campaign, it became clear that sample refinement and adjustment of observing priorities was required. Three sources had tip/tilt stars that did not allow for successful observati on (2MASS 0423-04, GJ 417B, and 2MASS 1217-03). It is possible that some of these tip/tilt stars were actually resolved galaxies. In addition, 2MASS 1217-03 was later reobserved with HST and determined to not be resolved, making it unlikely to be a binary (Burgasser et al. 2006). Three sources were successfully observed, but were unresolved in all NIRC2 observations (2MASS 0518-28, 2MASS 0652+47, and 2MASS 1600+17). It is possible that these sources have orbits that take them below the Keck diffraction limit. The source 2MASS 1047+40 was possibly marginally resolved in our first epoch of data in 2006 June, but all other measurements were unresolved. We report all unresolved measurements as upper limits. Finally, one source, 2MASS1017+13 was observed and resolved in 2006 November, but subsequent iterations of our Monte Carlo techniques showed that with this new epoch of data, the source was no longer "likely" to yield a mass with the necessary precision. We therefore also ceased additional observations of this target.

Additionally, a few targets were added to the monitoring program as it progressed. First, it was recognized that some sources did not make the cut because of the thesis timescale constraint, but with a slightly longer period of monitoring could have their masses derived to a high level of accuracy. In particular, the timescale cut introduced an obvious bias to sources with higher predicted masses, or earlier spectral types. Therefore, we added three objects included in Burgasser et al. (2007) to the NIRC2 monitoring program to provide initial epochs of data for future mass determination. These three objects are shown on Figure 10 in blue. All three were of spectral type L or T (we did not add additional M dwarfs to our sample because of the large number of M dwarfs included in our initial sample). All three had a >50% probability of a precise dynamical mass estimate in our initial Monte Carlos. These added sources are given in Table 2. Two additional sources were added to the sample that were discovered by Reid et al. (2006) after the initial publication of Burgasser et al. (2007). For these sources, we have calculated the likelihood that they will yield precise mass estimates by 2012. We do not include these sources on Figure 10 because the simulations we performed were different from our initial simulations, but we found that both sources had a >50% chance of yielding a precise mass estimate by 2012. We therefore added these two sources to our astrometric program as well. They are also listed in Table 2.

3. Observations

3.1. Astrometric Data

Targets in our sample were observed astrometrically beginning in May of 2006. Observing was conducted twice a year between 2006 May and 2009 June UT using the Keck II 10 m telescope with the facility LGS AO system (Wizinowich et al. 2006; van Dam et al. 2006) and the near-infrared camera, NIRC2 (K. Matthews 2009, in preparation). The AO system, which is also used for obtaining radial velocities (see next section), uses the sodium laser spot (V$\sim$10.5) as the primary correction source for all but two systems. Tip/tilt references are listed in Table 3. NIRC2 has a plate scale of 9.963 ± 0.005 mas pixel^{-1} and columns that are at a PA of 0.13 ± 0.02^o relative to North (Ghez et al. 2008). The observing sequence for each object depended upon the brightness of the target, whether observations in multiple filters had been previously made, and whether the target was actually resolved into two components at that epoch. If the binary was not resolved, we could only obtain upper limits on the separation, which do not require a full observing sequence to estimate. We generally tried to take at least nine individual exposures on each target, though sometimes due to time constraints less exposures were taken. Table 3 gives the log of all imaging and photometric observations, listing when each target was observed, the filters through which it was observed and the exposure time and number of images taken in each filter, and the tip/tilt reference source used for each target. In many cases, the brown dwarf targets were bright enough to serve as their own tip/tilt reference, even though they are not bright enough for natural guide star observations.

With only a few exceptions, all data used for astrometry were taken through the K-prime (λ_o = 2.124 μm, $\Delta\lambda$ = 0.351 μm) band pass filter. Data in both the J Band (λ_o = 1.248 μm, $\Delta\lambda$ = 0.163 μm) and H band (λ_o = 1.633 μm, $\Delta\lambda$ = 0.296 μm) were also taken at some point for most targets to provide a complete set of spatially resolved, near-infrared photometry. The images were generally taken in a three position, $2\farcs5$ x $2\farcs5$ dither box, with three exposures per position (avoiding the lower left quadrant of NIRC2, which has significantly higher noise than the other three), which allowed sky frames to be generated from the images themselves. In addition, the wide dither box insures the incorporation of known residual distortion (Ghez et al. 2008, Yelda et al. 2009) in the camera into our final astrometric uncertainties.

3.2. Radial Velocity Data

Twelve objects in our astrometric sample were also observed using the NIR spectrograph NIRSPEC on Keck II (McLean et al. 2000) in conjunction with the LGS AO system (NIRSPAO). We used the instrument its in high spectral resolution mode, selecting a slit $0\farcs041$ in width and $2\farcs26$ in length in AO mode. We elected to observe in the K band, with a particular interest in the densely populated CO band head region (~2.3 μm), necessitating an echelle angle of 63 degrees and a cross-disperer angle of 35.65 degrees. The resolution in this setup is R~23000, and the total wavelength coverage spans 2.044 to 2.382 μm (orders 37-32), with breaks at 2.075-2.100 μm, 2.133-2.160 μm, 2.193-2.224 μm, 2.256-2.291 μm, and 2.325-2.362 μm, where portions of the K band orders were beyond the edges of the detector.

The components of each binary were rotated so that both fell simultaneously on the high resolution slit, which is rotated at an angle of 105.9^o with respect to north. Typical observations consisted of four spectra of both components, each with 1200 second integration times, taken in an ABBA dither pattern along the length of the slit. In a few cases, more than four spectra were taken or a slightly different integration time was used, depending on the brightness of the object. Table 4 gives the log of our spectroscopic observations, listing the targets observed, the date of observation, the number of spectra, and the integration time for each spectrum. Each target observation was accompanied by the observation of a nearby A0V star to measure the telluric absorption in the target spectra.

4. Data Analysis

4.1. Astrometric Data Analysis

The NIRC2 data was initially processed using standard data reduction techniques for near-infrared images. Frames at differing dither positions were subtracted from each other to remove sky background, followed by the removal of bad pixels, division by a flat field, and correction for optical distortion with a model provided in the pre-ship review document[1] using standard techniques in IRAF and IDL. The binaries were then shifted to a common location in all frames and the images were median combined. Astrometry and flux ratios were obtained using the IDL package StarFinder (Diolaiti et al. 2000). An empirical point-spread function (PSF) is required by the StarFinder fitting algorithm. In the case of two sources, a suitable PSF star falls within the field of view of the NIRC2 observation of the source. However, in the majority of cases, no such PSF source is in the field of view. For these observations, we use either an image of a single star taken near in time to the images of the binary, or if no suitable single star was imaged, we use an idealized Keck PSF degraded to the calculated strehl ratio of the observation for PSF fitting. For this last case, the PSF is generated by first convolving an the idealized PSF with a Gaussian, such that the core is broadened to the appropriate FWHM. Next, a simulated "halo" is generated by adding a Gaussian with FWHM of $0\farcs5$ (average seeing halo at Keck), normalized such that the resulting strehl ratio matches the observations. Internal statistical measurement errors were calculated by fitting the components of the binaries in all individual images that contributed to the combined images and finding the RMS of the values derived therein.

Additional systematic uncertainties need to be accounted for when determining the final astrometric and photometric measurements for each of binary. First, absolute uncertainties in the plate scale and position of north given above are accounted for in all astrometry. A further, more complicated, source of uncertainty stems from using a PSF that is not imaged simultaneously with each binary, introducing systematic uncertaintie s in both astrometry and photometry. In particular, the variability of the AO performance over a given night generates time variable PSF structure that can contribute to slight offsets in astrometry and photometry. To estimate the additional uncertainty due to imperfect PSF matching, we performed simulations in which 1000 artificial binaries were generated using images of an image single sources with separations and flux ratios spanning the range observed for our sources. These artificial binaries were then fit with Starfinder using either a separate single source from the same night or simulated source as the PSF. This exercise was performed for every night in which observations were taken for both PSF types. Examples of the results of these simulations is shown in Figure 10 for the case of an observed PSF, and in Figure **??** for the case of a simulated PSF (from the night of 2006 May 21). We find in all simulations that median offsets between input and fitted separations are an exponentially decreasing function of the separation, meaning that fits to tighter binaries were more discrepant from the correct values than

---

[1] http://www2.keck.hawaii.edu/inst/nirc2/preship_testing.pdf

those to wide binaries. We also find that due to variable structure in AO PSF halos (even after accounting for pupil rotation), the offset in fitted position angle is a function of the position angle of the binary. Finally, the median offset in fitted flux ratio with res pect to the input flux ratio was essentially constant for all separations and position angles. Therefore, for every measurement of each target, we compute the necessary uncertainties from imperfect PSFs based on the relationships detailed above, taking the median values of the measured of fsets as the magnitude of the additional uncertainty. The PSF uncertainties have the greatest impact on the tightest systems or on nights when the performance was poor (strehl ratios $\lesssim$20%). In about 25% of our measurements, this PSF uncertainty is larger than our statistical uncertainty. The astrometry and relative photometry for all sources at all epochs is given in Table 5. Those sources that were unresolved in our observations have upper limits on binary separation only. Uncertainties in Table 5 are listed separately for the purpose of illustrating the relative magnitude of each source of uncertainty, but for all further analysis, we add them together in quadrature to give a final uncertainty.

4.2. Spectroscopic Data Analysis

The basic reduction of the NIRSPAO spectra was performed with REDSPEC, a software package designed for NIRSPEC[2]. Object frames are reduced by subtracting opposing nods to remove sky and dark backgrounds, dividing by a flat field, and correcting for bad pixels. Spectral orders are spatially rectified by fitting the trace of each nod of telluric calibrators with third order polynomials, and then applying the results of those fits across the image. A first-order guess at the wavelength solution for the spectra is obtained using the etalon lamps that are part of the lamp suite of NIRSPAO (this is used as a starting point for our derivation of the true wavelength solution). Order 33 has very few OH sky lines or arc lamp lines to use for this purpose. To obtain the correct values of the wavelengths for the etalon lines, we followed the method described by Figer et al. (2003). The wavelength regime that Order 33 encompasses was found to be between ~2.291 and ~2.325 μm. The output we used from REDSPEC was therefore a reduced, spatially rectified and preliminarily spectrally rectified fits image of order 33.

As these systems are fairly tight binaries, cross-contamination can be an issue when extracting the spectra. This made the simple square-box extraction provided in REDSPEC unsuitable for these observations. We therefore extracted the spectra by first fitting a Gaussian to the trace of one component of the binary and subtracting the result of this fit from the frame to leave only the other component. The width of the Gaussian is allowed to vary with wavelength, although over the narrow wavelength range in covered by order 33, the variation is small. Typically the binaries are separated by more than a FWHM of this Gaussian, making the fit of the bright stars' trace unbiased by the other. In the few cases where the traces were separated by less than about 7 pixels, the fitted FWHM would be artificially widened due to the presence of the companion. In these cases,

---

[2] http://www2.keck.hawaii.edu/inst/nirspec/redspec/index.html

we fixed the FWHM of the Gaussian to that measured for other, more widely separated sources observed on the same night. After the trace of one component was fitted and subtracted from the frame, the trace of the remaining component was then also fit with a Gaussian for extraction. We normalized this Gaussian such that the peak was given a value of one and corresponded to the peak of the trace in the spatial direction. We then weighted the flux of each pixel by the value of the normalized Gaussian at that pixel location, and then added these weighted fluxes together to get our final extracted spectrum. We do not remove telluric absorption from our order 33 spectra because telluric lines are used for radial velocity determination.

To measure radial velocities from our extracted spectra, we use the method detailed extensively by Blake et al. (2007) and White et al. (2009). Namely, using a combination of a spectral template appropriate for each target and a model of the telluric absorption of the atmosphere, it as possible to determine radial velocities for NIRSPEC spectra accurate to better than 1 km/s. Each extracted spectrum is therefore fit with a model in which the free parameters are the rotational velocity ($V\ sin\ i^3$), the PSF of the spectrograph (assumed to be a Gaussian where the width is the free parameter), the flux normalization, and the wavelength solution. The model thus consists of a spectral template that has been convolved with a rotational broadening kernel, shifted by some radial velocity, multiplied by a telluric model, and then convolved with a Gaussian PSF. The details of this fitting procedure are described in Blake et al. (2007). The synthetic spectral templates we used for our fitting are derived from the PHOENIX atmosphere models (Hauschildt et al. 1999). We use order 33 templates of the appropriate temperature for each source. This fitting procedure also has known degeneracies between derived $V\ sin\ i$ and temperature, as lowering the temperature or increasing the $V\ sin\ i$ have similar effects on the lines in the CO bandhead. We therefore use multiple templates spanning 300 K in temperature to determine the systematic uncertainty in radial velocity due to our synthetic template. We find that this systematic amounts to approximately ∼0.2-0.3 km/s for most targets. The measured radial velocities from this method are reported in Table 6. In Figures 10 through **??**, we show example fits for each of the sources with spectroscopic observations.

5. Orbital Analysis

5.1. Orbital Parameters from Relative Motion

To derive total mass estimates from relative orbital solutions for our sources, we combine our astrometric measurements from Section 4.1, previous astrometry reported in the literature, and the relative radial velocity between the components as determined in section 4.2. As described in Ghez et al. (2008), our model for an astrometric orbit always contains six free parameters:

---

[3] While this method has been shown to produce reliable radial velocities, the $V\ sin\ i$'s have known systematics that are perhaps due to an additional degeneracy with PSF

period (P), semi-major axis (a), eccentricity (e), time of periapse passage (T_o), inclination (i), position angle of the ascending node (Ω), and longitude of periapse passage (ω). We can remove the degeneracy in the values of Ω and ω which exists without information in this third dimension for the 11 of our 15 sources that have radial velocity information. The radial velocity data also allows distance to be a free parameter in the fit for those sources without a previously-measured parallax (5 systems). For those systems with a parallax measurement (9 systems), we do not allow distance to be a free parameter, but rather we constrain it to be consistent with the parallax distance and its uncertainties. The uncertainties on parallax measurements are smaller than those from fitting for distance as a free parameter, and the values are consistent in all cases. The distances, either used or derived in our fits, are given in Table 7. In the case of one system, 2MASS 0920+35, we had neither radial velocities nor a parallax measurement, so we use instead the photometric distance as determined from the relationship in Cruz et al. (2003), which is based on J band photometry and spectral type (here assumed to have an uncertainty of ±2 spectral subclasses). The best fit orbital parameter values are found by minimizing the total χ^2, which is found by summing the χ^2 of each data type ($chi^2_{tot} = \chi^2_{ast} + \chi^2_{rv}$; see Ghez et al. (2008) for more details on this fitting procedure).

After the best fit is determined, the uncertainties in the orbital parameters are found via a Monte Carlo simulation. First, 10,000 artificial data sets are generated to match the observed data set in number of points, where the value of each point (including the distance when it was not being fit for) is assigned by randomly drawing from a Gaussian distribution centered on the true value with a width corresponding to the uncertainty on that value. Each of these artificial data sets is then fit with an orbit model as described above, and the best fit model is saved. The resulting distribution of orbital parameters represents the joint probability distribution function of those parameters. We obtain the uncertainties on each parameter as in Ghez et al. (2008), where the distribution of each parameter is marginalized against all others and confidence limits are determined by integrating the resulting one-dimensional distribution from the best fit out to a probability of 68%. On occasion, when one or more parameters are not well-constrained, the best fit value does not correspond to the peak of the probability distribution. However, in almost all cases the best fit value for a parameter is within 1σ of the peak. The few fit parameters in which this is not the case are normally represented by bifurcated or poorly constrained flat distributions (see for example the distributions of e and ω for 2MASS 1847+55 AB, Figure **??**).

The resulting best-fit orbital parameters and their uncertainties are given in Table 7. The astrometric orbital solutions are drawn in conjunction with both the astrometric and relative radial velocity data in Figures 10-**??**. The dotted blue lines represent the 1σ range of separations and relative radial velocities allowed at a given time based on the orbital solutions from the Monte Carlo. The distributions of orbital parameters for all sources are shown in Figures 10-**??**. The shaded regions on the histograms show the 1σ ranges of each parameter. If the distances were sampled from previous parallax measurements, they are denoted with a red histogram. These figures are alphabetically ordered based on the sources' names.

5.2. Orbital Parameters from Absolute Motion

For 6 systems in our sample, sufficient absolute radial velocity measurements (at least 3) have been made and their relative orbits have been constrained enough to derive the first estimates of their absolute orbits, and hence the individual masses of the binary components. Common parameters between absolute and relative orbits, namely the P, T_o, e, and ω make it possible to only have to fit three free parameters: the semiamplitudes of the velocity curve for each component ($K_{Primary}$ and $K_{Secondary}$) and the systemic velocity (γ). We also have the additional constraint that $K_{Primary} + K_{Secondary} = 2\pi$ a sin$i$ / P (1 - $e^2)^{1/2}$. Since both inclination and semi-major axis are also constrained by the relative orbital solutions, this provides an additional constraint on the possible values of K, and hence the mass ratio, making it possible to eliminate $K_{Secondary}$ as a free parameter.

To first obtain the best fit solution for these parameters, we use our radial velocities from Table 6 and fix the values of P, a, T_o, e, i, and ω to perform a least-squares minimization between the equations for the spectroscopic orbit of each component and our data. We fully map χ^2 space (where in this case $\chi^2_{tot} = \chi^2_{Primary} + \chi^2_{Secondary}$) by first sampling randomly 100,000 times from a uniform distributions of $K_{Primary}$ and γ that are wide enough to allow mass ratios between 1 and 5 (where $M_{primary}$ / $M_{Secondary}$ = $K_{Secondary}$ / $K_{Primary}$) for all sources except LHS 2397a AB, for which we allow for mass ratios between 1 and 10. This imposed range is validated based on the approximate spectral types of the components, none of which imply very large mass ratios for our binaries. Due to the larger difference in the spectral type of the components of LHS 2397a AB, we chose to be conservative and allow for the larger mass ratio range. Upon obtaining these initial χ^2 maps, we narrow our sampling range around the region of minimum χ^2, allowing for parameters within 3σ, based on $\Delta\chi^2$, of the original best fit. We again sample 100,000 times within this new range. This process is continued until we are satisfied that we have found the best fit parameters by fully mapping χ^2 space to enough precision that our best fit values do not change to within more than 1σ as determined by the range of parameters from fits with $\chi^2 \leq \chi^2_{BestFit} + 1$.

To determine the uncertainties on our fit parameters, we again perform a Monte Carlo simulation. We use the distributions of P, a, T_o, e, i, and ω derived from our astrometric orbit Monte Carlo as inputs into the fits to account for the uncertainty in these parameters. We also then resample our radial velocity measurements to generate 10000 artificial data sets such that the value of each point is assigned by randomly drawing from a Gaussian distribution centered on the true value with a width corresponding to the uncertainty on that value (as was done with the astrometric data). We then find the best fit solution for each of these data sets (coupled with the sampled parameters from the astrometric fits). As with the astrometric orbit, we find the uncertainties by marginalizing the resulting distribution of each parameter against all others and integrating the resulting one-dimensional distribution from the best fit out to a probability of 68%.

The resulting best-fit orbital parameters for the absolute motion and their uncertainties are given in Table 8. The absolute orbital solutions are drawn with the absolute radial velocity data in Figures 10-**??** and the distributions of orbital parameters for all 6 sources are shown in Figures **??**-**??**. By combining our mass ratio distribution derived with this data with the total system mass derived in Section 5.1, we have computed the first assumption-free estimates of the individual masses of the components for 5 of these 6 systems. These individual masses are given in Table 8.

5.3. Individual System Remarks

5.3.1. 2MASS 0746+20AB

2MASS 0746+20 AB originally had its total system mass derived by Bouy et al. (2004). Those authors found a total mass of $0.146^{+0.016}_{-0.006}$ $M_{\odot}$. Our new astrometric and radial velocity data has allowed us to improve this total mass estimate by a factor of 4 to 0.151 ± 0.003 $M_{\odot}$, or to a precision of 2%. This measurement represents the most precise mass estimate for a VLM binary yet determined. Our individual mass estimates are the first for this system and the first for a binary L dwarf.

Though we do not yet have sufficient precision in our individual mass measurements for this system to resolve the debate on whether the secondary is a brown dwarf or a low mass star (Gizis & Reid 2006), our measurements can shed some light on the result by Berger et al. (2009), in which a radius for the primary component of the system was estimated using periodic radio emission from the system. Based on the assumptions that the emission was coming from the primary, that the previously reported, spatially unresolved *V sin i* measurements reflected the *V sin i* of the primary, and that the rotation axis of the primary was aligned with the binary inclination, Berger et al. (2009) derive a radius of 0.76 ± 0.10 R_{Jup} for this system. These authors note that this radius is about 30% smaller than expected based upon the models. Though we do not report definitive *V sin i* measurements for each component from *spatially resolved* spectra, providing an assumption free value for this type of analysis, preliminary work comparing all K band spectra across multiple orders for this system to high resolution atmosphere models suggests that the rotational velocity of the secondary component may be ∼35 km/s. If it were the case that the radio emission were coming from this component of the binary instead of the primary (which does seem to have *V sin i*∼ 25 km/s), this would increase the derived radius to something more in line with predictions. We leave the full analysis of our spectroscopy to derive quantities such as spatially resolved *V sin i* for a future publication.

5.3.2. 2MASS 0850+10AB

2MASS 0850+10 AB has two independent measurements of its distance via parallax. The first was from Dahn et al. (2002), 25.6 ± 2.5 pc and the second was from Vrba et al. (2004), 38.1 ± 7.3 pc. These values are about 1.5σ discrepant from each other, a fact noted by Vrba et al.

(2004), although those authors did not know the cause of this discrepancy. We performed a full Monte Carlo analysis as described in section 5.1 using both estimates for distance, which effects the total mass in the relative orbit fit. We choose to present the values of mass as derived from the Vrba et al. (2004) distance estimate here because it has larger uncertainties. Since the current uncertainties in the period and semimajor axis for this system are large, the impact of choosing one distance over the other is negligible.

5.3.3. 2MASS 0920+35AB

2MASS 0920+35 AB was discovered to be binary by Reid et al. (2001) using HST. A follow-up monitoring campaign of the system was performed by Bouy et al. (2008) using both HST and the VLT in conjunction with their facility AO system. In each of the five observations performed by Bouy et al. (2008), the system was unresolved. These authors postulated that the binary was therefore perhaps on a highly inclined orbit with a period of roughly 7.2 years. When our monitoring of the system began in 2006, the system was again resolved, and remained resolved for all of our measurements until our most recent one in 2009 June. We therefore utilize both the resolved and unresolved measurements to perform our orbit fits. First, we fit the resolved astrometric measurements for relative orbital parameter solutions as described in Section 5.1. We then took the output orbital solutions for those trials and calculated predicted separation of the binary at each of the epochs in which it was unresolved - if the predicted separation was above the detection limits given by Bouy et al. (2008) or our 2009 June 10 measurement, it was thrown out. These unresolved measurements therefore provided tighter constraints on the orbital parameters for this system.

The results of the Monte Carlo simulation for this system are shown in Figure 10. As shown in this figure, the resulting distribution of periods has a strong bifurcation, whereby ∼45% of the solutions favor an orbital period of ∼3.3 years and a very high eccentricity, and 55% favor the best fit solution of ∼6.7 years and more modest eccentricities. Since these solutions are nearly equally preferred but quite distinct, we display the best fit of both solution families in Figure **??**, with the shorter period solution plotted in green. The two solution sets cause the current mass uncertainty to be fairly high. However, an additional astrometric measurement before mid-2010 should distinguish between the two sets, as it will not be resolved for periods of ∼6.7 years but it will be resolved for periods of ∼3.3 years. Further, we have found the inclination of this system to be nearly edge on, meaning it has a non-negligible chance of being an eclipsing system (see section 9).

5.3.4. 2MASS 1534-29AB

The first derivation of the orbit of 2MASS 1534-29AB was performed by Liu et al. (2008), where they calculated a total system mass of 0.056 ± 0.003 $M_\odot$. By combining our astrometry with that reported by Liu et al. (2008), we find a slightly higher, but consistent, total system mass of 0.060 ± 0.004 $M_\odot$. We note that if we perform our analysis on only the astrometry given in Liu et al. (2008), we obtain a mass of 0.056 ± 0.004 $M_\odot$, which is a slightly higher uncertainty than what is reported in that work.

5.3.5. 2MASS 2140+16AB and 2MASS 2206-20AB

We have acquired sufficient radial velocity data to make the first calculations of the absolute orbits of these systems. However, the uncertainty in the radial velocities is comparable to the distance between the values. Because of this, the best fit is typically the one that minimizes $K_{Primary}$, which in turn maximizes $K_{Secondary}$. This leads to mass relatively high predicted mass ratios. Though there is some spread in the value of mass ratio, as shown in Figures **??** and **??**, the mass ratio is quite peaked at this high value. This leads not only to mass values for the secondary that are likely too low given their approximate spectral types, but also uncertainties that are too small for the secondary given the uncertainty in the mass of the primary. For these two systems, we therefore extend the uncertainty in the secondary mass by combining in quadrature the uncertainty in the total system mass and the uncertainty in the mass of the primary component. We have noted that we have taken this approach in Table 8, and have shaded the histograms in Figures **??** and **??** to reflect our chosen uncertainties. Though these first estimates of individual mass are fairly uncertain, they will improve with continued monitoring of these systems.

5.3.6. GJ 569Bab

The first derivation of the relative orbit of GJ 569Bab was performed by Lane et al. (2001), and was followed with improvements by Zapatero Osorio et al. (2004) and Simon et al. (2006). The work of Zapatero Osorio et al. (2004) and Simon et al. (2006) also contained spatially resolved, high resolution spectroscopy measurements for this systems, which is one of two targets in our sample that is an NGS AO target. Zapatero Osorio et al. (2004) derived the first estimate of the individual component masses of this system using their J band spectroscopic measurements. Simon et al. (2006) made their radial velocity measurements in the H band and noted that their derived center of mass velocity (-8.50 ± 0.30 km/s) is discrepant from that of Zapatero Osorio et al. (2004, -11.52 ± 0.45 km/s) by ~3 km/s. Simon et al. (2006) postulate that this stems from the choice of lines used to make their measurements. Zapatero Osorio et al. (2004) use the K I doublet location referenced to laboratory wavelengths while Simon et al. (2006) perform cross-correlation of their full order 48 (λ = 1.58 - 1.60 μm) and 49 (λ = 1.55 - 1.57 μm) spectra with spectral templates.

Simon et al. (2006) also note that the relative radial velocities are consistent with what is predicted based on astrometry.

We now note that our spectra, measured in the K band and fit for radial velocity as described in Section 4.2, appear to be systematically offset from both the measurements of Zapatero Osorio et al. (2004) and Simon et al. (2006). We find a center of mass velocity using just our data points of -8.05 ± 0.20 km/s, which is the most consistent of the three sets of measurements with that of the M2V primary of this tertiary system (-7.2 ± 0.2 km/s). We find, as shown in Figure **??**, that the relative velocities are consistent with what is expected for the relative orbit. Thus the velocity differences truly seem to be driven by an offset in their absolute value. It is possible that these velocity offsets may be related to the orbit of this binary around GJ 569A. To examine whether this is the case, we plot the measured systemic velocity by each of the three studies versus the median date of observation. This is shown in Figure 10. While the difference between our measurement and that of Simon et al. (2006) could be consistent with orbital motion around GJ 569A, the large acceleration in radial velocity implied between the Zapatero-Osorio et al. (2004) measurement and the other two points is likely too large to be caused by orbital motion. For GJ 569Bab, which is separated by ~50 AU from GJ 569A, to have a radial velocity change of ~2 km/s between 2004 and 2001 would require an orbital eccentricity of >0.99 and a date of periapse passage between 2001 and 2005, an unlikely configuration. Thus, the difference here is likely due to the absolute radial velocity calibration issues described in Simon et al. (2006).

In order to use all the radial velocity measurements to calculate individual masses, we opt to shift all data points from Zapatero-Osorio et al. (2004) and Simon et al. (2006) such that their center of mass velocity is consistent with ours. We also increase the uncertainties in these values such that they incorporate the uncertainties in our value of systemic velocity and in the systemic velocity derived in each work, which we combine in quadrature. We then use these shifted velocities in conjunction with our measurements to derive the absolute orbit, which is shown in Figure **??**. The application of this offset results in a very nice fit with a reduced χ^2 of 0.56. We find a mass ratio of 1.4 ± 0.3, which is lower than the value of 5.25 found by Simon et al. (2006). Those authors postulated that since the mass of the primary appeared to be so much higher than that of the secondary, that the primary may be a binary itself (something potentially suggested by the wider lines seen in GJ 569Ba). Our values of primary and secondary mass suggest that the sources actually have fairly similar masses of 0.073 ± 0.008 $M_\odot$ and 0.053 ± 0.006 $M_\odot$. We cannot, however, definitively rule out that GJ 569Ba is comprised of two components, as suggested Simon et al. (2006), although this possibility is more unlikely given that we find the mass of GJ 569Ba to be lower than those authors found.

5.3.7. HD 130948BC

The first derivation of the relative orbit of HD 130948BC was performed by Dupuy et al. (2009a), where they calculated a total system mass of 0.109 ± 0.003 $M_\odot$. By combining our astrometry with that reported by Dupuy et al. (2009a), we find an identical, but slightly more precise, total system mass of 0.109 ± 0.002 $M_\odot$. Although we only have one radial velocity measurement for this system, which is insufficient to calculate individual masses for the components, our radial velocity measurement allows us to resolve the degeneracy in the values of ω and Ω.

5.3.8. LHS 2397a AB

The first derivation of the relative orbit of LHS 2397a AB was performed by Dupuy et al. (2009b), where they calculated a total system mass of $0.146^{+0.015}_{-0.013}$ $M_\odot$. Combining our astrometry with that reported by Dupuy et al. (2009b), we also find a consistent total mass of $0.144^{+0.013}_{-0.012}$ $M_\odot$. Performing our analysis on just the astrometry given in Dupuy et al. (2009b), we find a slightly different, but consistent, mass of $0.150^{+0.014}_{-0.013}$. Dupuy et al. (2009b) also use their results in conjunction with a bolometric luminosity and the evolutionary models (both Burrows et al. (1997) and Chabrier et al. (2000)) to derive the individual component masses. Here we derive the first individual mass estimates free of assumptions, which allows for a direct comparison to the models. We find component masses of 0.09 ± 0.06 $M_\odot$ for the primary and 0.06 ± 0.05 $M_\odot$ for the secondary. The well-mapped velocity curve of the primary allows for this absolute orbit to be relatively well-defined with a comparable number of radial velocity measurements to other sources that do not yet have well-defined absolute orbits.

6. Bolometric Luminosity and Effective Temperature Derivation

In order to compare the predictions of theoretical evolutionary models to our dynamical mass measurements, estimates of both the effective temperature and bolometric luminosity are required. With input of these parameters, the evolutionary models can be used to derive a mass and an age for a source. Thus, we must derive these parameters for all binary components.

Our method for deriving both of these quantities relies on the spatially resolved photometry we have obtained with our imaging data. In our NIRC2 data, we have measured the flux ratio of the binary components in the J, H, and K' bands, given in Table 5. We convert these flux ratios into individual apparent magnitudes using the unresolved photometry for these sources from 2MASS (Cutri et al. 2003). The apparent magnitudes can then be converted into absolute magnitudes using the distances from Table 7. We also find the absolute magnitudes for each system in all other photometric bands for which spatially resolved measurements exist. The majority of these measurements were made in the optical with HST. The absolute photometry for all sources is given in Table 9. References are given for photometry taken from the literature.

The determination of effective temperature for these sources is complex. Generally speaking, spectral type is not as accurate a proxy for the temperature of brown dwarfs as it is amongst hydrogen burning stars, with derived temperatures spanning several hundred Kelvin for different sources of the same spectral type (Leggett et al. 2002, Golimowski et al. 2004, Cushing et al. 2008). We therefore opt to perform spectral synthesis modeling using atmospheric models on each source individually, which allows for lower temperature uncertainties for most objects than would be achieved by using a temperature vs. spectral type relationship. Though this introduces a model assumption into our comparison of these sources to evolutionary models, we can use our mass estimates to determine the consistency of the atmospheric and evolutionary models with each other. For our sources of late M to L spectral types, we derive effective temperature using the DUSTY form of the PHOENIX atmosphere models (Hauschildt et al. 1999). These models, in which all refractory elements present in the atmospheres of these objects are assumed to form dust grains, enveloping the synthetic atmosphere in thick dust clouds, have been shown to reproduce the colors and spectra of these types of objects quite well. Updated opacities and grain size distributions have improved the correspondence of these models to observations (Barman et al. in prep, Rice et al. 2009). Among the 30 sources in our dynamical mass sample, 21 have late M to early L spectral types for which the DUSTY models are appropriate. For the two sources in our sample of mid-T spectral type, we use the COND version of the PHOENIX atmosphere models, which have been shown to reproduce the colors and spectra of T dwarfs well. In these models, all refractory elements have been removed from the atmosphere through an unspecified "rain out process", resulting in dust free atmospheres and blue near infrared colors.

Since temperature can be the most effectively constrained by comparing synthetic atmosphere data over a broad range in wavelengths, we elect to use our spatially resolved photometry to perform the spectral synthesis modeling. Very high resolution versions of the DUSTY models and the wavelength and bandpass information for each of our photometric measurements in Table 9 were used to generate a grid of synthetic photometry for objects with T_{Eff} = 1400 - 4500 K for DUSTY and T_{Eff} = 300 - 3000 K for COND, with log g = 4.0 - 5.5. This range of surface gravity should be appropriate for all sources in our sample (McGovern et al. 2004, Rice et al. 2009). We then use this grid to fit the measured photometry for each source, allowing for interpolation between finite grid points. Because the flux values in the grid are defined at the surface of the source, they must be scaled by the radius of the source - thus, we also fit for the radius as a scaling factor. Uncertainties in the derived temperature and radius are then calculated via Monte Carlo simulation, in which 10000 new photometric data points are generated by sampling from a Gaussian distribution centered on each apparent magnitude with a width given by the uncertainty in each magnitude. The apparent magnitudes are then converted to absolute magnitudes using a distance sampled from a Gaussian distribution centered on the values given in Table 7 These datapoints are then fit in the same manner, and confidence limits on effective temperature and radius are then calculated by integrating our resulting one-dimensional distribution from the best fit out to a probability of 68%. The best fit SEDs from the atmosphere models are shown overplotted on the photometry for each source in Figures 10 through **??**. The one dimensional PDFs for temperature and radius are show in Figures 10 through **??**. Although surface gravity is also allowed to vary, we do not have sufficient photometric precision to distinguish between values of surface gravity for these field binaries, and the distributions of surface gravity are essentially flat. In Figure 10, we plot our derived effective temperatures as a function of spectral type. The scatter seen amongst the data points stresses the intrinsic scatter in effective temperature with spectral type for these objects. We combine the results of Golimowski et al. (2004), Cushing et al. (2008), and Luhman et al. (2003) to demonstrate previous measures of temperature versus spectral type. This relationship is plotted in red on Figure 10, along with error bars representing the range of allowed values by these works. This comparison demonstrates that in the cases where our photometry is well-constrained, the temperatures we derive using atmospheric modeling have much lower uncertainties than we would be able to obtain using spectral type.

Because we have a derived temperature and radius, we can also calculate the PHOENIX model predicted bolometric luminosity. However, this would also generate a model-dependence in our value of luminosity. Instead, we elect to determine bolometric luminosity using the K band bolometric corrections provided by Golimowski et al. (2004). These corrections are a function of spectral type and were derived using sources with photometric measurements over a broad range of wavelengths, integrating under their calculated light curves. The only assumption required to use these corrections is that spectral type is a good proxy for K-band bolometric corrections. In contrast to predicted effective temperature, the change in the K band bolometric correction with spectral type is quite gradual with lower scatter. In addition, Liu et al. (2008) and Dupuy et al. (2009b) showed that by deriving bolometric luminosities through light curve integration of four sources, they obtain values fully consistent with those they would have obtained using the bolometric corrections of Golimowski et al. (2004). To be conservative, we assume an uncertainty in the spectral type of each source of ±2 spectral subclasses to determine our uncertainty in bolometric correction. Even with this assumption, the bolometric correction uncertainty is never the limiting factor in our bolometric luminosity uncertainty (generally the uncertainty is dominated by the distance uncertainty). Our estimates of bolometric luminosity from using these bolometric corrections are given in Table 9. To demonstrate the correspondence between the luminosities calculated in this way and the luminosities predicted by the atmosphere models, we plot the values against each other in Figure 10. All points fall along the line of 1:1 correspondence (plotted in red). We therefore feel confident that our model-independent estimates of bolometric luminosity are appropriate for these sources.

In principle, our high resolution spectroscopy can also be used to calculate effective temperature. However, the narrow wavelength coverage in the near infrared provides relatively loose constraints on temperature, with many temperatures being allowed for by our K band spectra. We have, however, performed a few comparisons of our K band spectra to the same models we use for the photometric fitting and find that the results are consistent, with the photometry providing lower uncertainties than the spectroscopy. Ultimately, the best temperatures would be derived by fitting a combination of the photometry and the spectroscopy. However, such fitting has known challenges associate with how data is weighted (Cushing et al. 2008). In the future, we hope to perform fitting of this kind, combining all spectral data.

For the seven sources in our sample in the L/T transitions region, we must take a different approach to obtaining effective temperatures. The DUSTY and the COND models can be thought of as boundary conditions to the processes occurring in brown dwarf atmospheres, meaning each atmosphere is either fully dusty or completely dust free. There is no transitional dust phases represented in the current versions of these models. Though we attempted to fit sources in this region via the method described above with both models, we obtained very high temperatures and unphysically small radii. Therefore averaging the predictions of the two models does not work. For these sources, we elect to use the bolometric luminosity of the source and assume a radius with a large uncertainty, chosen to conservatively span the values derived in our atmospheric model fitting (1.0 ± 0.3 R_{Jup}). A radius in this range is also what is expected for these objects theoretically. In Figure 10, we plot the radii from our fits as a function of spectral type. Although there is a lot of scatter in this relationship due to the mixed ages in our sample, the large uncertainty we have assumed for radii at the L/T transition region should account for this variation. The result of assuming a radius is higher temperature uncertainties for these objects. All derived temperatures and radii are given in Table 9.

7. Eccentricity Distribution

Using the distributions from our Monte Carlo simulations in section 5.1, we can begin to examine the bulk orbital properties of our sample of VLM objects. In particular, we can determine the distribution of eccentricities for our sample (9 of which are constrained to better than 30%), which may shed light on the formation of VLM binaries.

To determine our eccentricity distribution, we performed a Monte Carlo in which we randomly sampled one value of eccentricity per source from the distributions in Section 5.1. In each trial, the total number of sources per bin was calculated in bins of width 0.1 over the range of values from 0 to 1. We performed 10,000 of these trials, which gave a distribution for each bin of the number of expected sources. This distribution provided a predicted number of sources in each bin along with an uncertainty. We then combined distributions such that the final bin width was 0.2. The resulting distribution for our 15 sources is shown in the right panel of Figure 10.

We find that our sources tend to have moderate to low eccentricities, with the number falling off towards high eccentricities. We have overplotted on Figure 10 the result found by Duquennoy & Mayor (1991) for solar-like field stars with periods > 1000 days (all sources in our sample meet this criteria except GJ 569B, which has a period of 865 days). These authors found that longer period systems showed an eccentricity distribution that went as $f(e) = 2e$, consistent with what is expected if the distribution is a function of energy only (Ambartsumian 1937). Our distribution does not appear to follow this trend. Duquennoy & Mayor (1991) also found that eccentricity appeared to be a function of period, with longer period systems tending towards higher eccentricities (albeit with fairly large scatter past the tidal circularization period of $\sim$10 days). We also examined the period as function of eccentricity. The relationship for our sample is shown in the right panel of Figure 10. We have overplotted the sources from Duquennoy & Mayor (1991) with periods greater than

865 days. Although we have fewer systems than those authors, our sample appears to be following the same trend, with eccentricity tending to increase as a function of period. A 2-dimensional K-S test between our distribution and the distribution from Duquennoy & Mayor (1991) shows that the two samples have an 11% chance of being drawn from the same distribution (therefore being consistent to within 1.6σ), suggesting the distributions are statistically consistent.

In our sample selection, we strove to minimize period in order to obtain mass estimates in a short timescale. We have therefore possibly preferentially selected systems with moderate to low eccentricities due to their relatively short periods. However, the right panel of Figure 10 shows that there are many systems in Duquennoy & Mayor (1991) of comparable periods to the majority of our sample that have higher eccentricities. An additional source of selection bias in our sample may stem from our assumptions during sample selection. Highly eccentric systems spend a long fraction of their orbit at wide separations. Binaries that had fairly wide separations at the time of their discovery tended to be cut through our sample selection process as described in Section 2. This could lead to highly eccentric systems being preferentially removed from our sample. With more time coverage, additional VLM systems will have their orbital solutions derived and help determine if this “overabundance” of low eccentricity systems is indeed a selection effect. If the overabundance is not a selection effect, it could have interesting implications for the formation and/or dynamical history of VLM binaries, and be another line of evidence in favor of the dynamical evolution of VLM objects being slightly different from that of stars (Konopacky et al. 2007b).

8. Comparisons to the Predictions of Evolutionary Models

We use our derived temperatures and bolometric luminosities to determine the model-predicted mass for each source in our sample. We consider both the Chabrier et al. (2000) evolutionary models, called DUSTY and COND, and the Burrows et al. (1997) evolutionary models (TUCSON). The DUSTY and COND evolutionary models are named as such because they use the boundary condition between the interior and the atmosphere provided by the DUSTY and COND atmosphere models, respectively. Thus the evolutionary and atmosphere models are not strictly independent. In comparing to the Chabrier et al. (2000) evolutionary models, we are consistently testing model predictions because we have used the same atmospheric models in our analysis. Our comparisons to the Burrows et al. (1997) models thus must be caveated in this regard, as we do not have access to the atmospheric models they employ. However, we still perform the comparison to test the correspondence of these models to our measurements, as the effect of the atmospheric model boundary condition should only have a minor impact on the evolutionary predictions (Chabrier & Baraffe 2004).

To do this comparison, we first interpolate over the surface defined by the grids of temperature, luminosity, mass, and age provided by the evolutionary models using the INTERPOLATE function in the SciPy package for Python. We then determine which temperature and luminosity point on the interpolated surface is the closest to our input value of temperature and luminosity. For the sources from late-M to mid-L, we calculate the predictions of the DUSTY version of the Chabrier et al. (2000) models, while for the T dwarfs we use the COND version on these models. For the L/T transition objects, we calculate the predictions of both sets of Chabrier et al. (2000) models. The Burrows et al. (1997, TUCSON) models do not assume a different atmospheric treatment for different spectral types and assume that dust species have condensed out of the atmosphere across the entire substellar regime. We therefore compare the predictions of these models to all objects in our sample. These comparisons provide the predicted mass and age for each source.

To determine the uncertainties in each model prediction of mass, we sample from temperatures and luminosities defined by the uncertainties in each for each sources, accounting for the correlations between bolometric luminosity and temperature (Konopacky et al. 2007a)[4]. The range of masses and ages predicted from this sampling, marginalized against the other parameters, provides our uncertainties. The values of mass predicted by each model is provided in Table 10. In the left panels of Figures **??** through **??**, we show the location of the components of each binary on an H-R Diagram, with the lines of constant mass for each model overplotted in different colors. For clarity, the isochrones are omitted.

The majority of the sources in our sample have little to no age information - hence, we test for coevality as opposed to correct age prediction by the models. For the two sources with age information, HD 130948 BC (∼500 Myr) and GJ 569Bab (∼100 Myr), the uncertainties on these ages are such that both models predict ages for these systems that are consistent with these values. For all sources in our sample, all binary components are coeval within the uncertainties for all models. Figure 10 shows the predicted ages of the binary components in the DUSTY and the TUCSON models plotted versus each other. A line of 1:1 correspondence is overplotted. The predicted coevality is apparent from the figure. The relatively large uncertainty in age estimates stems from the fact that the model isochrones become more closely packed at with increasing age. Because of this fact, empirical age estimates for field objects provide relatively weak constraints on the models.

Since our highest precision measurements are currently in total system mass, we can most effectively compare model predictions to these measurements. To do this, we add the model masses derived for each component together and add their uncertainties in quadrature. The combined mass predictions are also given in Table 10. We find that for 7 systems, all models underpredict the total system mass by greater than 1σ. These 7 systems have the smallest uncertainties in dynamical mass and primary component spectral types earlier than L4. For 7 systems, we find that all models considered predict masses that are consistent with the dynamical mass within 1σ. These systems all have mass uncertainties over 60%, and also generally higher temperature uncertainties. Finally, we find that the mass of one system is overpredicted by both models by greater than 1σ and is the

---

[4] In contrast to Konopacky et al. (2007a), we are not obtaining temperatures based upon the color of our systems. Our atmospheric model fits are only linked to bolometric luminosity through the K band magnitude, and thus the correlations between the two parameters are very weak in this study

only system with a mid-T spectral type.

To illustrate the apparent trend in mass discrepancy with spectral type, we have plotted the percent difference between the model prediction and the total dynamical mass for each model. These plots are shown in Figures 10 and **??**. It is clear that the discrepancies in total system mass peak for those sources with the earliest spectral types in our sample, reach a minimum at the L/T transition (though all sources in this region have fairly large uncertainties in dynamical mass), and then appear again for one T dwarf source.

We can test the predictions of the models a bit further by considering our handful of individual mass measurements. Although our individual mass measurements do not yet have the high precision we have achieved in total mass, we can already see for the most precise cases that the discrepancy holds. That is, for the primary components of 2MASS 2206-20AB, GJ 569Bab, and LHS 2397a AB (which have the highest precision in component mass), the models underpredict the mass. These three systems all have approximate spectral types of M8. We also see that the secondary components of GJ 569Bab and LP 349-25 AB have their masses underpredicted by the models. These systems are both of approximate spectral type M9.

For further illustration of these points, we again plot the percent difference between the masses predicted by the models and the dynamical masses, this time plotting the individual component mass. These plots are shown in Figures 10 and **??**[5]. Although the uncertainties are larger, the trend we saw amongst total system mass holds. The earliest spectral types have the strongest discrepancy with the evolutionary models. These figures also demonstrate the power of using individual component masses to perform model comparisons, allowing for the investigation of where discrepancies lie without assumptions (this is particularly apparent in the case of LHS 2397a AB, which has an M8 primary and an L7.5 secondary). In addition, individual component masses effectively double the sample of sources that can be used for comparison (here, we have compared 12 sources, already approaching the 15 we can do with total system masses). Emphasis in the future will be placed on obtaining more precise individual mass estimates for these systems to see if these trends persist.

9. Discussion

We have found systematic discrepancies between our measured dynamical masses and the predicted masses from theoretical evolutionary models, where overall the M and L dwarfs have higher dynamical masses than predicted and one T dwarf has a lower dynamical mass than predicted by evolutionary models. We determined the mass predicted by each evolutionary model using our measured parameters of luminosity and temperature, which are related to each other through the canonical equation L $=4\pi R^2\sigma T^4$. Our observed bolometric luminosity is the most constrained of

---

[5] Since only one system has a spectral type later than L5, we do not perform this exercise for the COND models

these parameters and is free of any model assumptions; therefore, it is the least likely parameter to contribute to disagreement. Instead, the radius and temperature are the most likely cause of the discrepancy between the predicted evolutionary model masses and our dynamical masses, either those predicted by the evolutionary model or those from our atmospheric model fits. In this section, we explore temperature and radius and discuss other assumptions used with both atmospheric and evolutionary models which may give rise to differences between our measured masses and predicted modeled mass. For reference, we show in Figure 10 the location of GJ 569Bb of the H-R Diagram, whose individual mass measurement was underpredicted by the evolutionary models. We show the location of the line of constant mass for a 0.05 $M_{\odot}$ source as given in both the LYON and TUCSON models, which should align with the position GJ 569Bb if there was no discrepancy. The direction of the offset between these lines and the position of GJ 56Bb is representative of the direction of the offset for all discrepant systems of M and L spectral types. Though we cannot make a corresponding plot for the case of our overpredicted T dwarf system, for which we do not have individual component masses, the direction of the offset is opposite that of GJ 569Bb.

We first consider the case in which the driver for the discrepancy is primarily the evolutionary models, which begin with mass and age as input parameters and then predict quantities of radius, temperature, and, in turn, the luminosity. For the sources in the late M through mid L spectral types that are discrepant, the mass lines that agree with our dynamical masses lie at higher temperatures and/or lower luminosities than our input values. To bring these sources into agreement would require either a decrease in the evolutionary model-predicted temperature for these sources of ~100-300 Kelvin or an increase in the radii by a factor of ~1.3-2.0. Meanwhile, for the discrepant T dwarfs, the correct mass lines lie at lower temperatures and/or higher luminosities than our input values. To bring them into agreement would require an increase in the evolutionary model predicted temperatures by ~100 Kelvin, or an increase in the radii by a factor of ~1.5.

There are a number of implications for the physics of the evolutionary models in this case. If the radii are off, this implies a that mass-radius relationship in these models might be slightly off. The predicted radius for a source is driven almost entirely by the assumed equation of state, with a very minor dependence on the assumed atmosphere (Chabrier et al. 1997). The interiors of very low mass objects are thought to be partially degenerate, and the mass radius relationship is generally modeled to follow a hybrid between the fully degenerate and classical relationships. Objects below the hydrogen burning limit will continually contract throughout their lifetimes, with a general slowing of that contraction after 1 Gyr. A need for a change in the radii for an object of a given mass could imply the need for a slight shift in the rate of contraction, or a slight shift in the radius at which the contraction effectively halts (see Figure 7 of Chabrier et al. 1997). An update of the equation of state from that given by Saumon et al. (1995), which is the equation of state used by both Burrows et al. (1997) and Chabrier et al. (2000), could potentially modify the mass-radius relationship. Indeed, more recent experiments on the behavior of dense plasmas (e.g., Collins et al. 1998) have shown that while the the Saumon et al. (1995) results agree reasonably well, there is room for improvement (Chabrier & Baraffe 2000). Incorporating the results of these new experiments may help resolve the observed discrepancies.

Meanwhile, the effective temperature is driven by the interior energy transport mechanisms for these objects, which is both convective and conductive, as well as the interior/atmospheric boundary conditions. If the required change is in the predicted effective temperature, this implies that adjustments need to be made to the efficiency of interior energy transport, or an offset is needed interior/atmospheric boundary condition. Energy transport efficiency also relates to the rate at which these objects cool over their lifetimes. An adjustment in this rate could also bring the predicted masses into agreement with our dynamical masses. Finally, magnetic activity could possibly inhibit the efficiency of convection, lowering the effective temperatures of these objects (Chabrier & Baraffe 2000). This may be important for the discrepant sources of spectral type M or L, which have lower temperatures than predicted by the evolutionary models. It has been shown that late M to mid L type objects exhibit magnetic activity (Berger 2006), and thus incorporating the effects of this activity into the models could also lead to partial resolution of the discrepancy.

The other case we consider is that in which the discrepancy is caused by the temperatures and radii predicted by the PHOENIX atmosphere models. In our spectral synthesis modeling, these two parameters are linked through the bolometric luminosity. Because our luminosity is a fixed, model-independent quantity, the parameter that matters in this case in temperature, because the radius is effectively set by the measurement of L_{Bol} and enters only as a scaling factor for the SEDs which are shaped by temperature. Therefore, if the discrepancy is caused by the atmosphere models, it is through the temperature prediction. In this case, the temperatures predicted would be too low in the case of the M and L dwarfs by ~100-300 K, and too high in the case of the T dwarf by about ~100. A change in temperature would cause the atmosphere model predicted radius to change as well, but do so in a way that again maintains correct L_{Bol}.

The PHOENIX atmosphere models we have used are thought to represent the limiting cases in terms of atmospheric dust treatment. That is, the DUSTY models assume an atmosphere fully enveloped in dust clouds, while the COND assume no dust clouds and the complete removal of refractory elements. If the temperatures predicted for the discrepant M and L dwarfs are too low, it implies that the dust clouds are too opaque, trapping too much radiation. For the T dwarfs, removal of all refractory elements from the atmosphere may have resulted in a drop in opacity that allows too much radiation to escape, causing a higher than predicted temperature. Along these lines, recent work by Helling et al. (2008) has shown that the treatment of dust clouds in atmospheric models has a dramatic effect on the output photometry. They show that the near-infrared colors predicted by different models with different dust treatments can be discrepant by as much as a magnitude. Since we have used photometry to derive our temperatures, this could imply that the dust treatment has lead to incorrect temperature predictions. Though Helling et al. (2008) only compared two test cases, one at 1800 K and one at 1000 K, a rough comparison between the colors of our discrepant sources and those test cases show that models with thinner dust clouds and uniform grain sizes may bring the temperatures into alignment with what is predicted by the evolutionary models.

We note that although we have not accounted for metallicity variation amongst our sources, using atmospheric models with fixed solar composition, our observations are not generally sensitive to metallicity. It has been shown that a factor of 10 difference in metallicity creates about a magnitude of variation in predicted photometry (Burrows et al. 2006). Since we do not expect any of our sources to have metallicities vastly different from solar, we do not have ability to distinguish metallicity with photometry, and hence not accounting for this is unlikely to have dramatically impacted our atmospheric fitting. However, our fits could potentially be slightly improved in the future by accounting for metallicity, which a number of authors have described as the potential "second parameter" that causes variations in the spectral morphology of these objects (Burrows et al. 2006).

Therefore, there are a number of scenarios in which a slight change in the input physics to either the evolutionary models or the atmosphere models (possibly both) could generate agreement between our dynamical masses and the model predicted masses. We note that discrepancies between the evolutionary and atmosphere models have been noted before for three of our systems. The systems HD 130948BC, LHS 2397a AB, and 2MASS 1534-29 AB had their relative orbits derived by Dupuy et al. (2009a), Dupuy et al. (2009b), and Liu et al. (2008). Though their approach to model comparison is different, whereby they use spectral synthesis by Cushing et al. (2008) as a proxy for performing atmospheric fitting on the sources, they find similar results to what we see here. Namely, they see that there is an offset between the evolutionary and atmosphere models, though they make the comparison only in terms of temperature (using their luminosities and total system masses with a mass ratio assumption to derive an evolutionary model predicted temperature). The temperature offsets they see in three comparisons are similar to what we derive here, though they only look at sources individually as opposed to the systematic tests across the entire substellar regime we have performed here. For the sources they compare, they find that their M and L dwarfs appear to have higher temperatures predicted by the evolutionary models than the atmosphere models and their T dwarf source has a lower temperature in the evolutionary models than the atmospheric models. Thus, though their approach is different and they only examine a few sources, they arrive at similar conclusions.

We also note that if the discrepancies between the models and the dynamical masses continue to follow the same trend, the implication for pushing into the planetary mass regime is that, like the T dwarfs, the masses of planets would be overestimated by the evolutionary models. For instance, in the case of the directly-imaged extrasolar system, HR 8799, relatively high masses of 7, 10, and 10 M_{Jup} have been derived using evolutionary models (Marois et al. 2008). These higher masses have generated some difficulty in terms of allowing for systemic stability over long timescales (Goździewski & Migaszewski 2009, Fabrycky & Murray-Clay 2008). The decrease of these masses by only a few percent would imply the system was much more stable over long timescales. Thus, this work may have important implications for the masses derived for directly imaged extrasolar planets using evolutionary models.

Future work will thus focus on improving dynamical mass estimates, with an emphasis on obtaining more individual mass measurements. With additional radial velocity measurements, individual mass measurements can approach the level of precision we have achieved for our total system masses. This will effectively double the sample of sources for which we can perform comparisons to theoretical models.

Perhaps a more powerful measurement than mass alone is the derivation of radii for these sources. Radii allow for the independent calculation of effective temperature free of an model assumption. This would allow us to test *both* the evolutionary and the atmospheric models independently of each other. Thus far, only one eclipsing binary brown dwarf has been reported (Stassun et al. 2006), providing the only empirical measurement of a brown dwarf radius (for a very young system in Orion). For our sample, we hope to measure radii through the derivation of accurate surface gravities, which provide radius estimates if the masses are known. We currently can plot the mass-radius relationship we have derived using those sources with individual mass measurements and our atmospheric-model calculated radii. We have done this in Figure 10. This figure shows that the measurement of surface gravities will allow for the measurement of radii independently from the models, allowing us to calibrate the mass-radius relationship in addition to directly calculating temperature. To measure gravities, we require high resolution spectra with gravity sensitive features. Our K band spectra, which were obtained to achieve the highest precision in radial velocity, are not suitable for this purpose as they are dominated primarily by water features, which are not gravity sensitive (Allard et al. 1997). However, alkali lines such as potassium in the J band have been shown to be quite gravity sensitive (McGovern et al. 2004, Rice et al. 2009), and can be used for this purpose. Thus, obtaining spatially resolved, high resolution J band spectra for our sources is a high priority for this project.

Additionally, one source in our sample, 2MASS 0920+35 AB (which has components in the L/T transition region), is on a highly inclined orbit with an inclination of 88.6 ± 1.2^o. Assuming that the components have a radius of 1 R_{Jup}, the system will be an eclipsing system if it has an inclination between 89.89^o and 90.15^o. Based on our full relative orbital solution distribution, we find the system has an 6.8% of eclipsing. If we consider only those solutions with a ∼6.5 year period, we find the system has a only a 3.1% chance of eclipsing. If we instead only consider those solutions with a ∼3.5 year period, the system has an 11.3% chance of eclipsing. In Figure 10, we plot the probability distribution of eclipse dates. The highest probability of eclipse occurred in April of 2009. The next most likely date of eclipse is in mid-2012. The duration of the eclipse would most likely be between 2 and 4 hours. If this system does eclipse, it will provide allow for a direct measurement of its radius, allowing for a very powerful test of models at the L/T transition region.

10. Conclusions

We have calculated relative orbital solutions for 15 very low mass binary systems, using a combination of astrometric and radial velocity data obtained with the Keck Observatory LGS AO system. For 10 of these systems, this is the first derivation of the relative orbits. We have also calculated the absolute orbital solutions for 6 systems, 5 of which are the first for those systems. Further, we have performed spectral synthesis modeling 12 of these systems using their spatially resolved photometry and the PHOENIX atmosphere models. This provides as estimate of the temperatures of each source.

The masses we have calculated based on these orbital solutions and our derived temperatures have allowed us to perform the first comprehensive comparison of a sample of VLM objects to theoretical evolutionary models. We find that for 6 systems, their total system masses are underpredicted by both evolutionary models considered. In these systems, 11 of the 12 components have spectral types earlier than L4. We find that one binary T dwarf has its total system mass overpredicted by the evolutionary models. The additional 8 systems, which include all 3 L/T transition systems in our sample, have evolutionary model predictions consistent with the dynamical masses. We postulate that for those systems in which we see a discrepancy, the possible cause is either an incorrect radius prediction by the evolutionary models, an incorrect temperature prediction by the evolutionary models, or an incorrect temperature prediction by the atmospheric models.

Future work will focus on improving the precision of our dynamical masses, with a particular emphasis on obtaining more individual masses across a broader range of spectral types. We will also obtain radius measurements for our sources, primarily through the calculation of surface gravity, which will allow us to test the evolutionary and atmospheric models independently. These measurements will provide powerful new tests of the evolutionary models.

The authors thank observing assistants **Steven Magee, Madeline Reed, and Terry Stickel** and support astronomers Randy Campbell, Al Conrad, Jim Lyke, and Hien Tran for their help in obtaining the observations. Support for this work was provided by the NASA Astrobiology Institute, the Packard Foundation, and the NSF Science & Technology Center for AO, managed by UCSC (AST-9876783). QMK acknowledges support from the NASA Graduate Student Research Program (NNG05-GM05H) through JPL and the UCLA Dissertation Year Fellowship Program. This publication makes use of data products from the Two Micron All Sky Survey, which is a joint project of the University of Massachusetts and the Infrared Processing and Analysis Center/California Institute of Technology, funded by the National Aeronautics and Space Administration and the National Science Foundation. The W.M. Keck Observatory is operated as a scientific partnership among the California Institute of Technology, the University of California and the National Aeronautics and Space Administration. The Observatory was made possible by the generous financial support of the W.M. Keck Foundation. The authors also wish to recognize and acknowledge the very significant cultural role and reverence that the summit of Mauna Kea has always had within the indigenous Hawaiian community. We are most fortunate to have the opportunity to conduct observations from this mountain.

REFERENCES

Allard, F., Hauschildt, P. H., Alexander, D. R., & Starrfield, S. 1997, ARA&A, 35, 137

Ambartsumian, V. A. 1937, Astron. Zh., 14, 207

Basri, G., & Martín, E. L. 1999, AJ, 118, 2460

Blake, C. H., Charbonneau, D., White, R. J., Marley, M. S., & Saumon, D. 2007, ApJ, 666, 1198

Bouy, H., Brandner, W., Martín, E. L., Delfosse, X., Allard, F., & Basri, G. 2003, AJ, 126, 1526

Bouy, H., et al. 2004, A&A, 423, 341

Bouy, H., et al. 2008, A&A, 481, 757

Burgasser, A. J., Kirkpatrick, J. D., Reid, I. N., Brown, M. E., Miskey, C. L., & Gizis, J. E. 2003, ApJ, 586, 512

Burgasser, A. J., Kirkpatrick, J. D., Cruz, K. L., Reid, I. N., Leggett, S. K., Liebert, J., Burrows, A., & Brown, M. E. 2006, ApJS, 166, 585

Burgasser, A. J., Reid, I. N., Siegler, N., Close, L., Allen, P., Lowrance, P., & Gizis, J. 2007, Protostars and Planets V, 427

Burrows, A., et al. 1997, ApJ, 491, 856

Burrows, A., Sudarsky, D., & Hubeny, I. 2006, ApJ, 640, 1063

Chabrier, G., & Baraffe, I. 1997, A&A, 327, 1039

Chabrier, G., & Baraffe, I. 2000, ARA&A, 38, 337

Chabrier, G., Baraffe, I., Allard, F., & Hauschildt, P. 2000, ApJ, 542, 464

Close, L. M., Siegler, N., Freed, M., & Biller, B. 2003, ApJ, 587, 407

Close, L. M., Siegler, N., Potter, D., Brandner, W., & Liebert, J. 2002, ApJ, 567, L53

Collins, G. W., et al. 1998, Science, 281, 1178

Cruz, K. L., Reid, I. N., Liebert, J., Kirkpatrick, J. D., & Lowrance, P. J. 2003, AJ, 126, 2421

Cutri, R. M., et al. 2003, The IRSA 2MASS All-Sky Point Source Catalog, NASA/IPAC Infrared Science Archive. http://irsa.ipac.caltech.edu/applications/Gator/

Cushing, M. C., et al. 2008, ApJ, 678, 1372

Dahn, C. C., et al. 2002, AJ, 124, 1170

Diolaiti, E., Bendinelli, O., Bonaccini, D., Close, L. M., Currie, D. G., & Parmeggiani, G. 2000, Proc. SPIE, 4007, 879

Duchêne, G., Beust, H., Adjali, F., Konopacky, Q. M., & Ghez, A. M. 2006, A&A, 457, L9

Duchêne, G., Ghez, A. M., McCabe, C., & Weinberger, A. J. 2003, ApJ, 592, 288

Dupuy, T. J., Liu, M. C., & Ireland, M. J. 2009, ApJ, 692, 729

Dupuy, T. J., Liu, M. C., & Ireland, M. J. 2009, ApJ, 699, 168

Duquennoy, A., & Mayor, M. 1991, A&A, 248, 485

Fabrycky, D. C. & Murray-Clay, R. A. 2008, arXiv:0812.0011v1 [astro-ph]

Figer, D. F., et al. 2003, ApJ, 599, 1139

Forveille, T., et al. 2005, A&A, 435, L5

Freed, M., Close, L. M., & Siegler, N. 2003, ApJ, 584, 453

Ghez, A. M., et al. 2008, ApJ, 689, 1044

Gizis, J. E., Reid, I. N., Knapp, G. R., Liebert, J., Kirkpatrick, J. D., Koerner, D. W., & Burgasser, A. J. 2003, AJ, 125, 3302

Golimowski, D. A., et al. 2004, AJ, 127, 3516

Goździewski, K., & Migaszewski, C. 2009, MNRAS, 397, L16

Hauschildt, P. H., Allard, F., & Baron, E. 1999, ApJ, 512, 377

Helling, C., et al. 2008, MNRAS, 391, 1854

Hilditch, R. W. 2001, An Introduction to Close Binary Stars (Cambridge: Cambridge University Press)

Hillenbrand, L. A., & White, R. J. 2004, ApJ, 604, 741

Kirkpatrick, J. D. 2005, ARA&A, 43, 195

Konopacky, Q. M., Ghez, A. M., Duchêne, G., McCabe, C., & Macintosh, B. A. 2007a, AJ, 133, 2008

Lane, B. F., Zapatero Osorio, M. R., Britton, M. C., Martín, E. L., & Kulkarni, S. R. 2001, ApJ, 560, 390

Leggett, S. K., et al. 2002, ApJ, 564, 452

Liu, M. C., Dupuy, T. J., & Ireland, M. J. 2008, ApJ, 689, 436

Luhman, K. L., Stauffer, J. R., Muench, A. A., Rieke, G. H., Lada, E. A., Bouvier, J., & Lada, C. J. 2003, ApJ, 593, 1093

Marois, C., Macintosh, B., Barman, T., Zuckerman, B., Song, I., Patience, J., Lafrenière, D., & Doyon, R. 2008, Science, 322, 1348

Martín, E. L., Koresko, C. D., Kulkarni, S. R., Lane, B. F., & Wizinowich, P. L. 2000, ApJ, 529, L37

McGovern, M. R., Kirkpatrick, J. D., McLean, I. S., Burgasser, A. J., Prato, L., & Lowrance, P. J. 2004, ApJ, 600, 1020

McLean, I. S., Graham, J. R., Becklin, E. E., Figer, D. F., Larkin, J. E., Levenson, N. A., & Teplitz, H. I. 2000, Proc. SPIE, 4008, 1048

Potter, D., Martín, E. L., Cushing, M. C., Baudoz, P., Brandner, W., Guyon, O., & Neuhäuser, R. 2002, ApJ, 567, L133

Reid, I. N., Gizis, J. E., Kirkpatrick, J. D., & Koerner, D. W. 2001, AJ, 121, 489

Reid, I. N., Lewitus, E., Allen, P. R., Cruz, K. L., & Burgasser, A. J. 2006, AJ, 132, 891

Rice, E. L., Barman, T. S., McLean, I. S., Prato, L., & Kirkpatrick, J.D. 2009, ApJ, submitted

Saumon, D., Chabrier, G., & van Horn, H. M. 1995, ApJS, 99, 713

Siegler, N., Close, L. M., Cruz, K. L., Martín, E. L., & Reid, I. N. 2005, ApJ, 621, 1023

Siegler, N., Close, L. M., Mamajek, E. E., & Freed, M. 2003, ApJ, 598, 1265

Simon, M., Bender, C., & Prato, L. 2006, ApJ, 644, 1183

Stassun, K. G., Mathieu, R. D., & Valenti, J. A. 2006, Nature, 440, 311

Tamazian, V. S., Docobo, J. A., White, R. J., & Woitas, J. 2002, ApJ, 578, 925

van Dam, M. A., et al. 2006, PASP, 118, 310

Vrba, F. J., et al. 2004, AJ, 127, 2948

White, R. J., et al. 2009, in prep

Wizinowich, P. L., et al. 2006, PASP, 118, 297

Yelda, S., Lu, J. R., Ghez, A. M., Clarkson, W., & Anderson, J. 2009, in prep

---

This preprint was prepared with the AAS LaTeX macros v5.2.

Table 1. Initial VLM Binary Sample

Source Name	RA (J2000)	Dec (J2000)	Estimated Sp Types	Discovery Reference	2MASS K Band Mag.
LP 349-25AB	00 27 55.93	+22 19 32.8	M8+M9	13	9.569 ± 0.017
LP 415-20AB	04 21 49.0	+19 29 10	M7+M9.5	8	11.668 ± 0.020
2MASS J04234857-0414035AB[a]	04 23 48.57	-04 14 03.5	L7+T2	1	12.929 ± 0.034
2MASS J05185995-2828372AB[a]	05 18 59.95	-28 28 37.2	L6+T4	2	14.162 ± 0.072
2MASS J06523073+4710348AB[a]	06 52 30.7	+47 10 34	L3.5+L6.5	3	11.694 ± 0.020
2MASS J07464256+2000321AB	07 46 42.5	+20 00 32	L0+L1.5	4	10.468 ± 0.022
2MASS J09201223+3517429AB	09 20 12.2	+35 17 42	L6.5+T2	4	13.979 ± 0.061
2MASS J10170754+1308398AB[b]	10 17 07.5	+13 08 39.1	L2+L2	5	12.710 ± 0.023
2MASS J10471265+4026437AB	10 47 12.65	+40 26 43.7	M8+L0	6	10.399 ± 0.018
GJ 417BC[a]	11 12 25.67	+35 48 13.2	L4.5+L6	5	12.721 ± 0.028
GJ 569b AB	14 54 29.0	+16 06 05	M8.5+M9	14	~9.8
LHS 2397a AB	11 21 49.25	-13 13 08.4	M8+L7.5	12	10.735 ± 0.023
2MASS J121711-031113AB	12 17 11.0	-03 11 13	T7.5+Y?	7	~15.887[c]
2MASS J14263161+1557012AB	14 26 31.62	+15 57 01.3	M8.5+L1	6	11.731 ± 0.018
HD 130948 BC	14 50 15.81	+23 54 42.6	L4+L4	10	~11.0
2MASS J15344984-2952274AB	15 34 49.8	-29 52 27	T5.5+T5.5	7	14.843 ± 0.114
2MASS J1600054+170832AB[a]	16 00 05.4	+17 08 32	L1+L3	5	14.678 ± 0.114
2MASS J17281150+3948593AB	17 28 11.50	+39 48 59.3	L7+L8	5	13.909 ± 0.048
2MASS J17501291+4424043AB	17 50 12.91	+44 24 04.3	M7.5+l0	8	11.768 ± 0.017
2MASS J18470342+5522433AB	18 47 03.42	+55 22 43.3	M7+M7.5	9	10.901 ± 0.020
2MASS J21402931+1625183AB	21 40 29.32	+16 25 18.3	M8.5+L2	6	11.826 ± 0.031
2MASS J22062280-2047058AB	22 06 22.80	-20 47 05.9	M8+M8	6	11.315 ± 0.027

[a] In all observations of these sources, the binary was never resolved. We report upper limits to the separations of these binaries, but no orbital solutions can be derived

[b] Source cut from sample due to additional astrometry showing that it was not likely to yield a mass to a precision of better than 10% in the required timeframe

[c] Flagged as having poor photometric quality in 2MASS catalog

Note. — References - (1) Burgasser et al. 2005 (2) Cruz et al. 2004 (3) Reid et al. (4) Reid et al. 2001 (5) Bouy et al. 2003 (6) Close et al. 2003 (7) Burgasser et al. 2003 (8) Siegler et al. 2003 (9) Siegler et al. 2005 (10) Potter et al. (2002) (11) Koerner et al. 1999 (12) Freed et al. 2003 (13) Forveille et al. 2005 (14) Martin et al. 2000

Table 2. Additional VLM Binary Sources

Source Name	RA (J2000)	Dec (J2000)	Estimated Sp Types	Discovery Reference	2MASS K Band Mag.
2MASS J07003664+3157266	07 00 36.64	+31 57 26.60	L3.5+L6	1	11.317 ± 0.023
2MASS J08503593+1057156	08 50 35.9	+10 57 16	L6+L8	3	14.473 ± 0.066
2MASS J10210969-0304197	10 21 09.69	-03 04 20.10	T1+T5	2	15.126 ± 0.173
2MASS J21011544+1756586	21 01 15.4	+17 56 58	L7+L8	4	14.892 ± 0.116
2MASS J21522609+0937575	21 52 26	+09 37 57	L6+L6	1	13.343 ± 0.034

Note. — References - (1) Reid et al. 2006 (2) Burgasser et al. 2006 (3) Reid et al. 2001 (4) Bouy et al. 2003

Table 3. Log of NIRC2 LGS AO Observations

Target Name	Date of Observation (UT)	Tip/Tilt Reference	Filter	Exposure Time (sec x coadds)	No. of Frames
2MASS 0518-28AB	2006 Nov 27	USNO-B1.0 0615-0055823	K-prime	30x4	18
	2007 Dec 02		K-prime	30x4	9
	2008 Dec 18		K-prime	20x4	5
2MASS 0652+47AB	2006 Nov 27	USNO-B1.0 1371-0206444	K-prime	8x12	6
	2007 Dec 02		K-prime	5x12	9
2MASS 0746+20AB	2006 Nov 27	source	K-prime	2x30	9
	2007 Dec 01		K-prime	2x30	8
	2007 Dec 01		J	4x15	9
	2008 Dec 18		K-prime	2x30	8
	2008 Dec 18		H	2x30	6
2MASS 0850+10AB	2007 Dec 02	USNO-B1.0 1009-0165240	K-prime	30x4	9
	2008 Dec 18		K-prime	10x1	5
2MASS 0920+35AB	2006 Nov 27	USNO-B1.0 1252-0171182	K-prime	30x4	7
	2007 Dec 02		K-prime	30x4	4
	2007 Dec 02		J	30x4	2
	2008 May 30		K-prime	30x4	6
	2008 Oct 21		H	30x4	6
	2008 Dec 18		H	10x10	7
	2009 Jun 10		H	10x5	6
2MASS 1017+13AB	2006 Nov 27	USNO-B1.0 1031-0208442	K-prime	13x12	3
2MASS 1047+40AB	2006 Jun 21	source	K-prime	1x60	9
	2006 Nov 27		K-prime	2x30	12
	2007 Dec 02		K-prime	2x30	6
	2008 Dec 18		K-prime	1x30	9
2MASS 1426+15AB	2006 Jun 20	USNO B1.0-1059-0232527	K-prime	10x12	3
	2008 May 30		K-prime	10x12	8
	2008 May 30		J	15x5	5
	2009 May 02		K-prime	5x12	9
	2009 May 02		H	5x12	6
2MASS 1534-29AB	2006 Jun 20	USNO-B1.0 0601-0344997	J	30x4	9
	2008 May 30		K-prime	40x2	7
	2008 May 30		H	40x2	6
	2008 May 30		J	40x1	3
	2009 May 04		H	30x4	6
2MASS 1600+17AB	2007 May 20	USNO-B1.0 1071-0293881	K-prime	30x4	9
	2008 May 30		K-prime	10x1	2
2MASS 1728+39AB	2007 May 20	USNO-A2.0 1275-09377115	K-prime	30x4	5
	2008 May 30		K-prime	30x2	4
	2008 May 30		J	60x2	5
	2009 May 03		K-prime	30x2	7
	2009 Jun 11		H	30x4	9
2MASS 1750+44AB	2006 Jun 20	source	K-prime	20x4	8
	2007 May 17		K-prime	10x12	7
	2008 May 13		K-prime	10x12	6
	2008 May 30		H	5x12	6

Table 3—Continued

Target Name	Date of Observation (UT)	Tip/Tilt Reference	Filter	Exposure Time (sec x coadds)	No. of Frames
	2008 May 30		J	10x1	4
	2009 May 01		K-prime	5x12	9
2MASS 1847+55AB	2006 May 21	source	K-prime	5x6	6
	2007 May 14		K-prime	1.452x1	9
	2008 May 20		K-prime	5x12	9
	2008 May 20		H	5x5	6
	2008 May 20		J	10x1	19
	2009 May 04		K-prime	5x12	9
2MASS 2140+16AB	2006 May 21	USNO-B1.0 1064-0594380	K-prime	5x1	12
	2006 Nov 27		K-prime	10x12	9
	2007 May 14		K-prime	7x5	9
	2007 Dec 02		K-prime	10x12	9
	2008 May 15		K-prime	10x12	9
	2008 May 30		H	5x12	4
	2008 May 30		J	10x1	4
	2008 Dec 19		K-prime	5x12	9
	2009 Jun 11		K-prime	5x12	8
2MASS 2206-20AB	2006 May 21	source	K-prime	5x6	9
	2006 Nov 27		K-prime	10x12	9
	2007 May 17		K-prime	10x3	8
	2007 Dec 02		K-prime	10x12	2
	2008 May 30		K-prime	5x12	9
	2008 May 30		H	5x6	3
	2008 May 30		J	10x1	6
	2009 Jun 11		K-prime	2.5x12	9
GJ 417BC	2007 Dec 02	USNO-B1.0 1258-0189170	K-prime	30x2	5
GJ 569BC	2009 Jun 11	GJ569A	K-prime	0.5x30	10
HD 130948BC	2007 May 11	HD 130948A	K-prime	2x30	12
	2007 May 11		H	2x60	12
	2007 May 11		J	4x15	12
	2007 May 11		L-prime	0.181x60	17
	2007 May 11		M-short	0.181x60	24
	2008 Apr 28		K-prime	0.1452x1	12
	2009 May 09		H	1x15	7
LHS 2397aAB	2006 Nov 27	source	K-prime	15x10	3
	2007 Dec 02		K-prime	8x15	3
	2007 Dec 02		J	10x15	6
	2008 May 30		K-prime	3x30	8
	2008 Dec 18		K-prime	2x30	8
	2008 Dec 18		H	1.5x30	6
	2008 Dec 18		J	2x30	6
	2009 Jun 10		K-prime	2x30	9
LP 349-25AB	2006 Nov 27	source	K-prime	1x30	5
	2006 Nov 27		H	1x30	5
	2006 Nov 27		J	1.5x30	3

Table 3—Continued

Target Name	Date of Observation (UT)	Tip/Tilt Reference	Filter	Exposure Time (sec x coadds)	No. of Frames
	2007 Dec 02		K-prime	5x6	9
	2008 May 30		K-prime	1.452x20	7
	2008 Dec 19		K-prime	2x20	6
	2008 Dec 19		J	1.5x20	5
	2009 Jun 11		K-prime	0.5x20	12
LP 415-20AB	2006 Nov 27	source	K-prime	8x12	6
	2007 Dec 02		K-prime	6x12	9
	2008 Dec 18		K-prime	6x12	9
	2008 Dec 18		H	5x12	9

Table 4. Log of NIRSPAO-LGS K-band Observations

Target Name	Date of Observation (UT)	A0V Star Standard	Exposure Time (sec x coadds)	No. of Frames
2MASS J07464256+2000321AB	2006 Dec 16	HIP 41798	1200x1	4
	2007 Dec 04	HIP 41798	1200x1	6
	2008 Dec 19	HIP 41798	1200x1	6
2MASS J14263161+1557012AB	2007 Jun 08	HIP 73087	1200x1	4
	2008 Jun 01	HIP 73087	1200x1	4
	2009 Jun 12	HIP 73087	1200x1	4
2MASS J17501291+4424043AB	2008 May 31	HIP 87045	1200x1	4
	2009 Jun 12	HIP 87045	1200x1	6
2MASS J18470342+5522433AB	2007 Jun 08	HIP 93713	1200x1	4
	2008 Jun 01	HIP 93713	1200x1	5
	2009 Jun 13	HIP 93713	1200x1	3
2MASS J21402931+1625183AB	2007 Jun 09	HIP 108060	1200x1	4
	2008 May 31	HIP 108060	1800x1	3
	2009 Jun 13	HIP 108060	1800x1	2
2MASS J22062280-2047058AB	2007 Jun 09	HIP 116750	1200x1	3
	2008 Jun 01	HIP 109689	1200x1	4
	2009 Jun 12	HIP 109689	1200x1	4
GJ 569b AB	2007 Jun 09	HIP 73087	900x1	2
	2009 Jun 13	HIP 73087	900x1	4
HD 130948BC	2007 Jun 09	HIP 73087	1200x1	4
LHS 2397aAB	2007 Dec 04	HIP 58188	1800x1	2
	2008 May 31	HIP 61318	1800x1	3
	2008 Dec 19	HIP 58188	1800x1	3
	2009 Jun 12	HIP 61318	1800x1	2
LP 349-25AB	2006 Dec 16	HIP 5132	600x1	4
	2007 Dec 04	HIP 5132	900x1	1
	2008 Dec 19	HIP 5132	1200x1	4
	2009 Jun 12	HIP 5132	1200x1	4
LP 415-20AB	2008 Dec 19	HIP 24555	1200x1	4

Table 5. NIRC2 LGS AO Results

Target Name	Date of Observation (UT)	Filter	Separation (pixels)[a]	Separation (arcseconds)[b]	Position Angle (degrees)[c]	Flux Ratio (Ab/Aa)[d]
2MASS 0518-28	2006 Nov 27	K-prime	< 6.40	< 0.064	—	—
	2007 Dec 02	K-prime	< 5.55	< 0.055	—	—
	2008 Dec 18	K-prime	< 6.55	< 0.065	—	—
2MASS 0652+47	2006 Nov 27	K-prime	< 3.05	< 0.030	—	—
	2007 Dec 02	K-prime	< 3.73	< 0.037	—	—
2MASS 0746+20	2006 Nov 27	K-prime	29.924 ± (0.058 ± 0.013)	0.2981 ± 0.0006	233.93 ± (0.08 ± 0.03) [0.08]	1.39 ± (0.02 ± 0.04)
	2007 Nov 30	K-prime	33.533 ± (0.028 ± 0.057)	0.3341 ± 0.0007	223.54 ± (0.04 ± 0.22) [0.23]	1.39 ± (0.01 ± 0.03)
	2007 Nov 30	J	33.501 ± (0.165 ± 0.072)	0.334 ± 0.002	223.49 ± (0.36 ± 0.26) [0.45]	1.60 ± (0.14 ± 0.04)
	2008 Dec 18	K-prime	35.240 ± (0.032 ± 0.002)	0.3511 ± 0.0004	214.31 ± (0.06 ± 0.02) [0.07]	1.39 ± (0.01 ± 0.03)
	2008 Dec 18	H	35.268 ± (0.036 ± 0.039)	0.3514 ± 0.0006	214.38 ± (0.10 ± 0.07) [0.13]	1.50 ± (0.01 ± 0.04)
2MASS 0850+10	2007 Dec 01	K-prime	8.927 ± (0.197 ± 0.215)	0.089 ± 0.003	158.71 ± (0.93 ± 0.13) [0.93]	1.81 ± (0.19 ± 0.04)
	2008 Dec 18	K-prime	7.611 ± (0.086 ± 0.073)	0.076 ± 0.001	165.87 ± (0.36 ± 0.12) [0.37]	2.12 ± (0.10 ± 0.03)
2MASS 0920+35	2006 Nov 27	K-prime	6.583 ± (0.194 ± 0.406)	0.066 ± 0.004	247.14 ± (2.04 ± 0.06) [2.04]	1.36 ± (0.08 ± 0.04)
	2007 Dec 01	K-prime	7.561 ± (0.292 ± 0.232)	0.075 ± 0.004	244.91 ± (3.23 ± 0.27) [3.24]	1.19 ± (0.07 ± 0.04)
	2007 Dec 01	J	6.623 ± (1.50 ± 0.66)	0.066 ± 0.016	247.7 ± (1.6 ± 0.2) [1.6]	1.04 ± (0.27 ± 0.05)
	2008 May 30	K-prime	6.622 ± (0.079 ± 0.057)	0.066 ± 0.001	249.94 ± (0.53 ± 0.09) [0.54]	1.75 ± (0.09 ± 0.03)
	2008 Oct 20	H	4.714 ± 0.145	0.047 ± 0.001	252.3 ± 3.0	1.20 ± 0.07
	2008 Dec 18	H	3.753 ± 0.335	0.037 ± 0.003	247.6 ± 1.8	1.07 ± 0.05
	2009 Jun 10	H	< 2.63	< 0.0262	—	—
2MASS 1017+13	2006 Nov 27	K-prime	8.777 ± (2.403 ± 0.295)	0.087 ± 0.024	83.11 ± (4.98 ± 0.06) [4.98]	1.27 ± (0.63 ± 0.04)
2MASS 1047+40	2006 Jun 21	K-prime	3.178 ± (0.169 ± 0.153)	0.032 ± 0.002	126.77 ± (4.44 ± 0.05) [4.44]	1.52 ± (0.26 ± 0.02)
	2006 Nov 27	K-prime	< 4.68	< 0.047	—	—
	2007 Dec 02	K-prime	< 4.68	< 0.047	—	—
2MASS 1426+15	2006 Jun 19	K-prime	26.565 ± (0.054 ± 0.018)	0.265 ± 0.001	343.07 ± (0.47 ± 0.04) [0.47]	1.81 ± (0.10 ± 0.02)
	2008 May 30	K-prime	30.562 ± (0.043 ± 0.015)	0.3045 ± 0.0005	343.55 ± (0.06 ± 0.03) [0.07]	1.82 ± (0.02 ± 0.03)
	2008 May 30	H	30.479 ± (0.107 ± 0.071)	0.304 ± 0.001	343.53 ± (0.28 ± 0.22) [0.36]	2.02 ± (0.05 ± 0.02)
	2009 May 02	K-prime	32.389 ± (0.046 ± 0.015)	0.3227 ± 0.0005	343.69 ± (0.06 ± 0.05) [0.08]	1.84 ± (0.02 ± 0.04)
	2009 May 02	H	32.375 ± (0.038 ± 0.017)	0.3226 ± 0.0006	343.84 ± (0.06 ± 0.05) [0.08]	1.91 ± (0.02 ± 0.04)
2MASS 1534-29	2006 Jun 19	J	18.649 ± 0.125	0.186 ± 0.001	15.57 ± 0.29	1.20 ± 0.04
	2008 May 30	K-prime	9.571 ± 0.121	0.095 ± 0.001	21.53 ± 0.84	1.23 ± 0.13
	2008 May 30	H	9.549 ± 0.131	0.095 ± 0.001	21.69 ± 0.82	1.38 ± 0.09
	2009 May 04	H	3.919 ± 0.118	0.039 ± 0.001	38.52 ± 3.25	1.28 ± 0.11
2MASS 1600+17	2007 May 20	K-prime	< 4.02	< 0.040	—	—
	2008 May 30	K-prime	< 3.90	< 0.039	—	—

Table 5—Continued

Target Name	Date of Observation (UT)	Filter	Separation (pixels)[a]	Separation (arcseconds)[b]	Position Angle (degrees)[c]	Flux Ratio (Ab/Aa)[d]
2MASS 1728+39	2007 May 20	K-prime	20.496 ± (0.138 ± 0.030)	0.204 ± 0.001	85.08 ± (0.21 ± 0.14) [0.25]	1.83 ± (0.03 ± 0.02)
	2008 May 30	K-prime	20.790 ± (0.589 ± 0.026)	0.207 ± 0.006	101.33 ± (0.13 ± 0.03) [0.14]	1.97 ± (0.14 ± 0.03)
	2008 May 30	J	21.467 ± (0.045 ± 0.165)	0.214 ± 0.002	101.85 ± (0.12 ± 0.25) [0.28]	1.34 ± (0.02 ± 0.02)
	2009 May 03	K-prime	21.854 ± (0.019 ± 0.110)	0.218 ± 0.001	105.85 ± (0.48 ± 0.15) [0.50]	1.74 ± (0.02 ± 0.02)
	2009 Jun 11	H	21.868 ± 0.034	0.218 ± 0.0004	106.41 ± 0.08	1.52 ± 0.01
2MASS 1750+44	2006 Jun 19	K-prime	15.392 ± (0.443 ± 0.050)	0.153 ± 0.004	33.68 ± (2.47 ± 0.07) [2.47]	1.94 ± (0.13 ± 0.02)
	2007 May 17	K-prime	17.330 ± (0.161 ± 0.022)	0.173 ± 0.002	42.37 ± (0.28 ± 0.02) [0.28]	1.93 ± (0.02 ± 0.04)
	2008 May 13	K-prime	18.556 ± (0.020 ± 0.057)	0.1849 ± 0.0006	52.29 ± (0.05 ± 0.06) [0.08]	1.84 ± (0.02 ± 0.03)
	2008 May 30	J	19.321 ± (0.173 ± 0.201)	0.192 ± 0.003	53.78 ± (0.32 ± 0.16) [0.35]	2.41 ± (0.03 ± 0.02)
	2008 May 30	H	18.575 ± (0.115 ± 0.394)	0.185 ± 0.004	52.64 ± (0.91 ± 1.77) [1.99]	2.04 ± (0.11 ± 0.19)
	2009 May 01	K-prime	20.2779 ± (0.035 ± 0.011)	0.2020 ± 0.0004	60.31 ± (0.06 ±0.02) [0.07]	1.83 ± (0.01 ± 0.02)
2MASS 1847+55	2006 May 21	K-prime	15.289 ± (0.032 ± 0.076)	0.1523 ± 0.0008	110.90 ± (0.03 ± 0.01) [0.04]	1.30 ± (0.003 ± 0.02)
	2007 May 14	K-prime	17.335 ± (0.039 ± 0.059)	0.173 ± 0.007	114.01 ± (0.08 ± 0.04) [0.09]	1.28 ± (0.01 ± 0.02)
	2008 May 20	K-prime	19.202 ± (0.147 ± 0.052)	0.191 ± 0.002	116.71 ± (0.44 ± 0.04) [0.44]	1.28 ± (0.04 ± 0.02)
	2008 May 20	J	18.892 ± (0.133 ± 0.209)	0.188 ± 0.003	116.61 ± (0.28 ± 0.15) [0.32]	1.25 ± (0.01 ± 0.10)
	2008 May 20	H	19.245 ± (0.054 ± 0.389)	0.192 ± 0.004	116.64 ± (0.15 ± 2.71) [2.72]	1.30 ± (0.03 ± 0.19)
	2009 May 04	K-prime	20.726 ± (0.057 ± 0.008)	0.2065 ± 0.0006	118.74 ± (0.13 ± 0.01) [0.14]	1.28 ± (0.02 ± 0.03)
2MASS 2140+16	2006 May 21	K-prime	10.922 ± 0.061	0.1088 ± 0.0006	202.91 ± 0.54 ± 0	1.97 ± 0.04
	2006 Nov 27	K-prime	10.803 ± 0.126	0.108 ± 0.001	215.02 ± 1.16	1.94 ± 0.12
	2007 May 14	K-prime	10.816 ± 0.044	0.1078 ± 0.0004	223.50 ± 0.25	1.96 ± 0.05
	2007 Dec 01	K-prime	10.879 ± 0.209	0.108 ± 0.002	234.02 ± 0.66	1.95 ± 0.12
	2008 May 15	K-prime	11.067 ± 0.096	0.111 ± 0.001	243.28 ± 0.56	1.96 ± 0.07
	2008 May 30	J	12.021 ± 0.173	0.120 ± 0.002	241.41 ± 0.45	2.39 ± 0.34
	2008 May 30	H	11.491 ± 0.075	0.115 ± 0.001	242.9 ± 1.6	2.35 ± 0.38
	2008 Dec 19	K-prime	11.311 ± 0.390	0.113 ± 0.004	254.68 ± 0.32	1.94 ± 0.19
	2009 Jun 11	K-prime	11.478 ± 0.113	0.114 ± 0.001	263.34 ± 0.23	1.93 ± 0.09
2MASS 2206-20	2006 May 21	K-prime	13.068 ± (0.147 ± 0.133)	0.130 ± 0.002	128.99 ± (0.27 ± 0.13) [0.27]	1.04 ± (0.05 ± 0.02)
	2006 Nov 27	K-prime	12.747 ± (0.223 ± 0.165)	0.127 ± 0.003	138.65 ± (0.29 ± 0.04) [0.30]	1.06 ± (0.09 ± 0.04)
	2007 May 17	K-prime	12.313 ± (0.013 ± 0.035)	0.1227 ± 0.0004	147.68 ± (0.12 ± 0.02) [0.12]	1.03 ± (0.01 ± 0.04)
	2007 Dec 01	K-prime	12.199 ± (0.07 ± 0.18)	0.122 ± 0.002	160.40 ± (0.09 ± 0.27) [0.29]	0.97 ± (0.09 ± 0.04)
	2008 May 30	K-prime	12.394 ± (0.084 ± 0.042)	0.1235 ± 0.0009	169.58 ± (0.34 ± 0.04) [0.34]	1.11 ± (0.11 ± 0.03)
	2008 May 30	J	11.834 ± (0.104 ± 0.404)	0.118 ± 0.004	170.49 ± (0.35 ± 0.47) [0.59]	1.15 ± (0.03 ± 0.02)
	2008 May 30	H	11.543 ± (0.838 ± 0.453)	0.115 ± 0.009	169.82 ± (0.92 ± 0.35) [0.99]	1.04 ± (0.18 ± 0.19)
	2009 Jun 11	K-prime	12.588 ± (0.033 ± 0.123)	0.124 ± 0.001	190.52 ± (0.07 ± 0.03) [0.09]	1.05 ± 0.02

Table 5—Continued

Target Name	Date of Observation (UT)	Filter	Separation (pixels)[a]	Separation (arcseconds)[b]	Position Angle (degrees)[c]	Flux Ratio (Ab/Aa)[d]
HD 130948 BC	2006 Jun 18[e]	Hn3	5.401 ± 0.279	0.109 ± 0.006	136.33 ± 3.68	—
	2007 May 11	K-prime	10.620 ± (0.058 ± 0.101)	0.1058 ± 0.001	131.63 ± (0.11 ± 0.03) [0.12]	1.21 ± (0.12 ± 0.03)
	2008 Apr 28	K-prime	5.068 ± (0.069 ± 0.122)	0.0505 ± 0.001	122.82 ± (4.93 ± 0.05) [4.93]	1.15 ± (0.31 ± 0.04)
	2009 May 09	H	3.775 ± (0.318 ± 0.528)	0.038 ± 0.006	327.1 ± (5.0 ± 1.1) [5.1]	1.20 ± (0.13 ± 0.15)
LHS 2397a	2006 Nov 27	K-prime	9.672 ± (4.976 ± 0.259)	0.096 ± 0.050	300.01 ± (9.38 ± 0.38) [9.39]	1.77 ± (0.82 ± 0.04)
	2007 Dec 01	K-prime	14.629 ± (0.554 ± 0.155)	0.146 ± 0.006	19.95 ± (2.16 ± 0.13) [2.17]	10.16 ± (0.86 ± 0.04)
	2008 May 30	K-prime	15.983 ± (0.758 ± 0.034)	0.159 ± 0.008	37.77 ± (1.68 ± 0.26) [1.70]	12.21 ± (1.49 ± 0.03)
	2008 Dec 18	K-prime	19.813 ± (0.101 ± 0.013)	0.197 ± 0.001	50.27 ± (0.11 ± 0.04) [0.12]	13.2 ± (1.0 ± 0.03)
	2008 Dec 18	H	19.908 ± (0.276 ± 0.055)	0.196 ± 0.003	50.94 ± (0.37 ± 0.11) [0.39]	17.4 ± (1.2 ± 0.04)
	2009 Jun 10	K-prime	22.026 ± (0.035 ± 0.021)	0.2195 ± 0.0004	59.44 ± (0.08 ± 0.58) [0.59]	12.89 ± (0.39 ± 0.02)
LP 349-25	2006 Nov 27	K-prime	12.603 ± (0.049 ± 0.169)	0.126 ± 0.002	234.88 ± (0.17 ± 0.70) [0.72]	1.38 ± (0.02 ± 0.04)
	2006 Nov 27	J	12.439 ± (0.213 ± 0.129)	0.124 ± 0.002	236.67 ± (2.53 ± 0.06) [1.53]	1.64 ± (0.04 ± 0.04)
	2006 Nov 27	H	12.349 ± (0.093 ± 0.150)	0.123 ± 0.002	235.48 ± (0.46 ± 0.06) [0.47]	1.48 ± (0.08 ± 0.04)
	2007 Dec 01	K-prime	13.126 ± (0.400 ± 0.169)	0.131 ± 0.004	211.47 ± (1.61 ± 0.23) [1.62]	1.20 ± (0.10 ± 0.04)
	2008 May 30	K-prime	12.518 ± (0.120 ± 0.041)	0.125 ± 0.001	197.94 ± (0.40 ± 0.02) [0.40]	1.44 ± (0.04 ± 0.03)
	2008 Dec 19	K-prime	8.555 ± (0.080 ± 0.064)	0.085 ± 0.001	172.41 ± (0.81 ± 0.08) [0.82]	1.31 ± (0.08 ± 0.03)
	2008 Dec 19	J	8.944 ± (0.364 ± 0.095)	0.089 ± 0.004	173.17 ± (0.59 ± 0.12) [0.61]	1.63 ± (0.16 ± 0.05)
	2009 Jun 11	K-prime	6.653 ± (0.056 ± 0.354)	0.066 ± 0.004	129.62 ± (0.22 ± 0.04) [0.22]	1.34 ± (0.05 ± 0.02)
LP 415-20	2006 Nov 27	K-prime	4.616 ± (0.083 ± 0.541)	0.046 ± 0.005	35.11 ± (2.40 ± 0.85) [2.55]	1.77 ± (0.09 ± 0.04)
	2007 Dec 01	K-prime	9.617 ± (0.152 ± 0.206)	0.096 ± 0.003	52.45 ± (1.06 ± 0.12) [1.06]	2.53 ± (0.21 ± 0.04)
	2008 Dec 18	K-prime	11.215 ± (0.444 ± 0.044)	0.112 ± 0.004	62.56 ± (0.97 ± 0.10) [0.97]	1.42 ± (0.12 ± 0.03)
	2008 Dec 18	H	11.145 ± (0.179 ± 0.066)	0.111 ± 0.002	62.18 ± (1.26 ± 0.04) [1.36]	1.60 ± (0.19 ± 0.04)

[a] The first listed uncertainty is that due to the measurement itself, while the second is the systematic uncertainty due to imperfect PSF matching. If only one uncertainty is given, the source had a suitable PSF in the field of view.

[b] The uncertainties given are the empirically estimated statistical uncertainty, the PSF mismatch uncertainty, and the absolute plate scale uncertainty added in quadrature

[c] The first listed uncertainty is that due to the measurement itself, while the second is the systematic uncertainty due to imperfect PSF matching. In the paratheses is the combination of these two uncertainties along with the absolute uncertainty of the columns with respect to north. If only one uncertainty is given, the source had a suitable PSF in the field of view.

[d] The first listed uncertainty is systematic uncertainty due to the measurement itself, while the second is that due to imperfect PSF matching. If only one uncertainty is given, the source had a suitable PSF in the field of view.

[e] Data from the OSIRIS imager, which has a plate scale of $0\farcs02$/pixel. This camera has not been fully characterized for distortion. However, the

uncertainties on these measurements are such that they should account for distortion on this camera

Table 6. Radial Velocity Measurements

Target Name	Date of Observation (UT)	Average SNR Primary (A)	Average SNR Secondary (B)	Rad. Velocity Primary (km/s)	Rad. Velocity Secondary (km/s)	ΔRV (km/s)
2MASS 0746+20AB	2006 Dec 16	52	44	55.60 ± 0.68	52.94 ± 0.68	-2.66 ± 0.96
	2007 Dec 04	72	59	55.18 ± 0.60	52.37 ± 1.12	-2.81 ± 1.27
	2008 Dec 19	66	56	56.06 ± 0.85	54.05 ± 2.30	-2.01 ± 2.45
2MASS 1426+15AB	2007 Jun 08	44	33	12.54 ± 0.43	14.41 ± 1.27	1.87 ± 1.34
	2008 Jun 01	50	36	12.67 ± 0.36	15.39 ± 1.40	2.72 ± 1.45
	2009 Jun 12	41	29	12.78 ± 0.49	15.00 ± 0.68	2.22 ± 0.84
2MASS 1750+44AB	2008 May 31	48	36	-17.52 ± 0.39	-15.89 ± 0.54	1.63 ± 0.67
	2009 Jun 12	41	31	-17.09 ± 0.53	-15.25 ± 1.31	1.84 ± 1.41
2MASS 1847+55AB	2007 Jun 08	69	60	-23.88 ± 0.32	-20.46 ± 0.29	3.42 ± 0.43
	2008 Jun 01	69	60	-24.15 ± 0.21	-20.09 ± 0.46	4.06 ± 0.51
	2009 Jun 13	39	36	-24.68 ± 0.60	-19.63 ± 1.00	5.05 ± 1.17
2MASS 2140+16AB	2007 Jun 09	43	28	13.90 ± 0.30	11.07 ± 1.21	-2.83 ± 1.25
	2008 May 31	58	40	13.62 ± 0.27	12.26 ± 1.62	-1.36 ± 1.68
	2009 Jun 13	38	26	13.47 ± 0.28	10.97 ± 2.00	2.50 ± 2.01
2MASS 2206-20AB	2007 Jun 09	47	39	13.66 ± 0.36	13.28 ± 0.48	-0.38 ± 0.66
	2008 Jun 01	54	48	13.14 ± 0.39	13.46 ± 0.51	0.32 ± 0.64
	2009 Jun 12	47	44	13.37 ± 0.24	12.75 ± 0.37	-0.62 ± 0.44
GJ 569b AB	2007 Jun 09	89	82	-10.49 ± 0.20	-4.90 ± 0.50	5.59 ± 0.54
	2009 Jun 13	86	67	-8.97 ± 0.36	-6.83 ± 0.27	2.14 ± 0.45
HD 130948Bc	2007 Jun 09	44	33	4.57 ± 2.61	-0.72 ± 1.05	-5.29 ± 2.81
LHS 2397aAB	2007 Dec 04	68	27	34.43 ± 0.86	34.84 ± 2.24	0.41 ± 2.40
	2008 May 31	114	44	33.85 ± 0.27	36.30 ± 0.86	2.45 ± 0.90
	2008 Dec 19	85	31	33.79 ± 0.37	35.30 ± 2.49	1.51 ± 2.52
	2009 Jun 12	103	33	33.51 ± 0.66	34.27 ± 2.02	0.76 ± 1.22
LP 349-25AB	2006 Dec 16	58	45	-11.91 ± 1.33	-6.57 ± 2.50	5.34 ± 2.83
	2007 Dec 04	63	58	-11.11 ± 3.00	-5.50 ± 3.02	5.67 ± 2.12
	2008 Dec 19	105	84	-9.89 ± 1.51	-6.78 ± 1.84	3.11 ± 0.98
	2009 Jun 12	114	98	-8.16 ± 0.49	-7.27 ± 1.35	0.89 ± 1.44
LP 415-20A	2008 Dec 19	42	32	41.13 ± 0.91	40.41 ± 1.06	-0.72 ± 1.40

Table 7. Astrometric Orbital Parameters

Target Name	Fixed Dist. (pc)	Fit Dist. (pc)	Total System Mass ($M_\odot$)	Period (years)	Semi-Major Axis (mas)	Eccentricity	T_o (years)	Inc. (degrees)	Ω (degrees)	ω (degrees)	Best Fit Reduced χ^2
2MASS 0746+20AB	12.21 ± 0.05[b]	—	0.151 ± 0.003	12.71 ± 0.07	$237.3^{+1.5}_{-0.4}$	0.487 ± 0.003	2002.83 ± 0.01	138.2 ± 0.5	28.4 ± 0.5	354.4 ± 0.9	0.88
2MASS 0850+10AB	38.1 ± 7.3[c]	—	0.2 ± 0.2	24^{+69}_{-6}	126^{100}_{-32}	0.64 ± 0.26	2016^{+9}_{-24}	65 ± 12	96 ± 27	236^{+117}_{-171}	2.85
2MASS 0920+35AB	24.3 ± 5.0[a]	—	0.11 ± 0.11	$6.7^{+3.3}_{3.4}$	69 ± 24	$0.21^{+0.65}_{-0.21}$	2003.43 ± 1.15	88.6 ± 2.4	69.0 a± 1.5	317^{+43}_{-300}	0.92
2MASS 1426+15AB	—	34 ± 13	$0.11^{+0.08}_{-0.11}$	1985^{+2141}_{-1945}	2273 ± 1560	$0.85^{+0.10}_{-0.41}$	1998 ± 24	88.3 ± 0.8	344.8 ± 0.4	282^{+78}_{-210}	1.89
2MASS 1534-29AB	13.59 ± 0.22[d]	—	0.060 ± 0.004	23.1 ± 4.0	234 ± 30	0.10 ± 0.09	2006.4 ± 3.0	85.6 ± 0.4	13.4 ± 0.3	25^{+154}_{-25}	1.57
2MASS 1728+39AB	24.1 ± 2.1[c]	—	$0.15^{+0.25}_{-0.04}$	31.3 ± 12.7	220 ± 26	$0.28^{+0.35}_{-0.28}$	$2017\ ^{+4}_{-22}$	62 ± 7	118^{+11}_{-9}	94 ± 15	2.60
2MASS 1750+44AB	—	37.6 ± 12.3	0.20 ± 0.12	317 ± 240	728 ± 375	0.71 ± 0.18	2004.3 ± 1.8	44 ± 10	99 ± 6	267 ± 26	1.63
2MASS 1847+55AB	—	29.8 ± 7.1	$0.18^{+0.35}_{-0.13}$	44.2 ± 18.7	237 ± 36	$0.1^{+0.5}_{-0.1}$	2020^{+6}_{-28}	79^{+4}_{-2}	125 ± 3	68 ± 30	0.63
2MASS 2140+16AB	—	25 ± 10	0.10 ± 0.08	$20.1^{+5.3}_{-1.6}$	141^{9}_{-6}	0.26 ± 0.06	$2012.0^{+0.5}_{-2.0}$	$46.2^{2.5}_{-8.7}$	104 ± 7	223^{+10}_{-47}	0.50
2MASS 2206-20AB	26.67 ± 2.63[e]	—	0.16 ± 0.05	23.78 ± 0.19	168.0 ± 1.5	$0.000^{+0.002}_{-0.000}$	$2000.0^{+1.9}_{-3.2}$	44.3 ± 0.7	74.8 ± 1.0	326^{+28}_{-52}	2.32
GJ569B ab	9.81 ± 0.16[f]	—	0.126 ± 0.007	2.370 ± 0.002	90.8 ± 0.8	0.310 ± 0.006	2003.150 ± 0.005	33.6 ± 1.3	144.8 ± 1.9	77.4 ± 1.7	1.43
HD 130948BC	18.18 ± 0.08[f]	—	0.109 ± 0.002	9.83 ± 0.16	120.4 ± 1.4	0.16 ± 0.01	2008.6 ± 0.2	95.7 ± 0.2	313.3 ± 0.2	253.3 ± 3.9	2.12
LHS 2397a AB	14.3 ± 0.4[g]	—	0.144 ± 0.013	14.26 ± 0.10	215.8 ± 1.5	0.348 ± 0.006	2006.29 ± 0.04	40.9 ± 1.2	78.0 ± 1.5	217.7 ± 2.6	1.47
LP 349-25AB	13.19 ± 0.28[h]	—	0.121 ± 0.009	7.31 ± 0.37	141 ± 7	0.08 ± 0.02	2002.5 ± 0.8	118.7 ± 1.5	213.8 ± 1.1	109^{+37}_{-22}	2.15
LP 415-20AB	—	21 ± 5	0.09 ± 0.06	11.5 ± 1.2	108 ± 24	0.9 ± 0.1	2006.5 ± 0.2	55 ± 12	200 ± 40	73 ± 50	1.47

[a] No parallax measurement or radial velocity data exists - spectrophotometric distance used here

[b] Distance from parallax measurement by Dahn et al. (2002)

[c] Distance from parallax measurement by Vrba et al. (2004)

[d] Distance from parallax measurement by Tinney et al. (2003)

[e] Distance from parallax measurement by Costa et al. (2006)

[f] Distance from Hipparcos parallax for high mass tertiary companion

[g] Distance from parallax measurement by Monet et al. (1992)

[h] Distance from parallax measurement by Gatewood et al. (2009)

Table 8. Absolute Orbital Parameters

	Fit Parameters			Derived Properties			
Target Name	$K_{Primary}$ (km/s)	Center of Mass Velocity (km/s)	Best Fit Reduced χ^2	$K_{Secondary}$ (km/s)	Mass Ratio ($M_{Primary}$ / $M_{Secondary}$)	$M_{Primary}$ ($M_\odot$)	$M_{Secondary}$ ($M_\odot$)
2MASS 0746+20AB	$1.0^{+3.0}_{-0.1}$	54.7 ± 0.8	0.44	$4.1^{+0.1}_{-3.1}$	4.0 ± 0.1	$0.12^{+0.01}_{-0.09}$	$0.03^{+0.09}_{-0.01}$
2MASS 2140+16AB	0.8 ± 0.3	13.0 ± 0.2	0.9	3.1 ± 1.1	$4.0^{+0}_{-0.1}$	0.08 ± 0.06	$0.02^{+0.08\,\mathrm{a}}_{-0.02}$
2MASS 2206-20AB	0.8 ± 0.2	13.3 ± 0.2	2.2	3.1 ± 0.4	$4.0^{+0.0}_{-0.2}$	0.13 ± 0.05	$0.03^{+0.07\,\mathrm{a}}_{-0.02}$
GJ 569b AB	2.7 ± 0.3	$-8.0 \pm 0.2^{\mathrm{b}}$	0.56	3.8 ± 0.4	1.4 ± 0.3	0.073 ± 0.008	0.053 ± 0.006
LHS 2397a AB	1.7 ± 1.2	34.6 ± 1.4	0.41	2.6 ± 1.4	$1.5^{+7.1}_{-1.4}$	0.09 ± 0.05	0.06 ± 0.05
LP 349-25 AB	4.5 ± 0.9	-8.0 ± 0.5	0.8	2.2 ± 0.9	0.5 ± 0.3	0.04 ± 0.02	0.08 ± 0.02

Note. — Using our absolute radial velocities in conjunction with the parameters from our relative orbital solutions, we fit for $K_{Primary}$ and γ. We then use those values to find $K_{Secondary}$ and the mass ratio. We combine the mass ratio and the total system mass from the relative orbits to find component masses.

[a] Upper uncertainty set using the uncertainty in $M_{Primary}$ and M_{Tot}

[b] Set to our value

Table 9. Photometric Measurements

Target Name	M_{F625W}	M_{F775W}	M_{814W}	M_{850LP}	M_{F1042}	M_J	M_H	M_{Kp}	L_{Bol} (Log $L/L_\odot$)	T_{Eff} (K)	Rad. (R_{Jup})	Phot. Ref
2MASS 0746+20A	18.36 ± 0.05	15.55 ± 0.05	14.98 ± 0.15	13.81 ± 0.05	—	11.85 ± 0.04	11.13 ± 0.02	10.62 ± 0.02	-3.64 ± 0.02	2205 ± 15	0.99 ± 0.03	1
2MASS 0746+20B	18.86 ± 0.06	16.23 ± 0.07	15.98 ± 0.18	14.57 ± 0.06	—	12.36 ± 0.10	11.57 ± 0.03	10.98 ± 0.02	-3.77 ± 0.02	2060 ± 50	0.97 ± 0.06	1
2MASS 0850+10A	20.93 ± 0.50	18.41 ± 0.48	17.39 ± 0.44	16.17 ± 0.48	—	—	—	11.99 ± 0.42	-4.22 ± 0.18	1590 ± 290	1.0 ± 0.3	2
2MASS 0850+10B	22.24 ± 0.57	19.57 ± 0.50	18.86 ± 0.45	17.03 ± 0.49	—	—	—	12.80 ±0.43	-4.47 ± 0.18	1380 ± 250	1.0 ± 0.3	2
2MASS 0920+35A	—	—	17.90 ± 0.48	—	—	14.43 ± 0.47	13.40 ± 0.45	12.65 ± 0.45	-4.47 ± 0.19	1375 ± 250	1.0 ± 0.3	3
2MASS 0920+35B	—	—	18.78 ± 0.49	—	—	14.47 ± 0.56	13.60 ± 0.46	12.97 ± 0.46	-4.54 ± 0.20	1320 ± 250	1.0 ± 0.3	3
2MASS 1426+15A	16.98 ± 0.87	13.92 ± 0.86	13.49 ± 0.85	12.23 ± 0.86	11.33 ± 0.85	10.69 ± 0.83	10.00 ± 0.83	9.55 ± 0.83	-3.19 ± 0.34	2400 ± 50	$1.37^{+0.54}_{-0.59}$	4
2MASS 1426+15B	17.98 ± 0.87	15.16 ± 0.87	14.89 ± 0.85	13.29 ± 0.86	12.63 ± 0.85	11.46 ± 0.83	10.70 ± 0.83	10.20 ± 0.83	-3.48 ± 0.34	2240 ± 50	$1.12^{+0.48}_{-0.50}$	4
2MASS 1534-29A	—	—	19.57 ± 0.04	—	15.74 ± 0.12	14.61 ± 0.10	14.79 ± 0.11	14.84 ± 0.12	-4.97 ± 0.10	1130 ± 20	0.80 ± 0.03	5
2MASS 1534-29B	—	—	19.87 ± 0.05	—	15.94 ± 0.24	14.77 ± 0.10	15.14 ± 0.13	15.03 ± 0.13	-5.05 ± 0.10	1097 ± 20	0.80 ± 0.03	5
2MASS 1728+39A	—	—	18.35 ± 0.25	—	15.89 ± 0.21	14.68 ± 0.20	13.40 ± 0.20	12.47 ± 0.20	-4.38 ± 0.10	1450 ± 230	1.0 ± 0.3	3
2MASS 1728+39B	—	—	19.00 ± 0.28	—	15.64 ± 0.22	15.00 ± 0.20	13.85 ± 0.20	13.13 ± 0.20	-4.60 ± 0.10	1280 ± 200	1.0 ± 0.3	3
2MASS 1750+44A	—	—	—	—	—	10.30 ± 0.71	9.72 ± 0.71	9.36 ± 0.71	-3.08 ± 0.29	2200 ± 100	$1.88^{+0.72}_{-0.73}$	6
2MASS 1750+44B	—	—	—	—	—	11.26 ± 0.71	10.49 ± 0.72	10.03 ± 0.71	-3.40 ± 0.29	2020 ± 60	$1.62^{+0.78}_{-0.65}$	6
2MASS 1847+55A	—	—	—	—	—	10.19 ± 0.52	9.52 ± 0.52	9.16 ± 0.52	-2.98 ± 0.22	2400 ± 300	$1.70^{+0.26}_{-0.28}$	6
2MASS 1847+55B	—	—	—	—	—	10.43 ± 0.53	9.81 ± 0.55	9.43 ± 0.52	-3.11 ± 0.22	2100 ± 100	1.99 ± 0.59	6
2MASS 2140+16A	—	—	14.05 ± 0.89	—	11.79 ± 0.89	11.33 ± 0.87	10.66 ± 0.87	10.28 ± 0.87	-3.48 ± 0.35	2300 ± 65	$1.13^{+0.47}_{-0.44}$	3
2MASS 2140+16B	—	—	15.56 ± 0.89	—	13.17 ± 0.89	12.28 ± 0.88	11.59 ± 0.89	11.02 ± 0.87	-3.83 ± 0.35	2075 ± 50	$0.92^{+0.39}_{-0.36}$	3
2MASS 2206-20A	—	—	13.59 ± 0.21	—	11.81 ± 0.21	10.92 ± 0.21	10.28 ± 0.22	9.91 ± 0.21	-3.32 ± 0.10	2350 ± 60	$1.27^{+0.15}_{-0.14}$	3
2MASS 2206-20B	—	—	13.67 ± 0.21	—	11.83 ± 0.21	11.07 ± 0.22	10.33 ± 0.24	9.98 ± 0.21	-3.35 ± 0.10	2250 ± 60	$1.30^{+0.15}_{-0.18}$	3
GJ 569Ba	—	—	—	—	—	11.18 ± 0.08	10.47 ± 0.05	9.90 ± 0.06	-3.33 ± 0.07	2000 ± 40	1.69 ± 0.09	7
GJ 569Bb	—	—	—	—	—	11.69 ± 0.08	11.08 ± 0.06	10.43 ± 0.07	-3.56 ± 0.07	2000 ± 65	1.28 ± 0.07	7
HD 130948B	—	—	—	—	—	12.51 ± 0.06	11.74 ± 0.10	10.96 ± 0.03	-3.84 ± 0.06	1840 ± 40	1.09 ± 0.03	8
HD 130948C	—	—	—	—	—	12.82 ± 0.07	12.03 ± 0.11	11.16 ± 0.03	-3.92 ± 0.06	1790 ± 40	1.02 ± 0.03	8
LHS 2397aA	—	—	14.29 ± 0.07	—	—	11.33 ± 0.06	10.52 ± 0.07	10.04 ± 0.07	-3.37 ± 0.07	2180^{+50}_{-90}	1.28 ± 0.15	9
LHS 2397aB	—	—	18.71 ± 0.18	—	—	14.45 ± 0.10	13.62 ± 0.10	12.82 ± 0.07	-4.50 ± 0.07	1350 ± 210	1.0 ± 0.3	9
LP 349-25A	—	—	—	—	—	10.53 ± 0.05	9.93 ± 0.06	9.58 ± 0.06	-3.19 ± 0.06	2200 ± 45	$1.70^{+0.08}_{-0.09}$	6
LP 349-25B	—	—	—	—	—	11.07 ± 0.07	10.35 ± 0.09	9.88 ± 0.09	-3.34 ± 0.07	2050 ± 50	$1.68^{+0.09}_{-0.08}$	6
LP 415-20A	—	—	—	—	—	11.48 ± 0.52	10.98 ± 0.52	10.64 ± 0.52	-3.57 ± 0.22	2300 ± 150	$1.00^{+0.24}_{-0.29}$	6
LP 415-20B	—	—	—	—	—	12.32 ± 0.54	11.49 ± 0.54	11.02 ± 0.53	-3.80 ± 0.22	2000 ± 100	$1.00^{+0.30}_{-0.25}$	6

Note. — References for photometric measurements: (1) Optical from Bouy et al. (2004), NIR from this work; (2) F814W from Bouy et al. (2003), all others from this work; (3) Optical from Bouy et al. (2003), NIR from this work; (4) F814W and F1042M from Bouy et al. (2003), all others from this work; (5) F814W and J from Liu et al. (2008), F1042M from Burgasser et al. (2003), all others from this work; (6) All photometry from this work; (7) Photometry from Lane et al. (2001) and Simon et al. (2006); (8) Photometry from Dupuy et al. (2009a); (9) Optical from Freed et al. (2004), J from Dupuy et al. (2009b), all others from this work

Table 10. Evolutionary Model Predictions

Target Name	$M_{Primary}$ Tucson ($M_\odot$)	$M_{Secondary}$ (Tucscon ($M_\odot$)	M_{Total} Tucscon ($M_\odot$)	$M_{Primary}$ DUSTY ($M_\odot$)	$M_{Secondary}$ DUSTY ($M_\odot$)	M_{Total} DUSTY ($M_\odot$)	$M_{Primary}$ COND ($M_\odot$)	$M_{Secondary}$ COND ($M_\odot$)	M_{Total} COND ($M_\odot$)
2MASS 0746+20AB	0.050 ± 0.005	0.050 ± 0.010	0.10 ± 0.01	0.066 ± 0.005	0.060 ± 0.010	0.13 ± 0.01	—	—	—
2MASS 0850+10AB	0.04 ± 0.04	0.04 ± 0.04	0.08 ± 0.06	$0.04^{+0.04}_{-0.03}$	$0.04^{+0.04}_{-0.03}$	$0.08^{+0.06}_{-0.04}$	$0.03^{+0.05}_{-0.03}$	$0.03^{+0.05}_{-0.03}$	$0.06^{+0.07}_{-0.04}$
2MASS 0920+35AB	0.04 ± 0.04	$0.03^{+0.05}_{-0.03}$	$0.07^{+0.06}_{-0.05}$	$0.04^{+0.04}_{-0.03}$	$0.03^{+0.05}_{-0.03}$	$0.07^{+0.06}_{-0.04}$	$0.03^{+0.05}_{-0.03}$	$0.03^{+0.05}_{-0.03}$	$0.06^{+0.07}_{-0.04}$
2MASS 1426+15AB	$0.03^{+0.04}_{-0.02}$	$0.04^{+0.04}_{-0.03}$	$0.07^{+0.06}_{-0.04}$	$0.04^{+0.04}_{-0.02}$	0.05 ± 0.03	$0.09^{+0.05}_{-0.04}$	—	—	—
2MASS 1534-29AB	0.06 ± 0.02	0.06 ± 0.02	0.12 ± 0.03	—	—	—	$0.04^{+0.03}_{-0.01}$	$0.04^{+0.04}_{-0.01}$	$0.08^{+0.05}_{-0.01}$
2MASS 1728+39AB	0.04 ± 0.04	$0.03^{+0.05}_{-0.03}$	$0.07^{+0.06}_{-0.05}$	0.04 ± 0.04	0.04 ± 0.04	0.08 ± 0.06	$0.03^{+0.05}_{-0.03}$	$0.03^{+0.04}_{-0.03}$	$0.06^{+0.06}_{-0.04}$
2MASS 1750+44AB	0.01 ± 0.01	$0.01^{+0.03}_{-0.01}$	$0.02^{+0.03}_{-0.01}$	0.02 ± 0.02	0.02 ± 0.02	0.04 ± 0.03	—	—	—
2MASS 1847+55AB	$0.02^{+0.03}_{-0.02}$	0.01 ± 0.01	$0.03^{+0.03}_{-0.02}$	$0.03^{+0.05}_{-0.02}$	$0.01^{+0.02}_{-0.01}$	$0.04^{+0.05}_{-0.02}$	—	—	—
2MASS 2140+16AB	$0.04^{+0.05}_{-0.03}$	$0.07^{+0.03}_{-0.05}$	0.11 ± 0.06	0.06 ± 0.04	$0.07^{+0.03}_{-0.04}$	$0.13^{+0.05}_{-0.06}$	—	—	—
2MASS 2206-20AB	0.032 ± 0.010	$0.026^{+0.007}_{-0.010}$	$0.058^{+0.012}_{-0.014}$	$0.047^{+0.016}_{-0.012}$	$0.037^{+0.011}_{-0.009}$	$0.084^{+0.019}_{-0.015}$	—	—	—
GJ569B ab	0.01 ± 0.01	0.02 ± 0.01	0.03 ± 0.01	0.015 ± 0.005	$0.027^{+0.013}_{-0.007}$	$0.042^{+0.014}_{-0.009}$	—	—	—
HD 130948BC	0.030 ± 0.010	0.032 ± 0.010	0.062 ± 0.014	0.035 ± 0.010	$0.037^{+0.013}_{-0.010}$	$0.072^{+0.016}_{-0.014}$	—	—	—
LHS2397a AB	0.02 ± 0.01	0.04 ± 0.04	0.06 ± 0.04	0.03 ± 0.01	0.04 ± 0.04	0.07 ± 0.04	—	$0.03^{+0.04}_{-0.03}$	$0.06^{+0.04}_{-0.03}$[a]
LP 349-25AB	0.014 ± 0.005	0.010 ± 0.005	0.024 ± 0.007	0.024 ± 0.005	0.020 ± 0.005	0.044 ± 0.007	—	—	—
LP 415-20AB	$0.06^{+0.04}_{-0.03}$	0.05 ± 0.03	$0.11^{+0.05}_{-0.04}$	$0.08^{+0.02}_{-0.05}$	$0.06^{+0.02}_{-0.04}$	$0.14^{+0.03}_{-0.06}$	—	—	—

[a] Total mass found by adding DUSTY prediction for primary to COND prediction for secondary

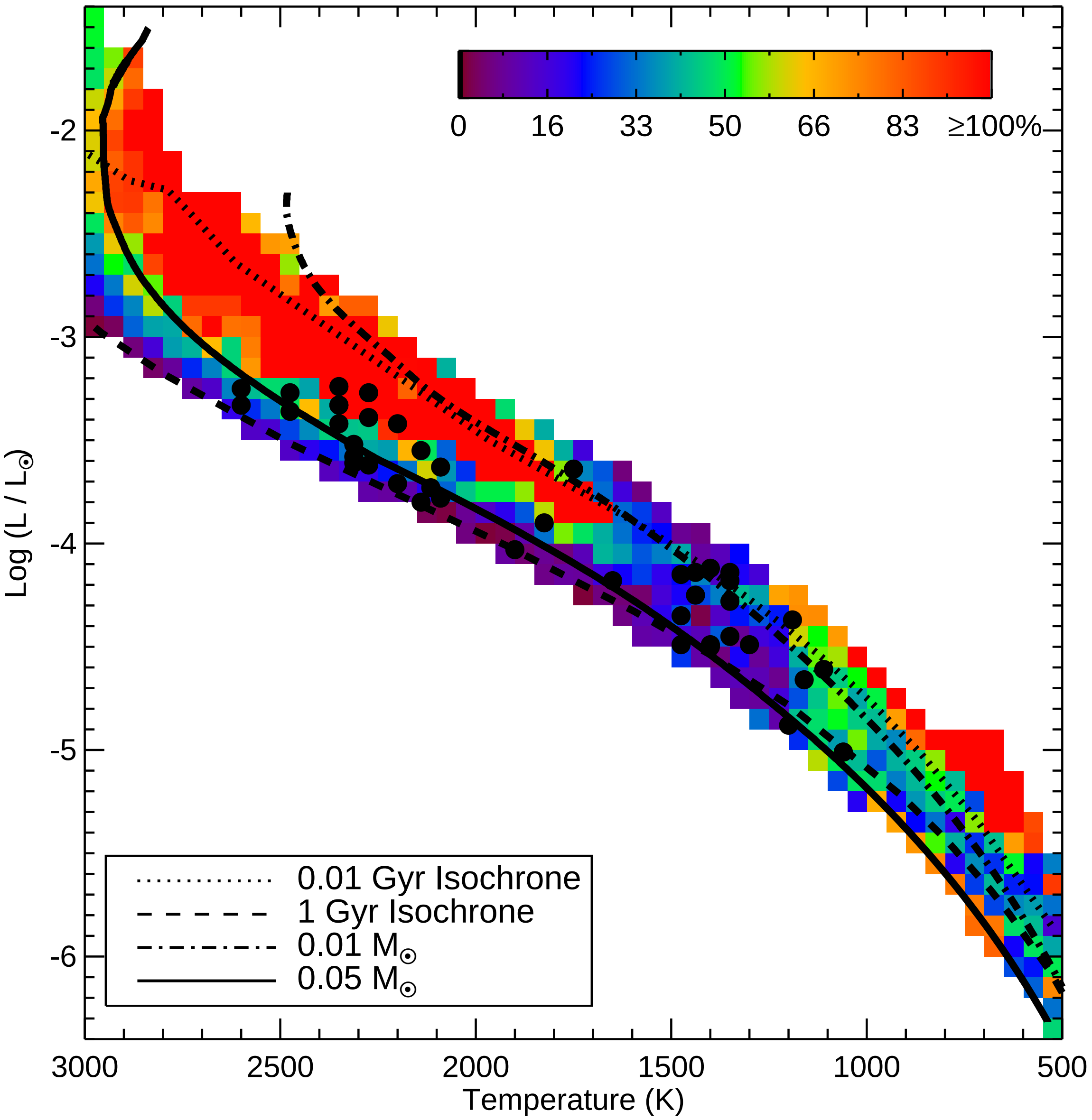

Fig. 1.— Percent discrepancy in mass predictions between the Burrows et al. (1997) evolutionary and the Chabrier et al. (2000) evolutionary models, over the range on the H-R diagram with complimentary coverage. The colors represent the level of the discrepancy in units of percent of the mass predicted by the Burrows et al. (1997) models, as shown by the scale bar. For the majority of the H-R Diagram, the discrepancy between the model predictions is $\gtrsim$10%, with a number of regions having discrepancies greater than 100%. Overplotted are two isochrones and lines of constant mass from the Burrows et al. (1997) models for points of reference. In addition, the overplotted filled points show the rough location of the sources in our full sample. The largest discrepancies are at the youngest ages, but the discrepancies are still substantial for older objects.

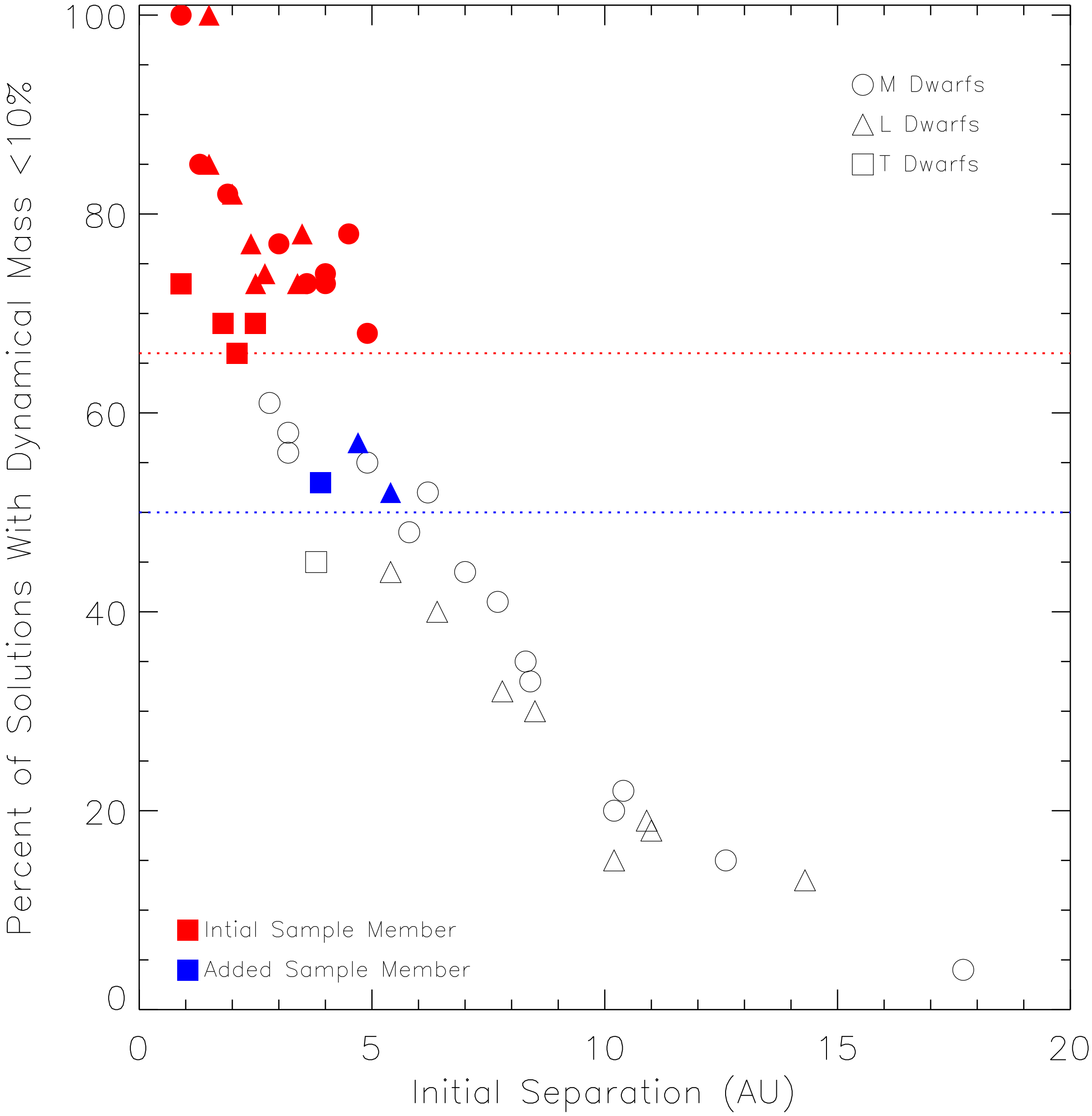

Fig. 2.— The percent of solutions in our Monte Carlo simulations that yielded a mass with $\lesssim$10% precis ion versus the initial separation of the binary. Sources included in our sample are denoted in red, with the red dotted line showing our cutoff of 66%. Additional sample members are denoted in blue, and were chosen because they had either L or T spectral types and because they had a probability of >50% of yielding a precise mass in our initial simulations (with an increased probability for high precision masses by 2012). The symbol type denotes the spectral type of the primary component.

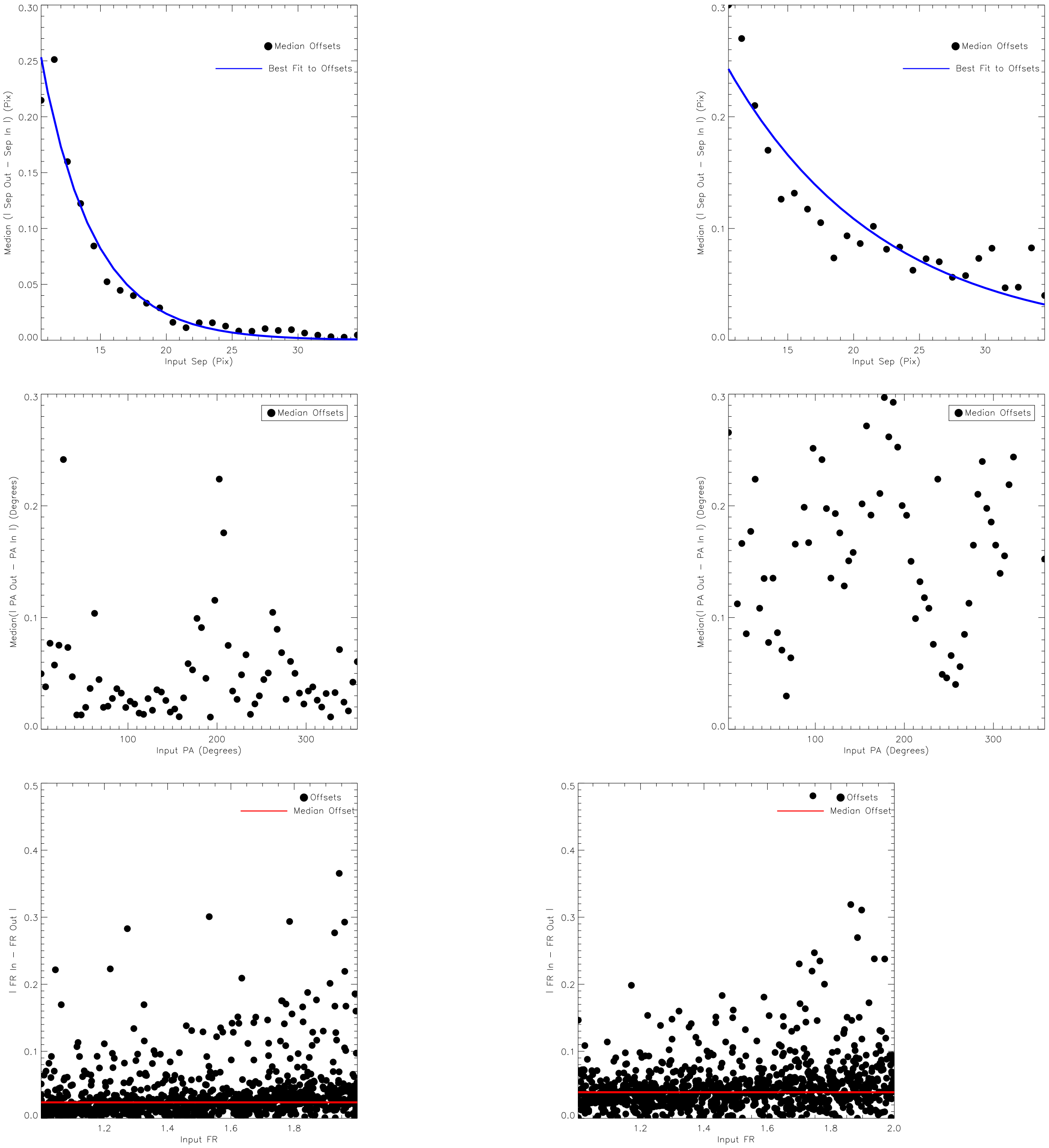

Fig. 3.— Results of PSF systematics simulation from 2006 May 21, using two observed PSFs (left column) and one observed, one simulated PSF (right column). **Top**: Median offset in fit separation from input separation, binned in one pixel increments. The absolute value of these offsets is an exponentially decreasing function of separation. The blue line shows the fit of an exponential function to these offsets. We use this function to determine the additional uncertainty necessary for a source given its fit separation. **Middle**: Median offset in fit position angle (PA) from input PA, binned in 5 degree increments. Because of variable PSF structure, the offsets have no obvious functional form. We therefore use these binned data to apply an additional uncertainty in PA given the PA of the binary. **Bottom** Measured absolute offsets in fit flux ratio from input flux ratio. We use the median of all these values, represented by the red line, as the additional uncertainty in flux ratio.

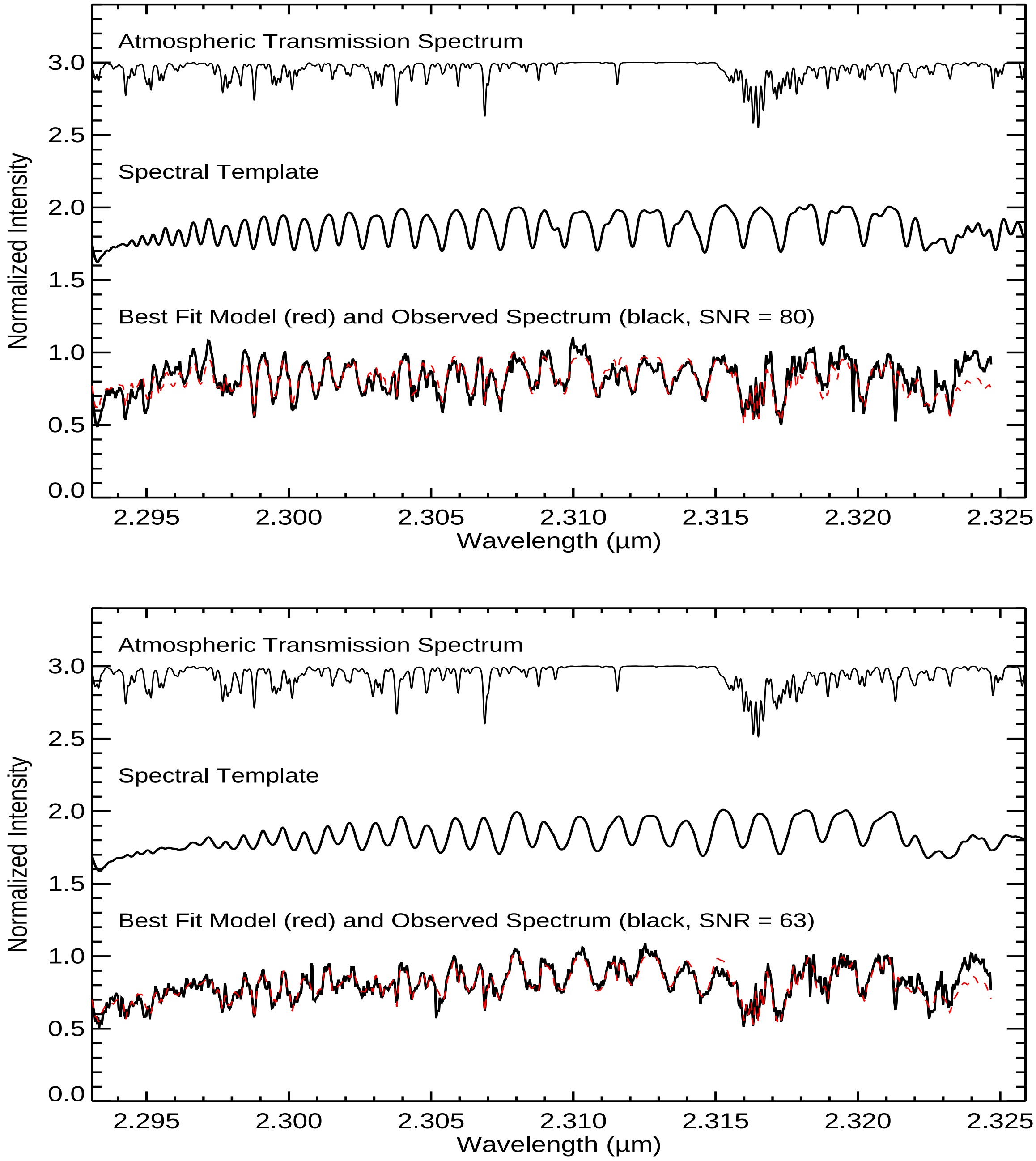

Fig. 4.— Example of a fit for radial velocity for the components of 2MASS 0746+20 A (**top**) and B (**bottom**) from the night of 2007 Dec 04. The atmospheric transmission spectrum used for wavelength calibration is shown, as well as the theoretical spectral template. On the bottom of each panel, we plot our actual spectrum in black (note that the telluric features have not been removed, as is necessary for the fitting) and overplot in red the best fitting model that combines the synthetic atmospheric and spectral templates. Example spectra for all other systems with NIRSPAO measurements are shown online.

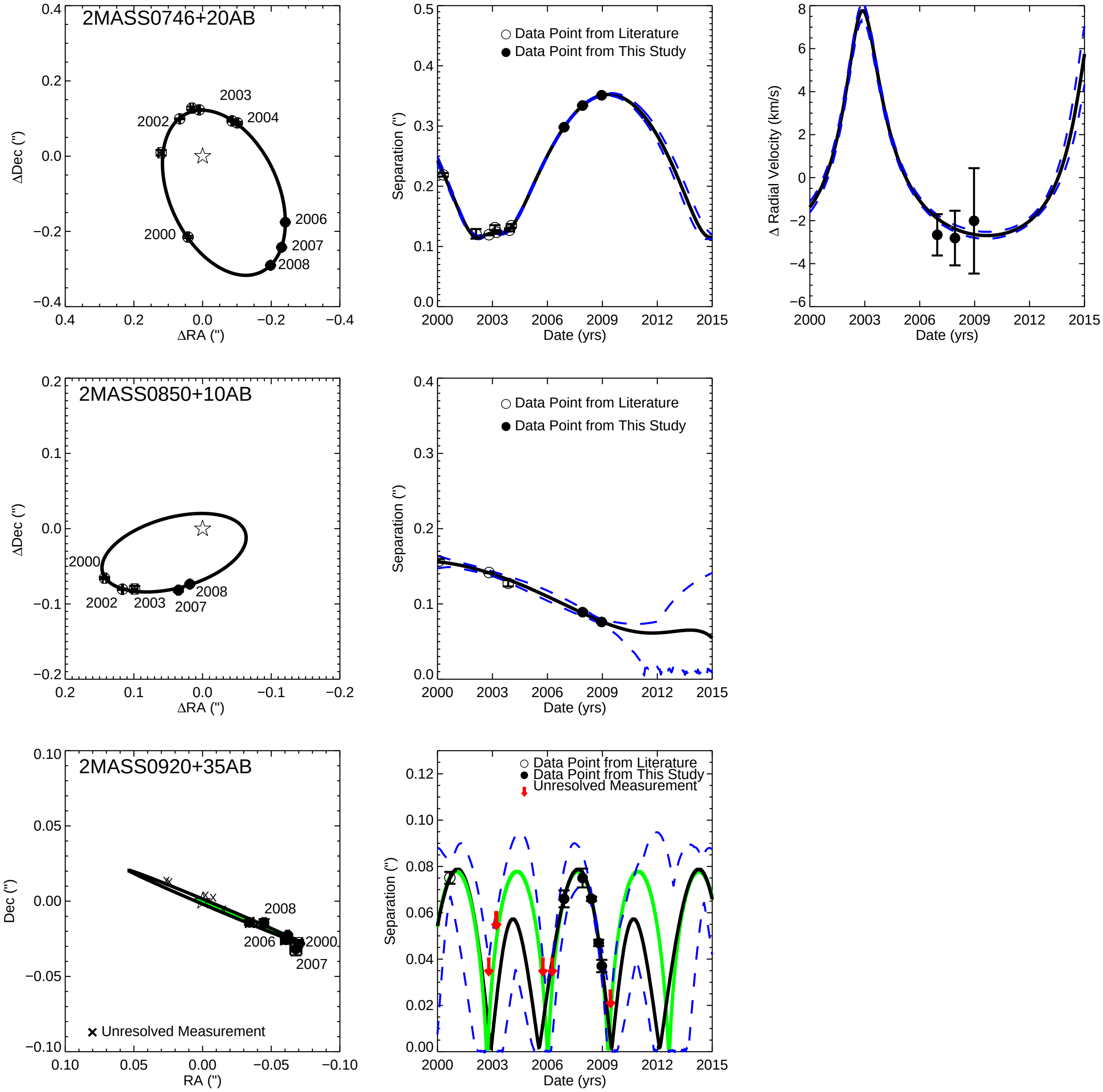

Fig. 5.— Best fit relative orbit for 2MASS0746+20AB (top), 2MASS 0850+10 AB (middle) and 2MASS 0920+35AB (bottom). The left panel shows the relative astrometry data points overplotted with the best fit orbit. The middle panel shows separation of the components as a function of time overplotted with the best fit orbit. Finally, the right hand panel shows the relative radial velocity measurements as a function of time overplotted with the best fit orbit. The blue dotted lines represent the 1σ allowed range of separations and relative radial velocities at a given time. Astrometric data from the literature is from Reid et al. (2001), Bouy et al. (2004), and Buoy et al (2008 - unresolved data points for 2MASS 0920+35AB). For 2MASS 0920+35 (bottom), the black line shows the best fit orbital solution (period ∼6.7 years), while the green line shows the other allowed solution which has a very short period (∼3.3 years) and a high eccentricity. The unresolved measurements from Bouy et al. (2008) are used to throw out solutions that do not lead to the binary being unresolved on those dates (Xs and arrows).

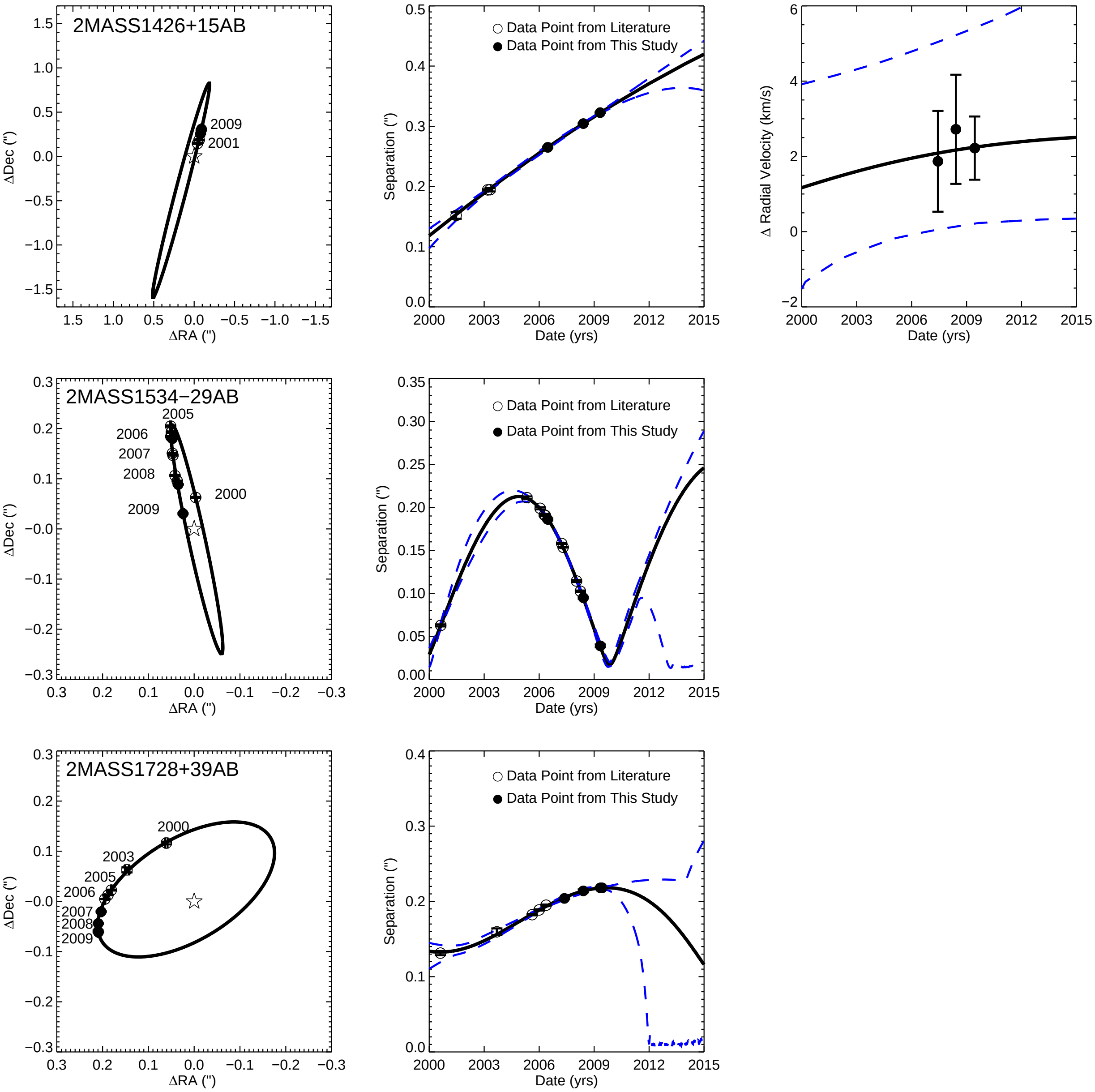

Fig. 6.— Best fit relative orbit for 2MASS1426+15AB (top), 2MASS 1534-29AB (middle), and 2MASS1728+39AB. The left panel shows the relative astrometry data points overplotted with the best fit orbit. The middle panel shows separation of the components as a function of time overplotted with the best fit orbit. Finally, the right hand panel shows the relative radial velocity measurements as a function of time overplotted with the best fit orbit. The blue dotted lines represent the 1σ allowed range of separations and relative radial velocities at a given time. Astrometric data from the literature is from Close et al. (2002), Bouy et al. (2003), Burgasser et al. (2003), Bouy et al. (2008), and Liu et al. (2008).

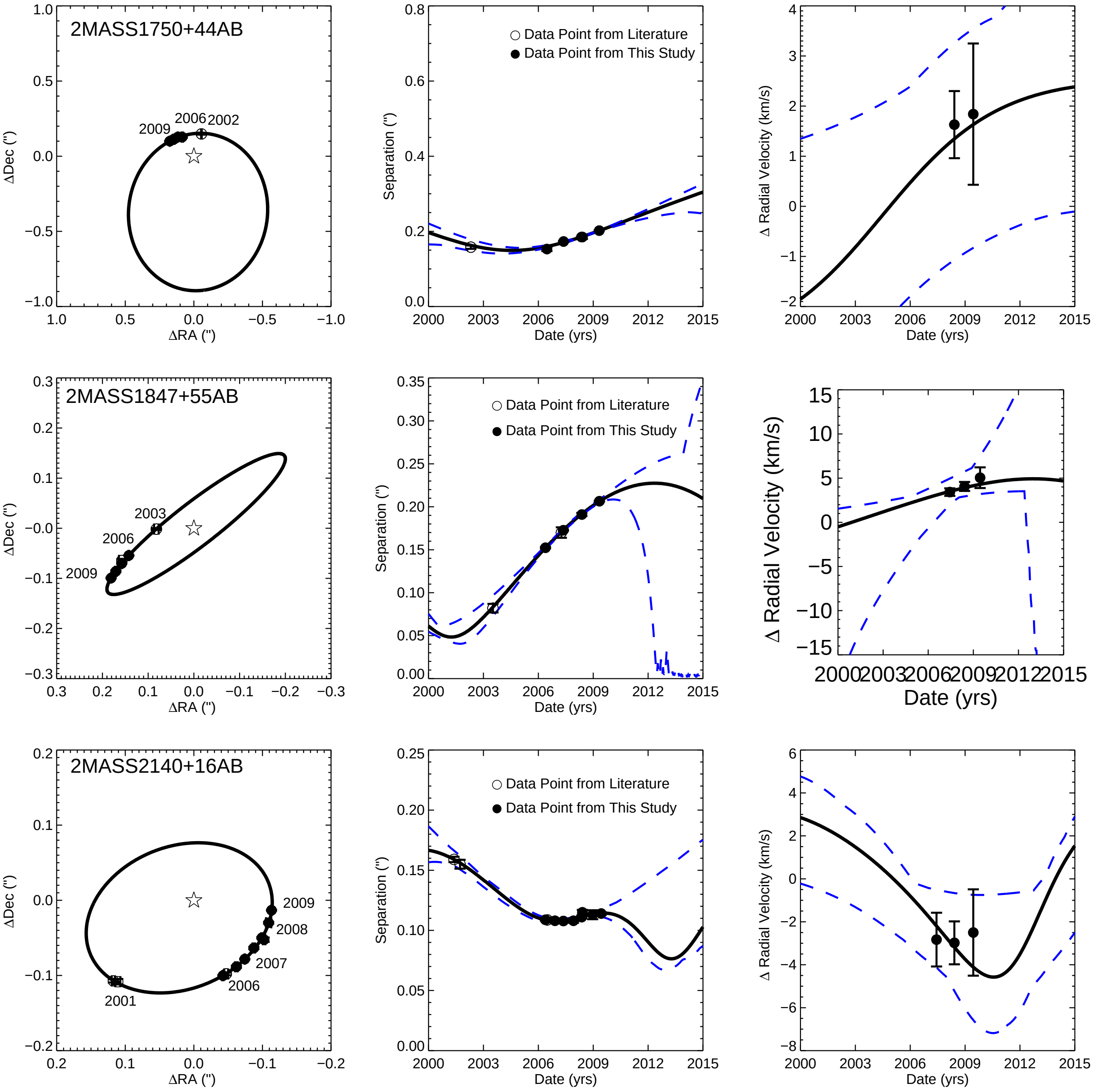

Fig. 7.— Best fit relative orbit for 2MASS1750+44AB (top), 2MASS1847+55AB (middle), and 2MASS2140+16AB. The left panel shows the relative astrometry data points overplotted with the best fit orbit. The middle panel shows separation of the components as a function of time overplotted with the best fit orbit. Finally, the right hand panel shows the relative radial velocity measurements as a function of time overplotted with the best fit orbit. The blue dotted lines represent the 1σ allowed range of separations and relative radial velocities at a given time. Astrometric data from the literature is from Bouy et al. (2003), Close et al. (2003), Siegler et al. (2003), Siegler et al. (2005), and Bouy et al. (2008)

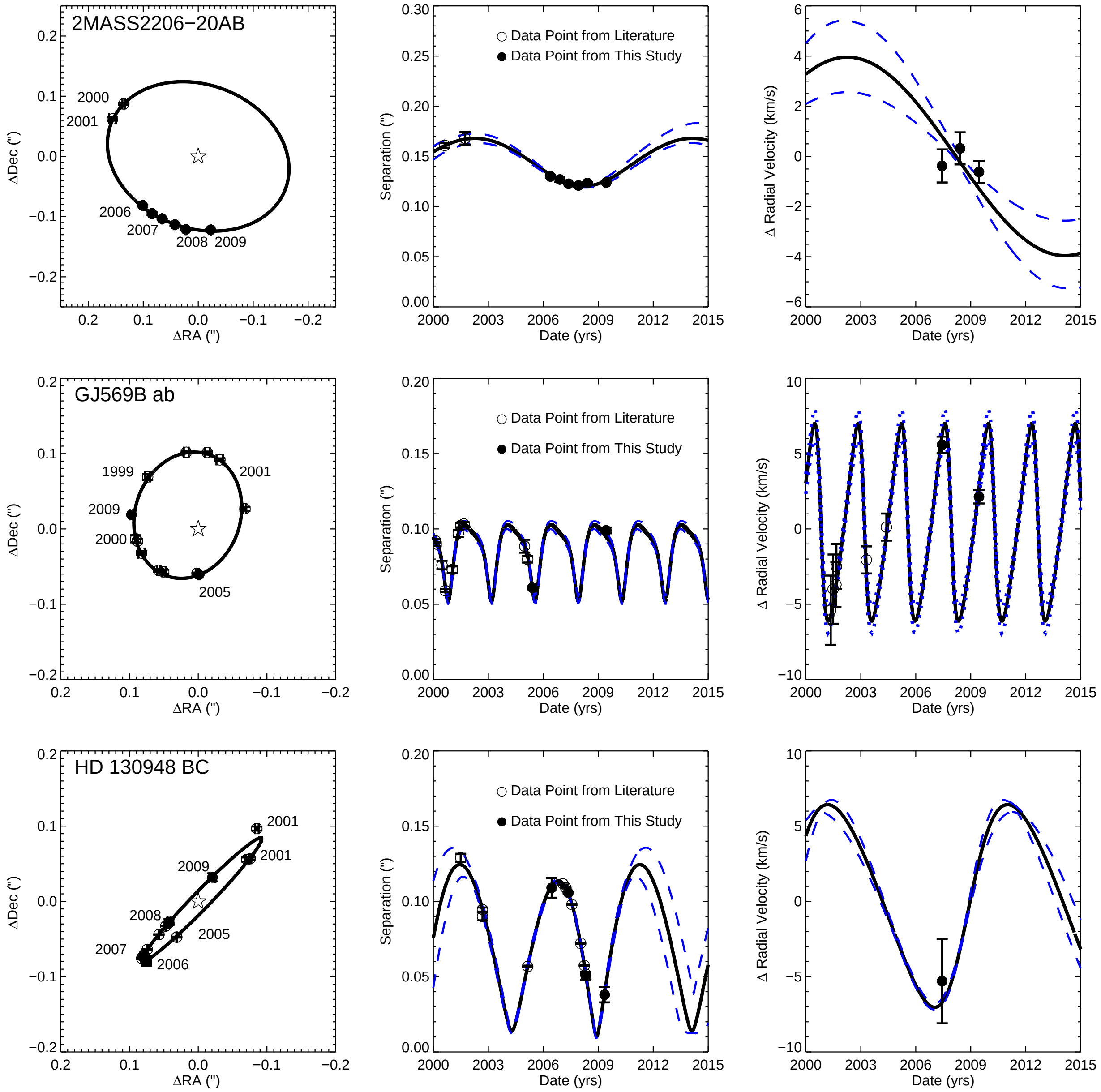

Fig. 8.— Best fit relative orbit for 2MASS2206-20AB (top), GJ 569Bab (middle) and HD 130948BC (bottom). The left panel shows the relative astrometry data points overplotted with the best fit orbit. The middle panel shows separation of the components as a function of time overplotted with the best fit orbit. Finally, the right hand panel shows the relative radial velocity measurements as a function of time overplotted with the best fit orbit. The blue dotted lines represent the 1σ allowed range of separations and relative radial velocities at a given time. Astrometric and radial velocity data from the literature is from Close et al. (2002), Potter et al. (2002), Bouy et al. (2003), Zapatero Osorio et al. (2004), Simon et al. (2006), and Dupuy et al. (2009a).

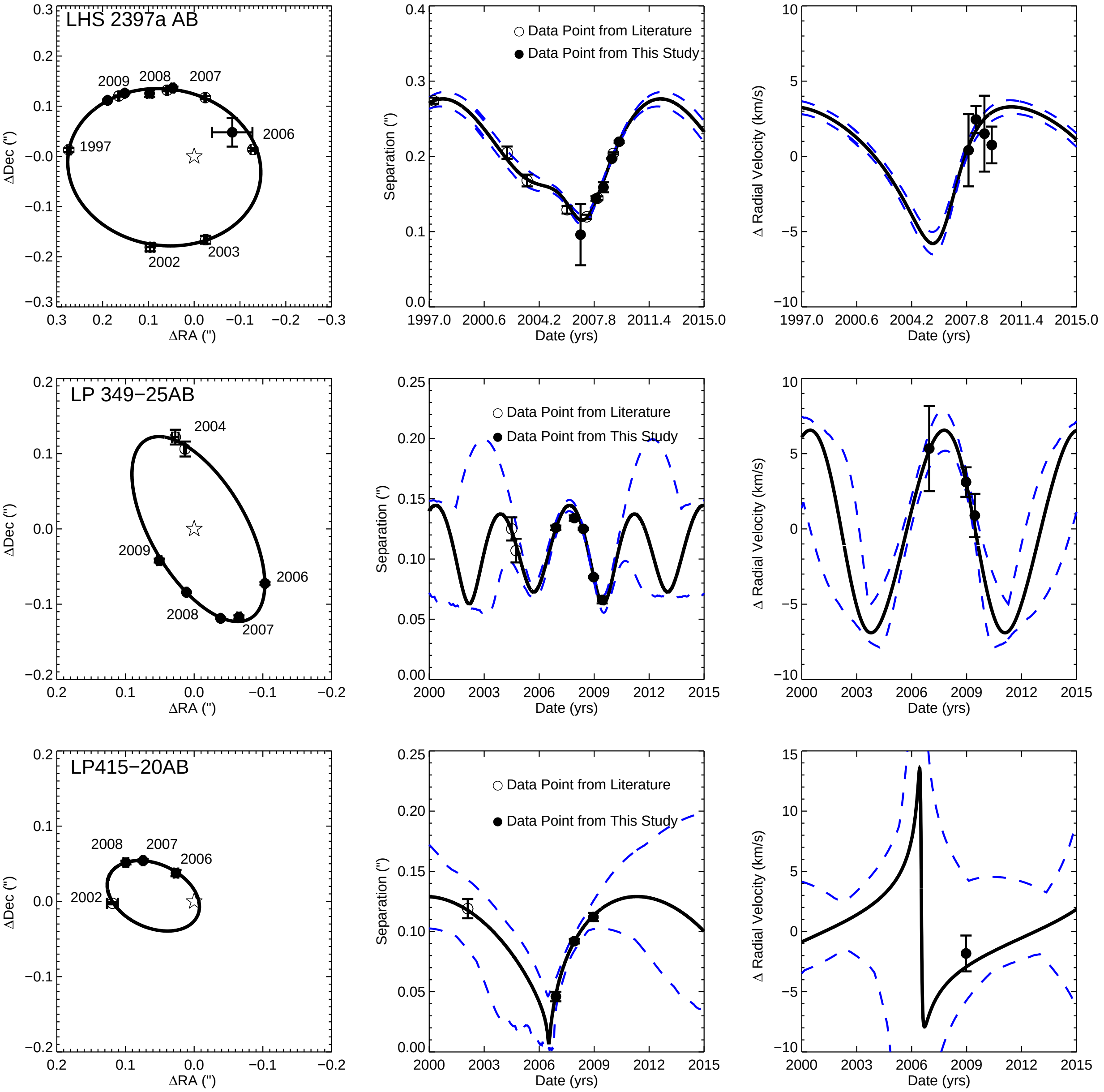

Fig. 9.— Best fit relative orbit for LHS 2397a AB (top), LP 349-25AB (middle) and LP 415-20AB (bottom). The left panel shows the relative astrometry data points overplotted with the best fit orbit. The middle panel shows separation of the components as a function of time overplotted with the best fit orbit. Finally, the right hand panel shows the relative radial velocity measurements as a function of time overplotted with the best fit orbit. The blue dotted lines represent the 1σ allowed range of separations and relative radial velocities at a given time. Astrometric data from the literature taken from Freed et al. (2003), Forveille et al. (2005), Siegler et al. (2005), and Dupuy et al. (2009b).

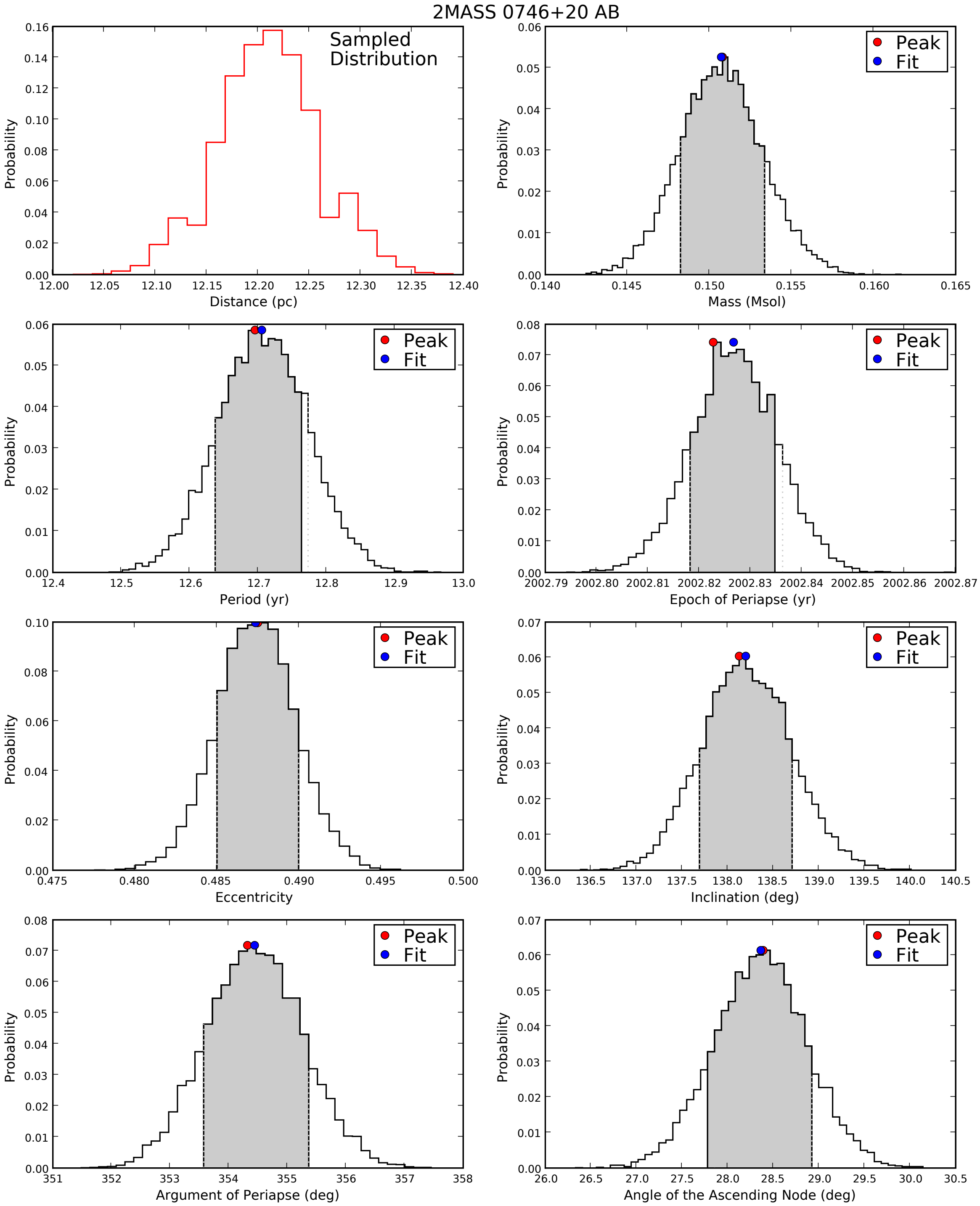

Fig. 10.— One-dimensional PDFs for the relative orbit (total system mass) of 2MASS 0746+20AB. This is an example of a typical system with a well-measured mass and a distance sample from a parallax measurement.

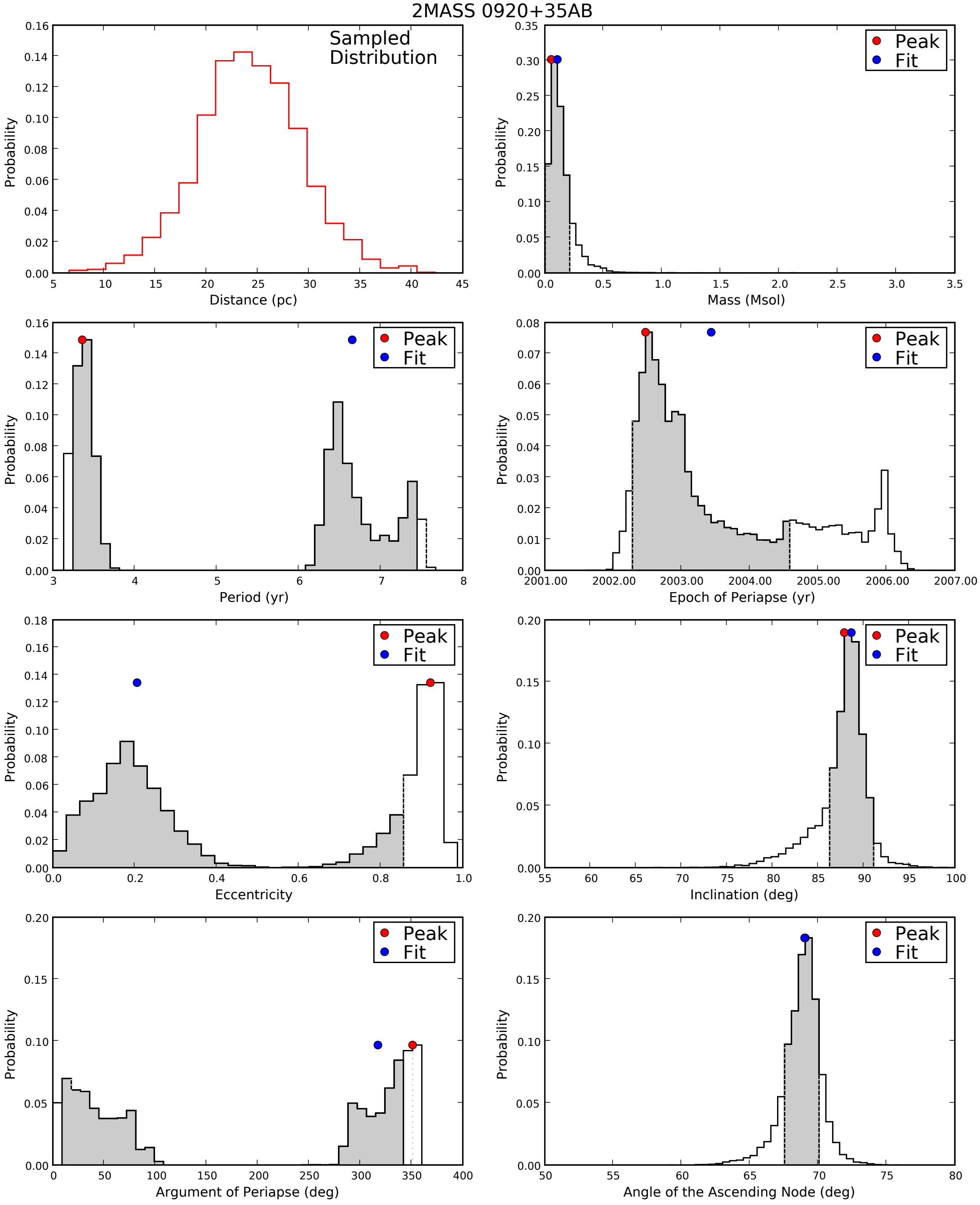

Fig. 11.— One-dimensional PDFs for the relative orbit (total system mass) of 2MASS 0920+35AB. A set of solutions exists with a period of ∼3.5 years and very high eccentricities, making the distributions of period, e and ω strongly bifurcated.

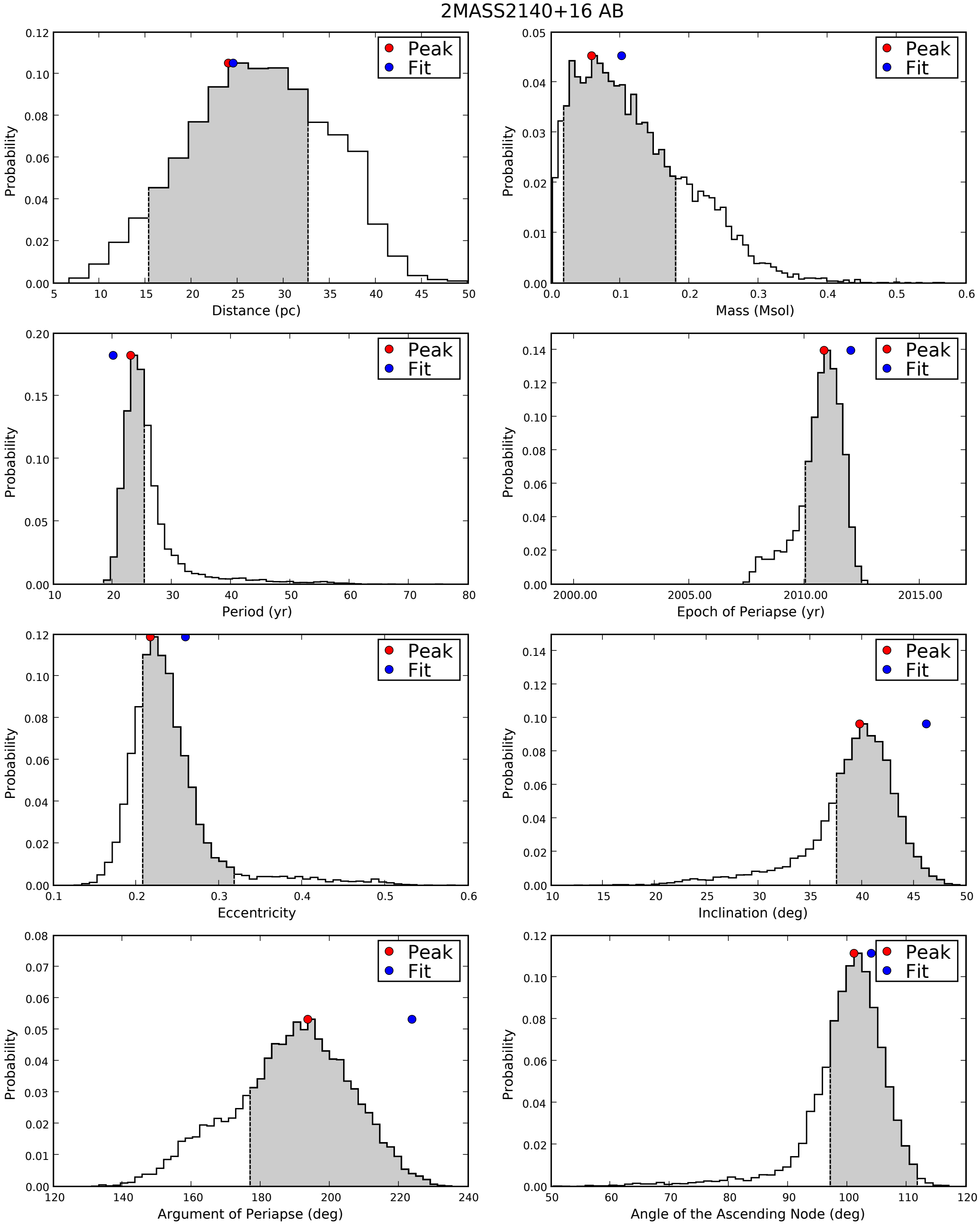

Fig. 12.— One-dimensional PDFs for the relative orbit (total system mass) of 2MASS 2140+16AB. This is an example of a system for which we fit for distance using our relative radial velocities

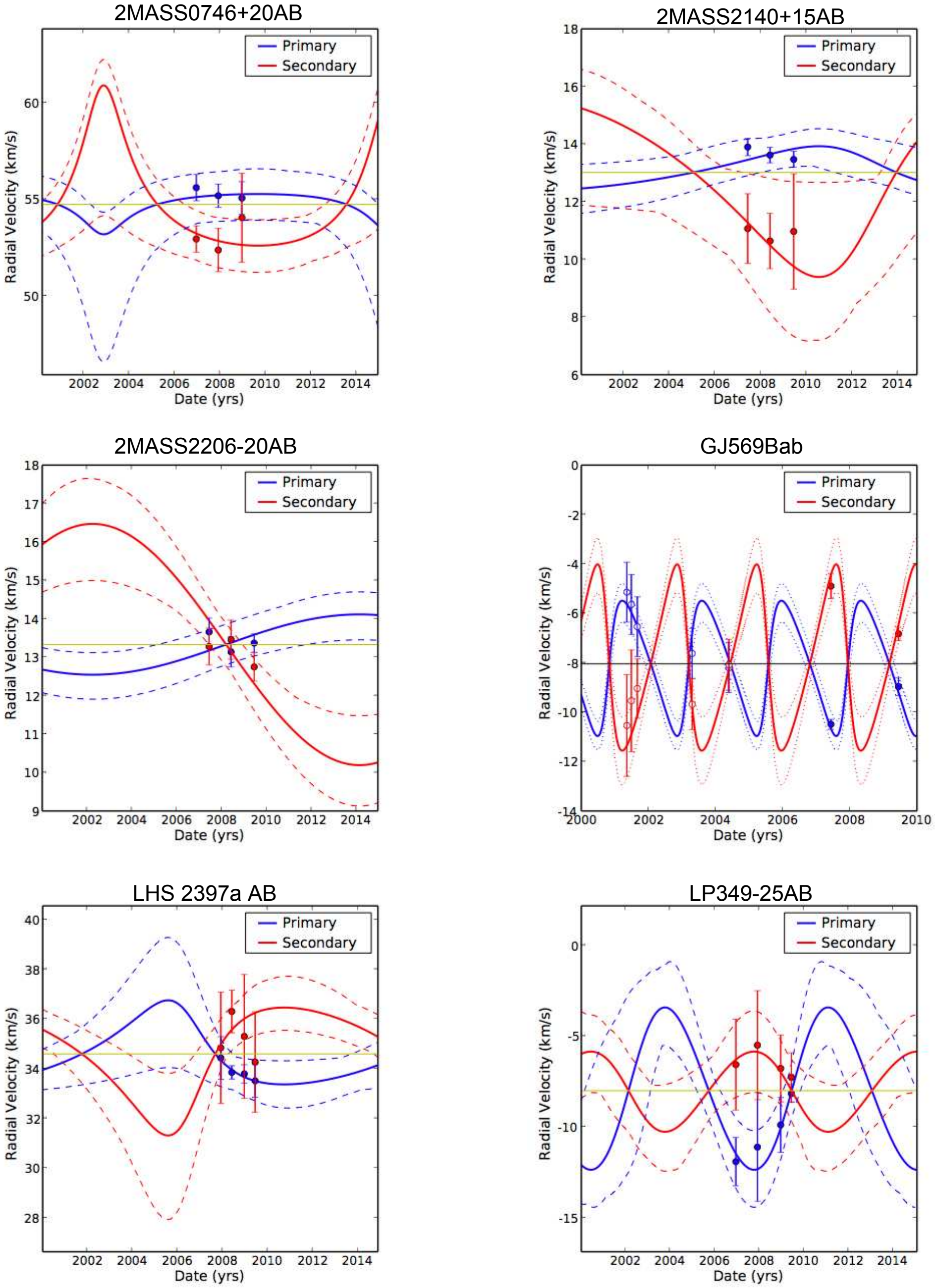

Fig. 13.— Best fit absolute orbits for 6 systems in our sample. Absolute radial velocity data points overplotted with the best fit orbits for both components. Radial velocity data from the literature for GJ 569Bab is taken from Zapatero Osorio et al. (2004) and Simon et al. (2006). The green line represents the best fit systemic velocity. The dotted lines represent the 1σ allowed ranges of radial velocity at a given time.

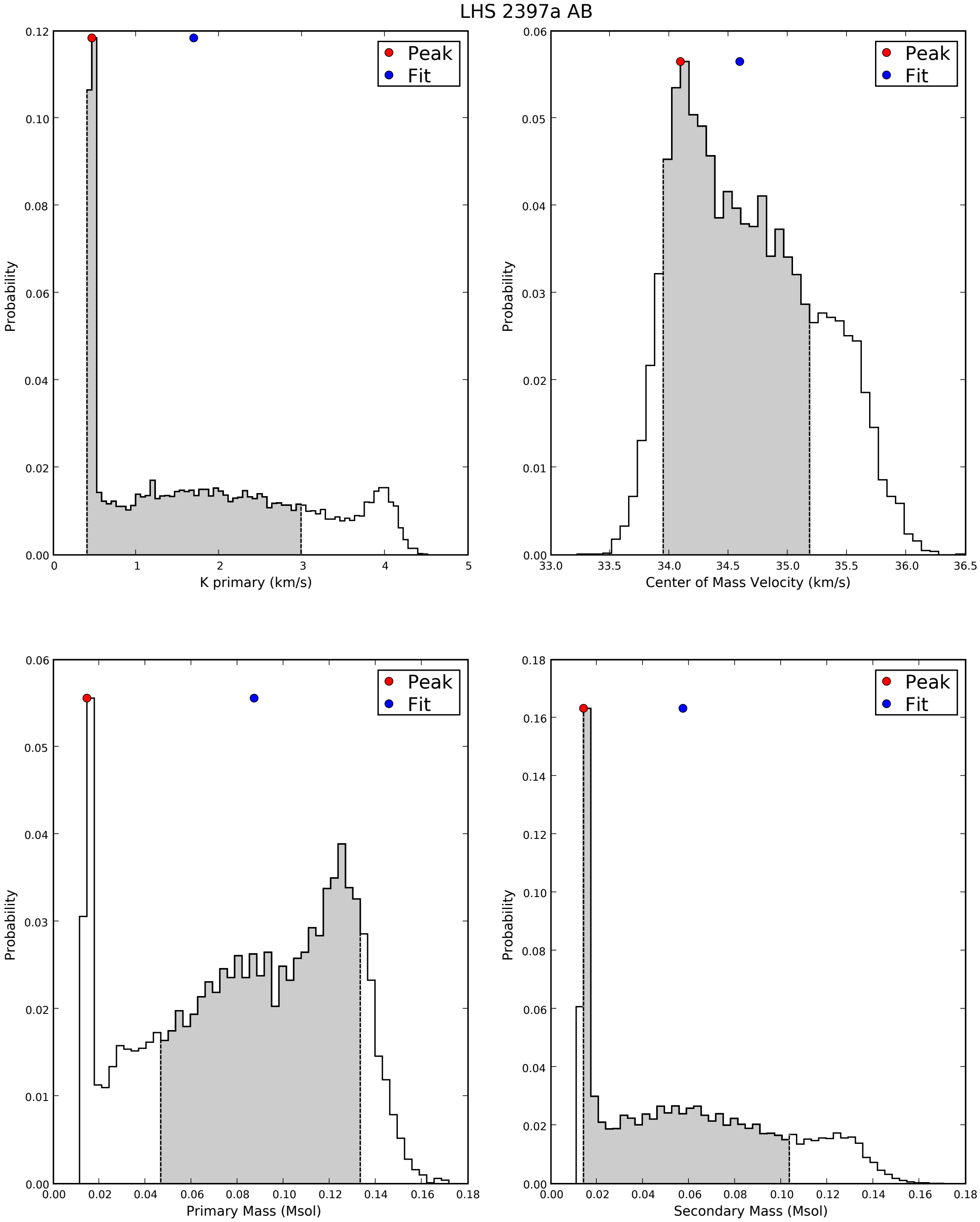

Fig. 14.— One-dimensional PDFs for the absolute orbit of LHS 2397a AB. Fit parameters are $K_{Primary}$ and γ (top panels). The distributions for parameters in common between this orbit and the relative orbit, namely P, e, T_o, and ω, are shown above in Figure **??** online. From $K_{Primary}$ and γ, $K_{Secondary}$ is calculated, giving the mass ratio, which we use in conjunction with the total system mass to derive component masses (bottom panels). PDFs for the other 5 systems with absolute orbit derivations are shown online.

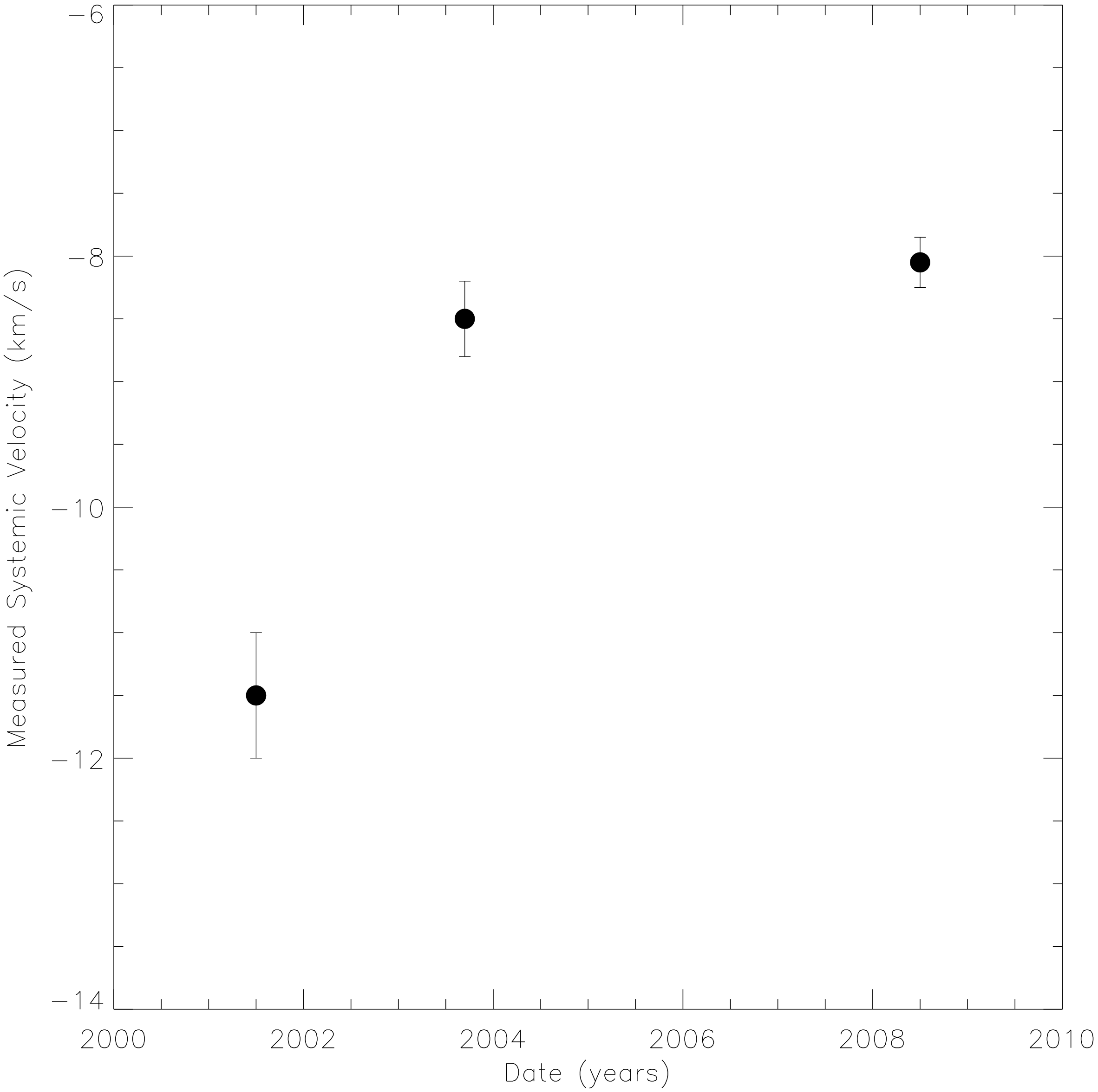

Fig. 15.— The measured systemic velocities from Zapatero-Osorio et al. (2004), Simon et al. (2006), and this study, as a function of the median time of observation. Because this source is a wide companion to GJ 569A, an M star, it is expected to undergo some change in velocity due to its orbit around GJ 569A. While the difference in our systemic velocity with respect to that of Simon et al. (2006) could be consistent with this, the Zapatero-Osorio et al. (2004) is likely too discrepant to be caused by this orbital motion.

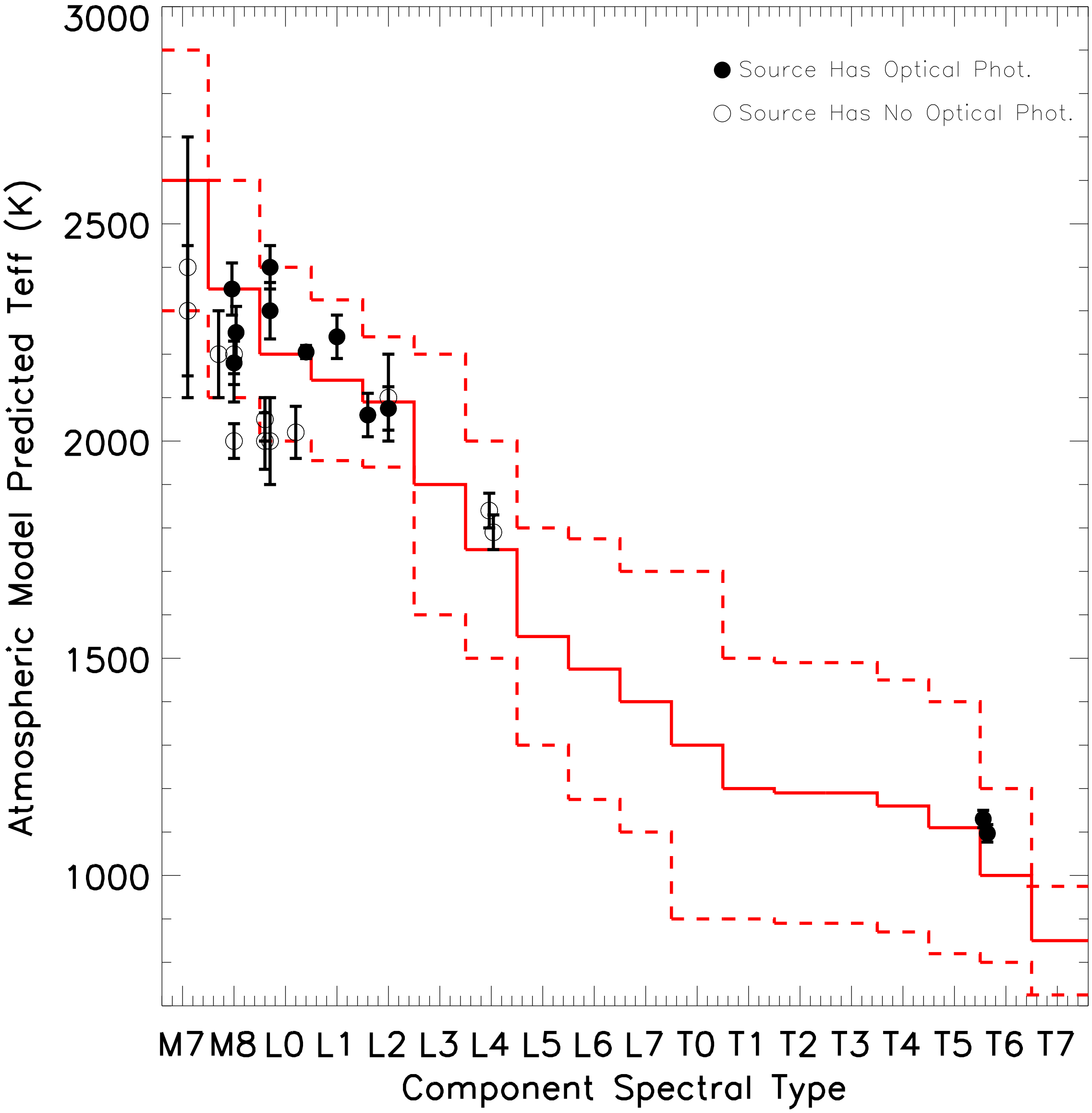

Fig. 16.— The fitted effective temperatures from the atmospheric models are plotted as a function of spectral type. The scatter in the data points further stresses the intrinsic scatter in predicted effective temperature with spectral type. Overplotted in red is an effective temperature/spectral type relationship derived from the results of Golimowski et al. (2004), Cushing et al. (2008), and Luhman et al. (2003). In most cases, the uncertainties in our derived temperatures and smaller temperature than those predicted by the temperature/spectral type relationship.

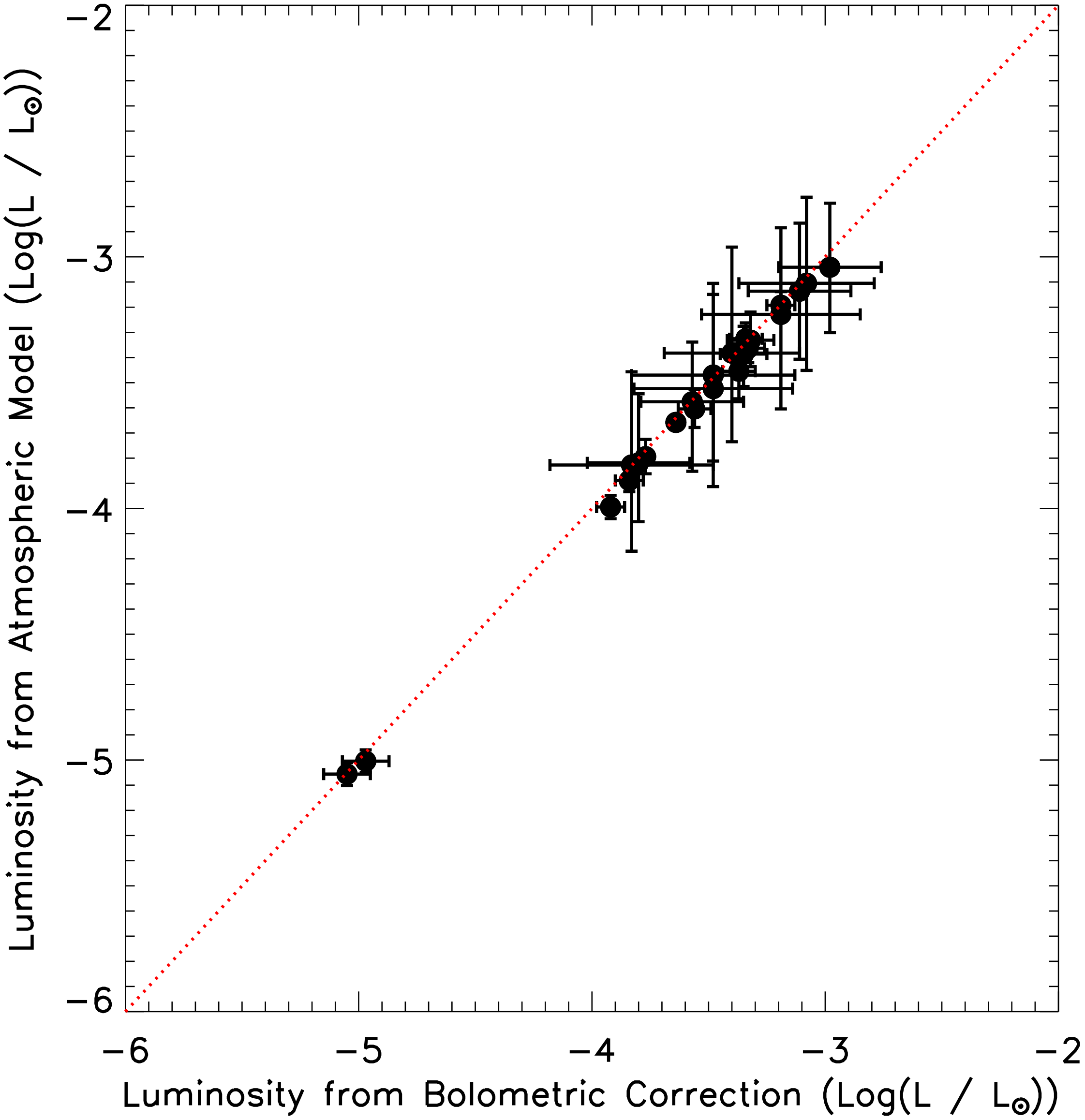

Fig. 17.— The luminosities implied from our atmospheric model fits for T_{Eff} and radius versus the luminosities derived from the bolometric corrections in Golimowski et al. (2004). The red line represents 1:1 correspondence. All values are consistent with each other. We use the luminosities from bolometric corrections for further analysis because they are completely independent of models.

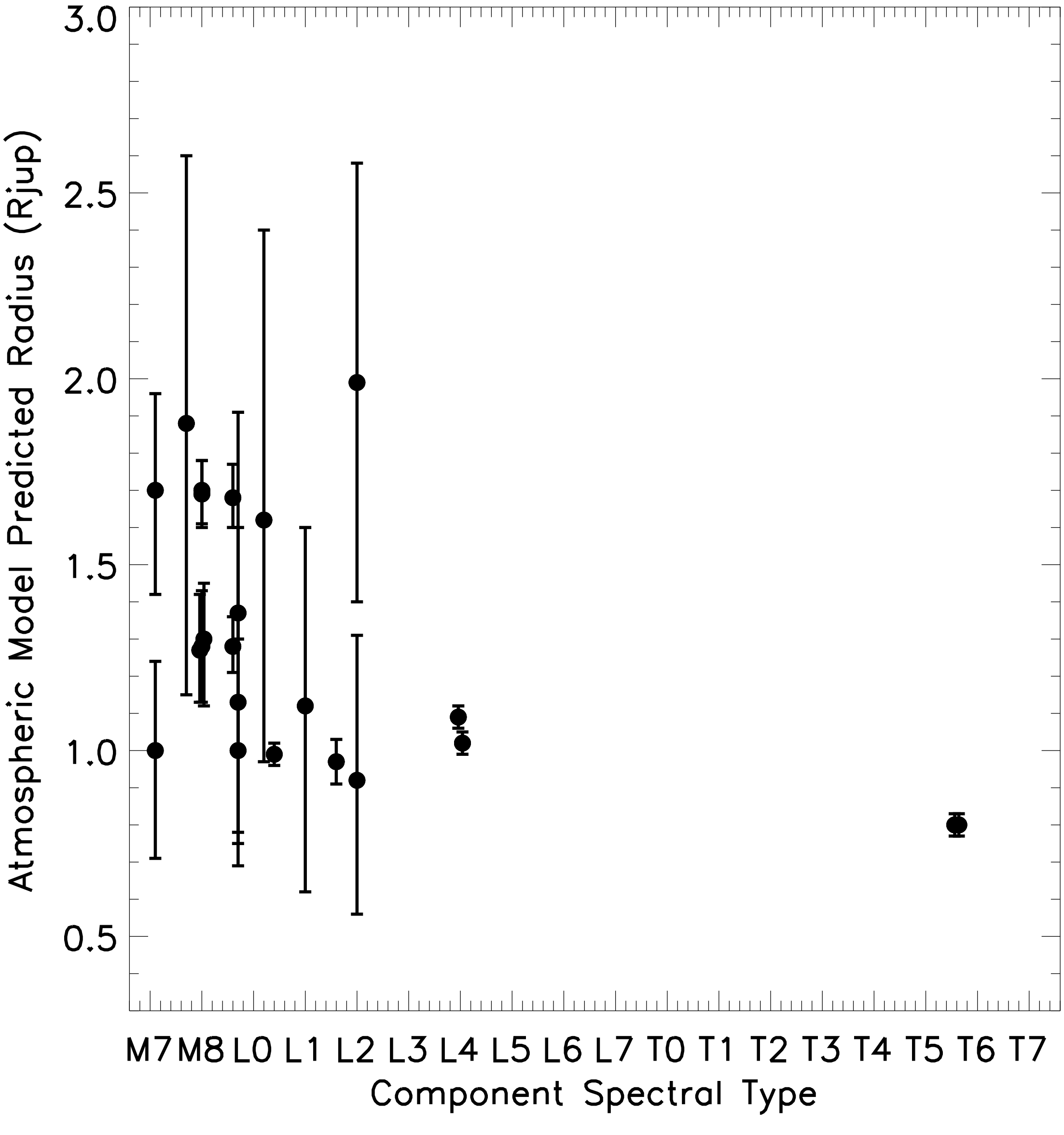

Fig. 18.— The fitted radii from the atmospheric models are plotted as a function of spectral type. A fairly large scatter in the values is seen, but this is expected given the mixed age population of our sample. The values, however, are consistently in the range expected for VLM objects of between 0.5 and 2 R_{Jup}. This result also justifies our choice of assuming a radius of 1.0 ± 0.3 R_{Jup} for the L/T transition objects that cannot be fit by the atmospheric models.

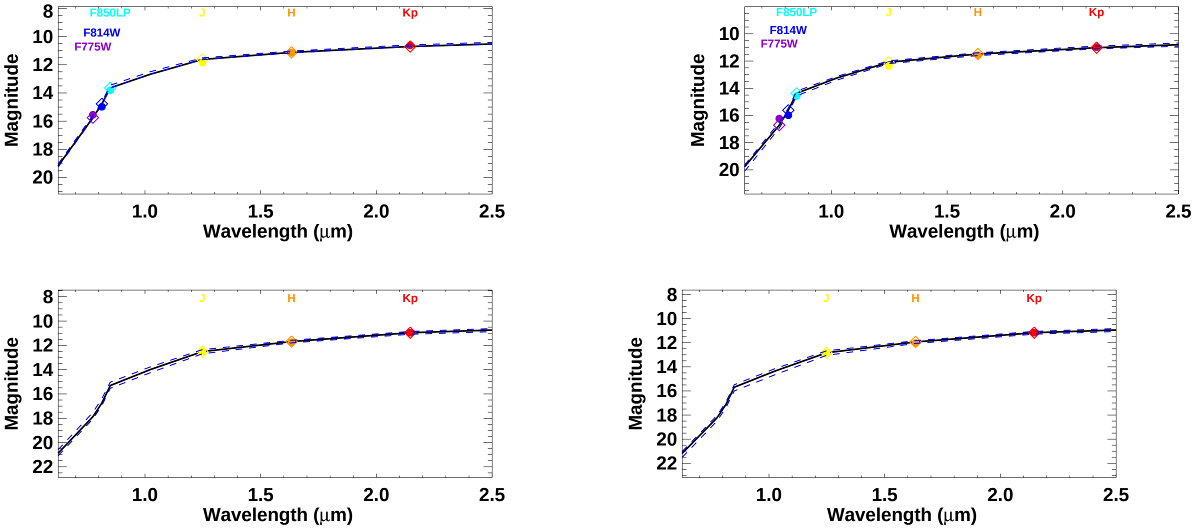

Fig. 19.— Photometry and best fit SEDs for 2MASS 0746+20A (top left, 2205 K) and 2MASS 0746+20B (top right, 2060 K). These are examples of fits in which optical data is available. Photometry and best fit SEDs are also shown for HD 130948B (bottom left, 1840 K) and HD 130948C (bottom right, 1790 K), representing fits without optical data. Photometric measurements are shown as filled circles, and best fit photometry from the DUSTY atmosphere models are show as open diamonds. The full best fit SED (generated by interpolating between the best fit photometry from the models) is overplotted in black, and the 1σ allowed ranges of magnitudes are shown as dashed blue lines. Best fit SEDs for all other sources are shown online.

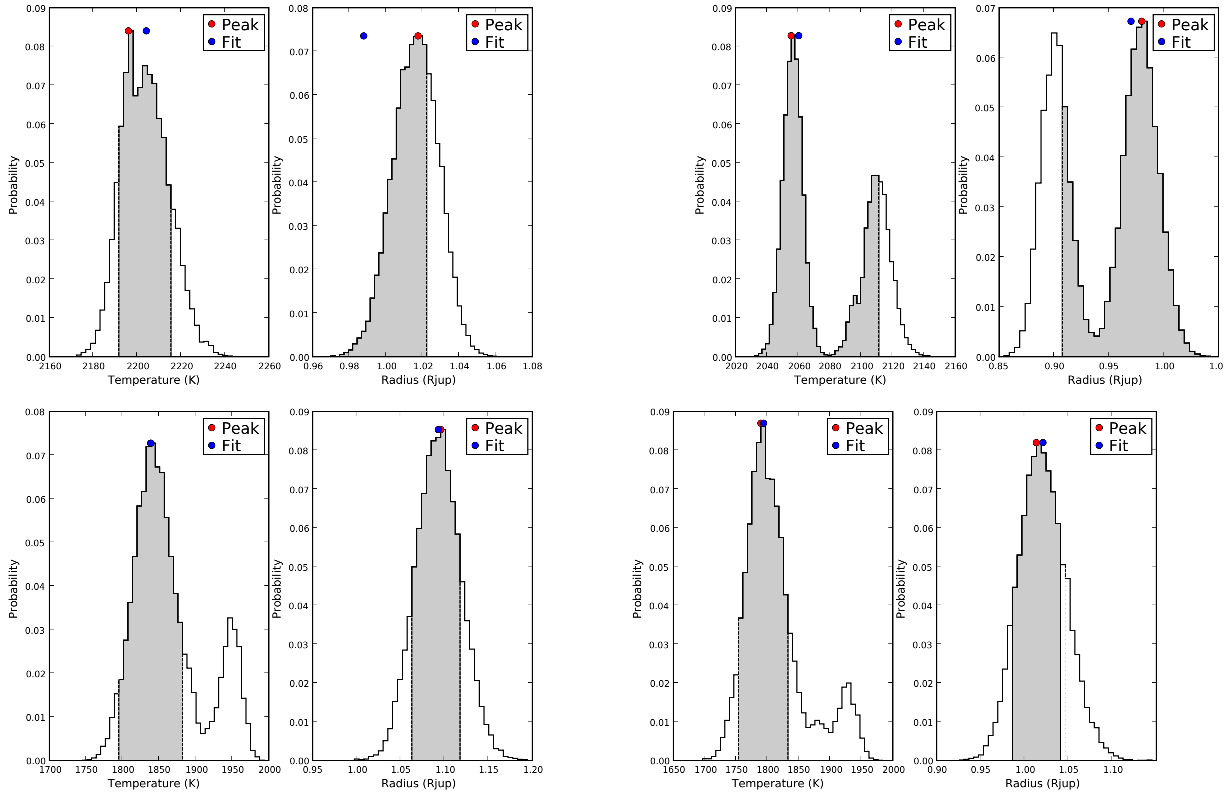

Fig. 20.— One dimensional PDFs of temperature and radius from the spectral synthesis modeling for 2MASS 0746+20A and B (top) and HD 130948B and C (bottom). PDFs for all other sources are shown online.

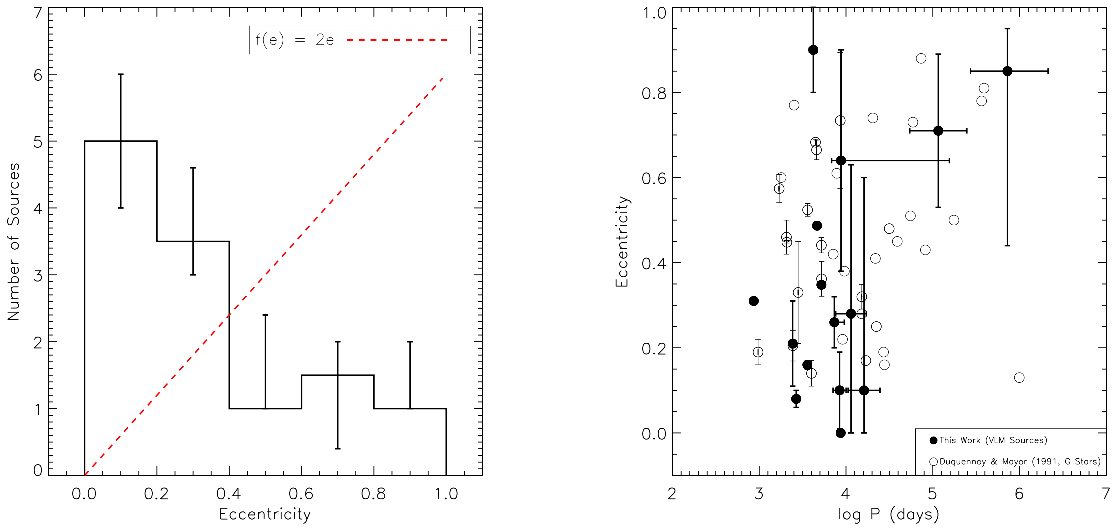

Fig. 21.— **Left:** The eccentricity distribution of our sample based on the eccentricity distributions for each source from the relative orbit Monte Carlos. Overplotted is the relation for field solar-like stars from Duquennoy & Mayor (1991), where f(e) = 2e (normalized to 15 systems). **Right:** Eccentricity as a function of period for the sources in our sample (filled circles). Overplotted are the systems from Duquennoy & Mayor (1991) with periods greater than 865 days (open circles). As in Duquennoy & Mayor (1991), eccentricity tends to increase with period.

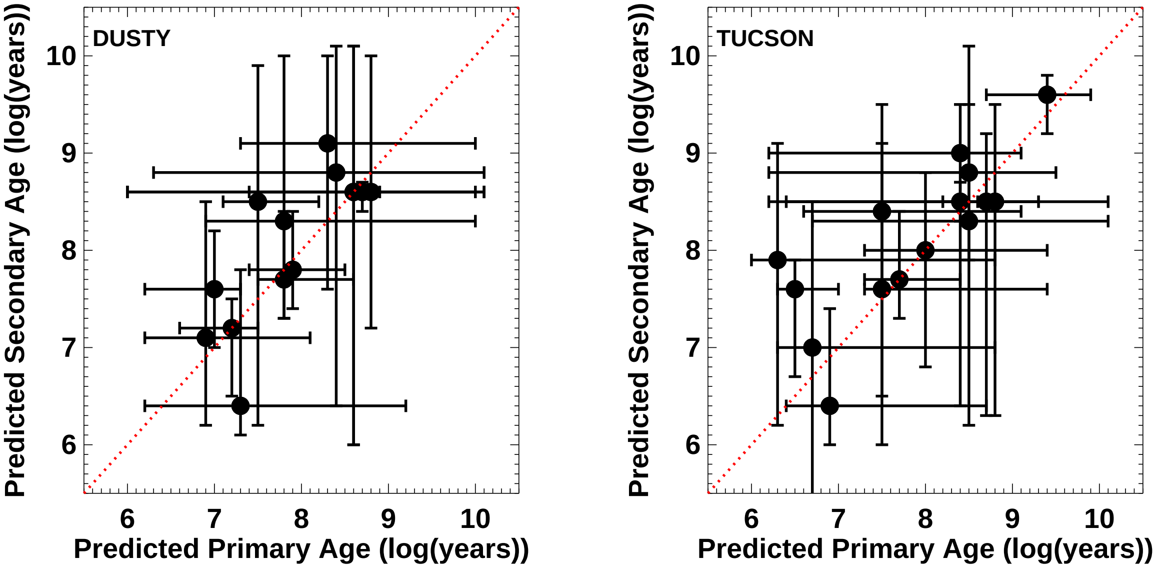

Fig. 22.— The predicted ages for secondary components versus primary components by the DUSTY (**left**) and TUCSON (**right**) models. The line of 1:1 correspondence is plotted in red. Within the uncertainties, all binary components are predicted to be coeval for all models.

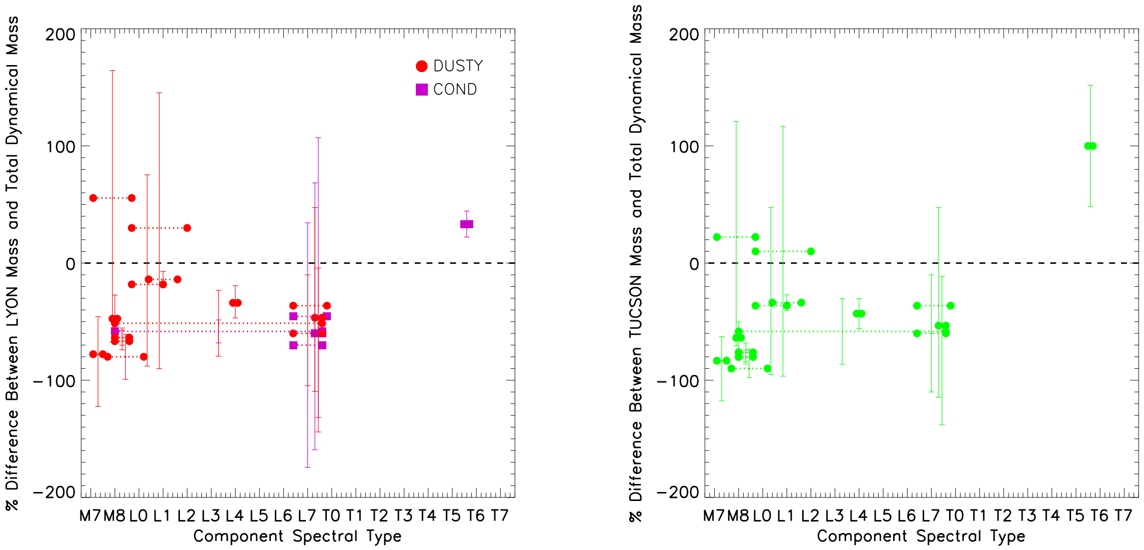

Fig. 23.— **Left:** The percent difference between the predictions of the Lyon (both DUSTY and COND, Chabrier et al. 2000) models and our total dynamical masses as a function of spectral type. Each system is denoted by the spectral type of its components, which are connected with a horizontal bar. We find that 7 of the 14 systems we have compared to the DUSTY models have their masses underpredicted by these models. These systems all have primary component spectral types earlier than L4. We find that one T dwarf system we compared to the COND models has its mass overpredicted by the models. All sources with primary component spectral types in the L/T transition region have mass predictions that are consistent with the total dynamical mass. **Right:** The percent difference between the predictions of the TUCSON (Burrows et al. 1997) models and our total dynamical masses as a function of spectral type. We caveat that while we have used different atmospheric models to derive effective temperature than is employed in the Burrows et al. (1997) models, the effect of the atmospheric model is thought to be minor. We have compared all 15 systems to these models. We find that 7 systems have their masses underpredicted by these models, all of which have primary component spectral types earlier than L4. We find that one mid-T system has its mass overpredicted by the models. All sources with primary component spectral types in the L/T transition region have mass predictions that are consistent with the total dynamical mass.

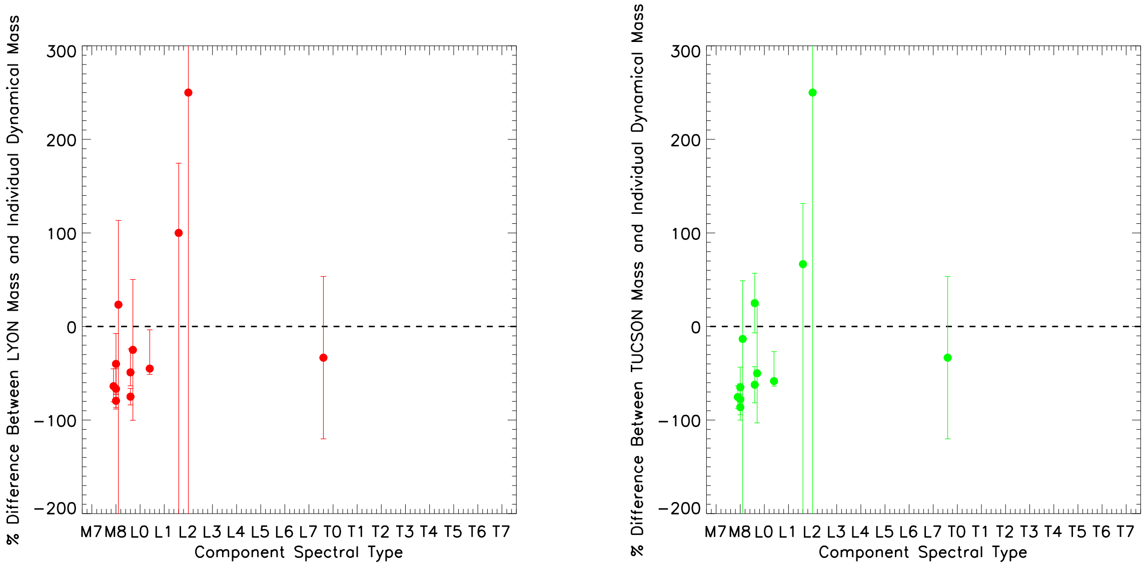

Fig. 24.— **Left:** The percent difference between the predictions of the DUSTY (Chabrier et al. 2000) models and our individual dynamical masses as a function of spectral type. We compare our 12 individual mass measurements to these models, and find that five sources have their masses underpredicted by these models. All five sources have spectral types of M8 - M9. **Right:** The percent difference between the predictions of the TUCSON (Burrows et al. 1997) models and our individual dynamical masses as a function of spectral type. We caveat that while we have used different atmospheric models to derive effective temperature than is employed in the Burrows et al. (1997) models, the effect of the atmospheric model is thought to be minor. We compare our 12 individual mass measurements to these models, and find that five sources have their masses underpredicted by these models. All five sources have spectral types of M8 - M9.

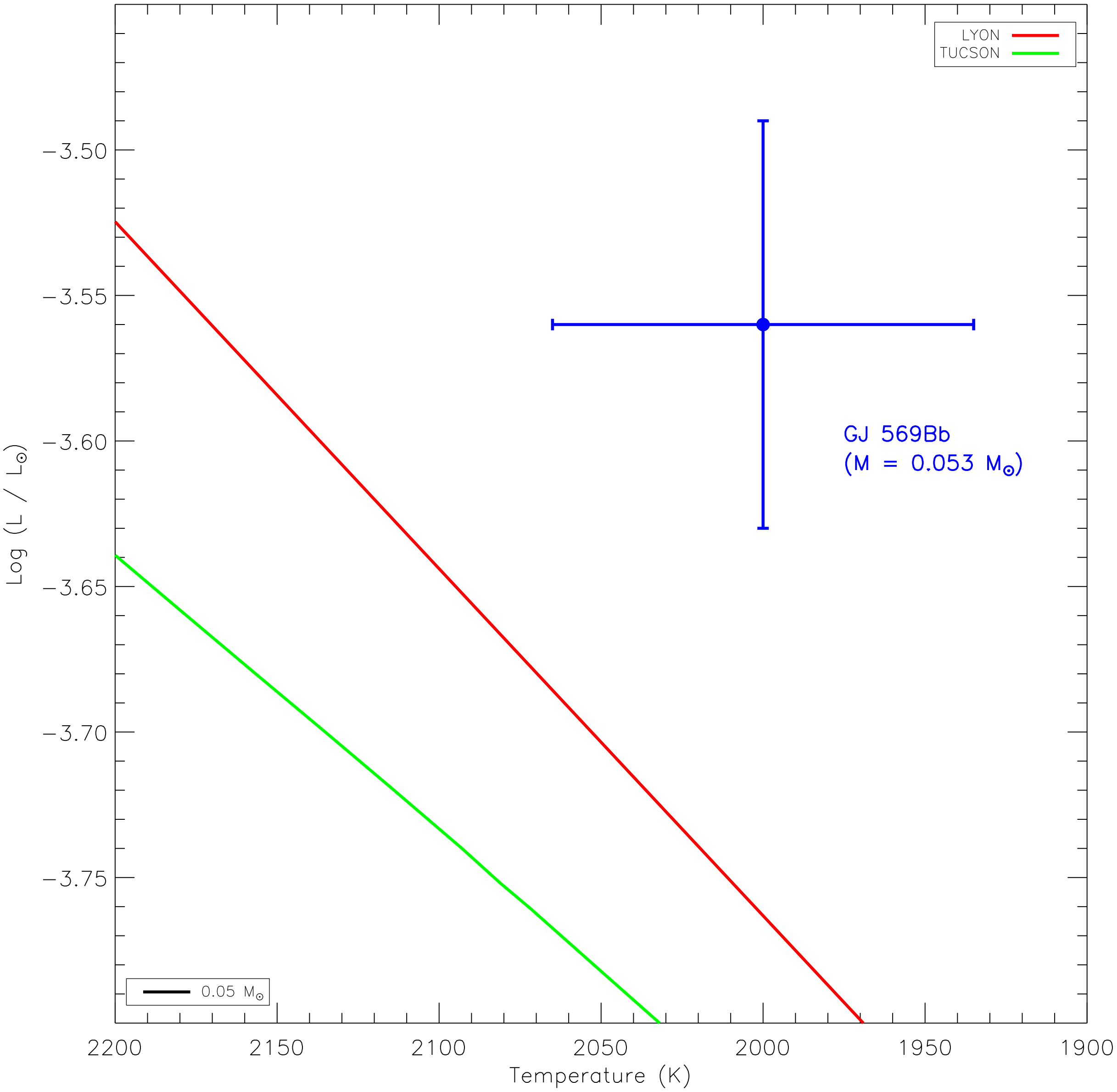

Fig. 25.— Location of GJ 569Bb on the H-R diagram given our derived temperature and luminosity. Since this system had a mass of 0.053 ± 0.006 $M_\odot$, it should lie close to the line of constant mass for a 0.05 $M_\odot$ object in the evolutionary models. The location of this line for both LYON and TUCSON are also plotted. As with all discrepant sources in our sample of spectral type M or L, the source lies above and to the right of these lines, implying either the temperature is too high in the evolutionary models, the radius is too small in the evolutionary models, or the temperature is too low in the atmosphere models for these sources.

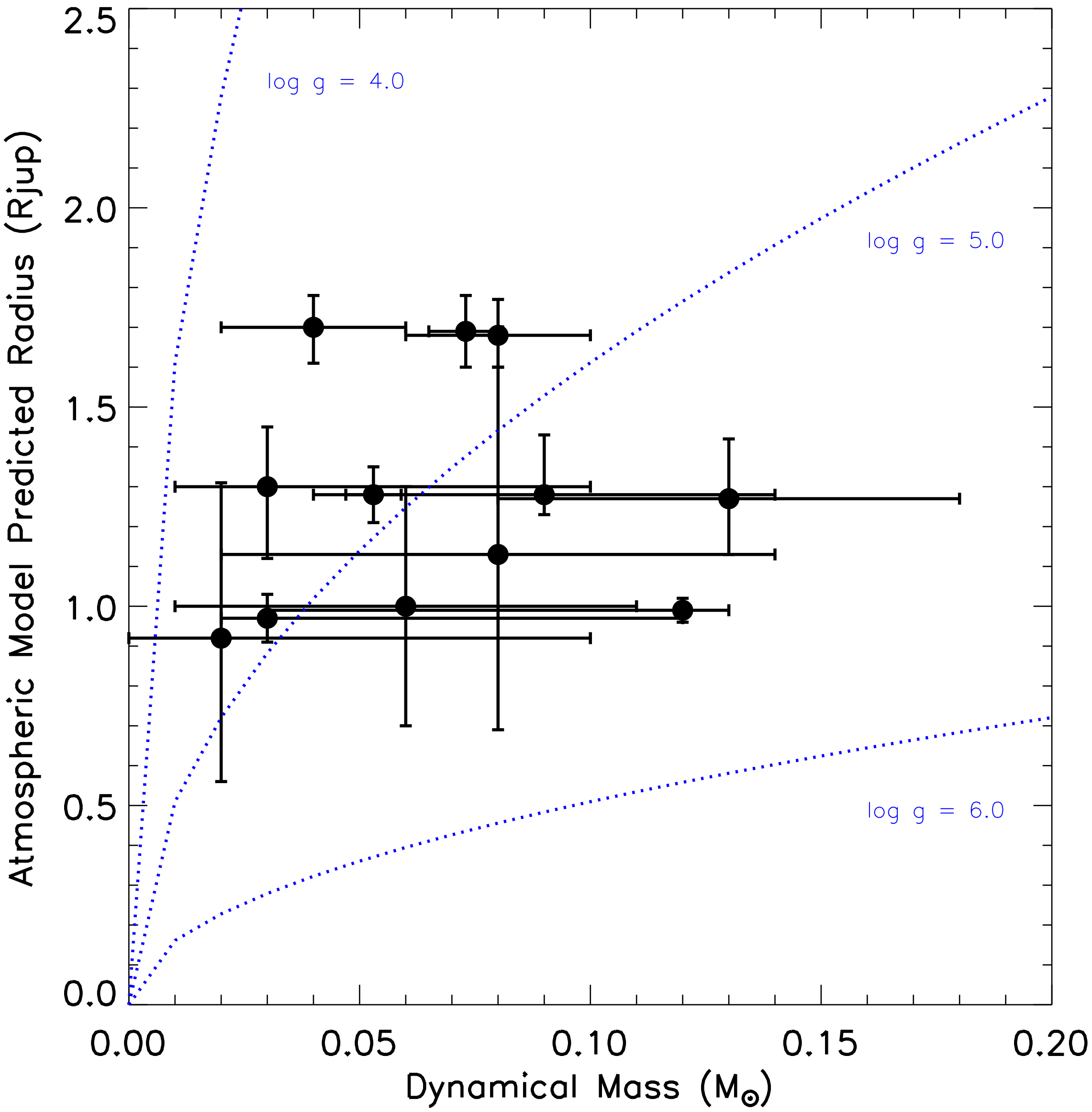

Fig. 26.— The atmospheric model-predicted radii versus the masses for sources with individual mass estimates. Overplotted are lines of constant surface gravity. With the direct measurement of surface gravity for these objects, we can find model-independent radii and reduce the scatter in this relationship.

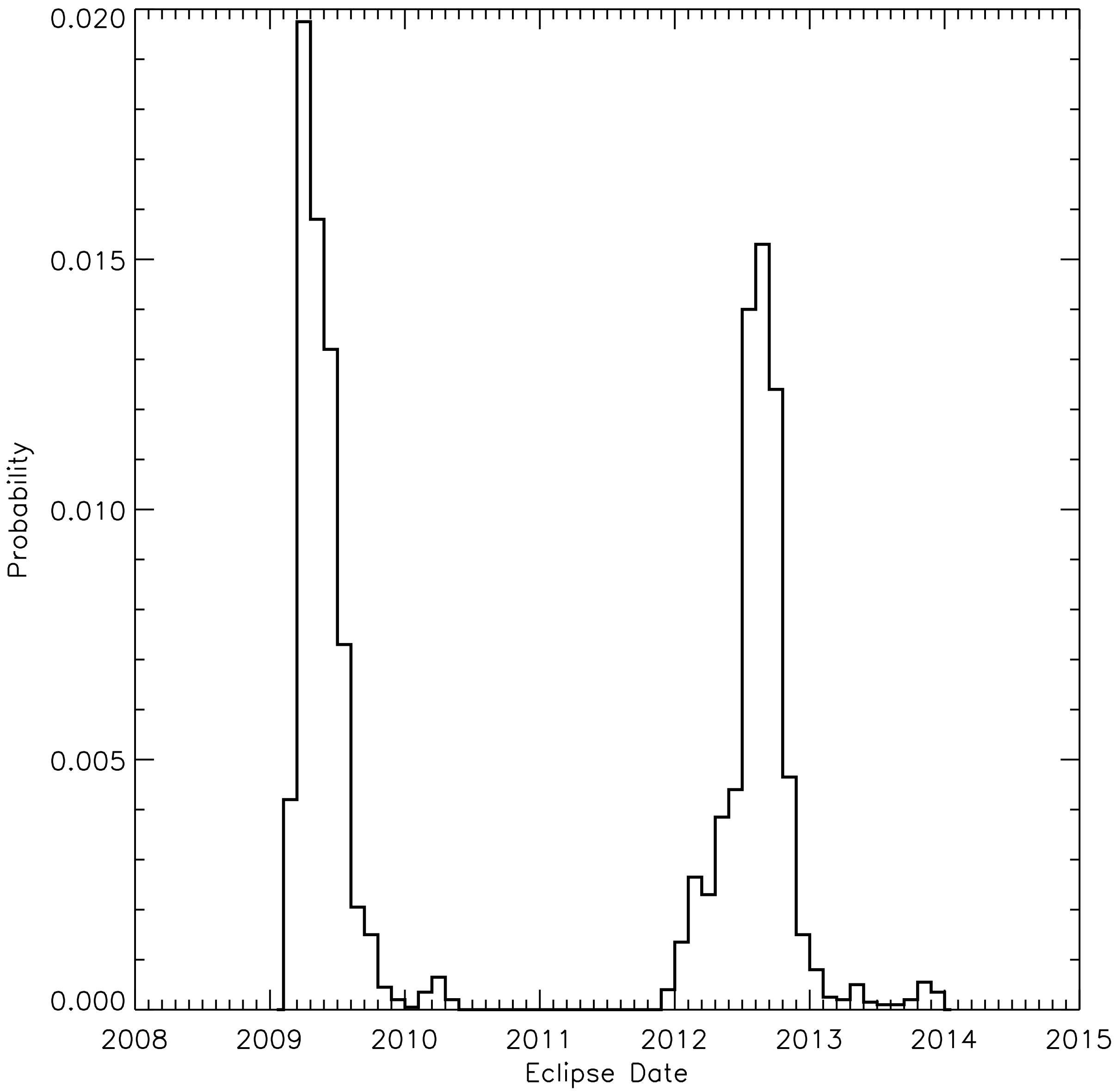

Fig. 27.— The probability of eclipse as a function of date of occurence for 2MASS 0920+35 AB. Overall, the system has a 6.8% chance of being an eclipsing system, with the most likely date of eclipse having occured in April of 2009. The next most likely date of an eclipse is in mid-2012.